PHYSIK-DEPARTMENT

Raman Spectroscopy on Single-Molecule Junctions

Doktorarbeit
von

Hai Bi

TECHNISCHE UNIVERSITÄT MÜNCHEN

TECHNISCHE UNIVERSITÄT MÜNCHEN

Physik Department E20

Molekulare Nanowissenschaften & Chemische Physik von Grenzflächen

Raman Spectroscopy on Single-Molecule Junctions

Hai Bi

Vollstädiger Abdruck der von der Fakultät für Physik der Technischen Universität München zur Erlangung des akademischen Grades eines Doktors der Naturwissenschaften (Dr. rer. nat.) genehmigten Dissertation.

Vorsitzender:	Univ.-Prof. Dr. Björn Garbrecht
Prüfer der Dissertation:	1. Univ.-Prof. Dr. Johannes Barth
	2. Univ.-Prof. Dr. Reinhard Kienberger

Die Promotion wurde am 11.09.2014 bei der Technischen Universität München eingereicht und durch die Fakultät für Physik am 07.10.2014 angenommen.

Abstract

Transport of electrons in single-molecule junctions is a fundamental process in the general field of molecular electronics. The molecule can serve as a current carrying conductor and observables such as electron transfer rates and yields can be investigated. However, in most cases, the detection is limited to the current-voltage (I-V) characteristic of the single-molecule junctions.

In this work, we present a novel method for optically studying single-molecule junctions with a home-made molecular junction spectroscopy (MJS) set-up. The near-field Raman spectrum of conducting single molecular units could be recorded with this set-up. By monitoring the Raman spectra in dependence of the applied voltages, the electron-phonon interaction in the current-driven single-molecule junction was studied with a highly conjugated organic molecule. Additionally, the switching behavior of a single-molecule junction was studied with an organic molecule with seperated $\pi-$electron systems. The applied voltage serves as the input to control the molecular conformation, and the Raman spectrum of the molecular junction serves as the corresponding output information.

Contents

Chapter 1

Introduction

Understanding transport of charge and dissipation of energy in single molecules is fundamental for the development of (macro)molecular[1, 2] and quantum molecular circuitry. In metal-molecule-metal junctions[3, 4], especially for π-conjugated molecules, control over electron-phonon coupling would make it possible to steer a wide range of dissipation effects from suppression to optimization[5, 6]. In order to gain insight into electron-phonon mediated charge transport through molecules, articulated knowledge on non-equilibrium, nonadibatic quantum molecular energy landscapes must be attained. Because of this serious theoretical challenge, extensive studies[7, 8] have been focused on giving qualitative explanations for the current-induced vibronic progressions observed upon sequential low-temperature transport experiments[9, 10] and tunneling spectroscopy at the single molecule level[11, 12]. Different methods are introduced in this field to get a better understanding at the electron transport mechanism as well as its applications. Besides electrical studies on the conductivity of molecular junctions, localized optical methods offer another promising option to study the electron transmission.

In this thesis, the electron transport process of single-molecule junctions was studied in combination with Raman spectroscopy. By monitoring the electron transport with the optical methods, it could be shown that the molecules get positively charged during transport, i.e. that charge transport is mediated by the depopulation of the highest occupied molecular orbitals. Furthermore, the electron-phonon coupling and the related parameter λ_{el-ph} was deduced from the phonon population observed in the anti-Stokes Raman spectrum of the same junction. Moreover, the switching behavior of specific single-molecule junctions was shown to be related to the charging of the molecule.

1.1 Outline of the thesis

In the first chapter the basic electron transport mechanism of nanoscale electronics (section 1.2), the two-terminal single-molecule junction (section 1.3) and Raman spectroscopy at the nanoscale (section 1.4) are introduced. In section 1.3, the properties and the vibrational effects of a single-molecule junction are discussed in detail. In section 1.4, an introduction on surface plasmon polaritons and their application at the nanoscale is given. In section 2, an insight into the properties of the tetrahedral scanning near-field microscopy tip, which is employed as a probe, is given(section 2.1). Subsequently the experimental set-up to characterize the electron transport properties of single molecules is elucidated (section 2.2). And finally, the performance of the experimental set-up was investigated (section 2.3) by measuring conductance quantization and tip-enhanced Raman spectroscopy efficiency. Chapter 3 mainly discusses the influences of the electron transport on the conjugated molecule and electron-phonon coupling. In the first part, electron-phonon coupling in of a conjugated single-molecule junctions is discussed and the electron-phonon coupling constant is deduced from the observed Raman spectrum (section 3.1). In the second part, the switching behavior of a particular single-molecule junction is discussed with the observed Raman spectra (section 3.2). Finally, we give a summary for the whole thesis (section 4).

1.2 Electron transport at the nanoscale

In the field of nanotechnology several approaches for the characterization of nano-scale devices have been developed. Also, the mechanism of electron transport through single-molecule junction has been intensely studied theoratically and experimentally[8, 13–18]. The study of transport properties shows great potential in various fields like rectifiers, switches, transistors, light emitters and organic-inorganic hybrid devices. In this section, we will briefly review the nano-scale transport mechanisms with a convenient model for electrode-bridge-electrode system[15]. Electron transport at the nano-scale cannot be simply described with the Drude model[19], but strongly depends on the properties of the electrodes and the bridge itself.

Ballistic electron transport is used to describe situations in which the mean free path of the electron is (much) longer than the dimension of the medium through which the electron travels[20, 21](section 1.2.1). Two other transport mechanisms, coherent transport[16] and sequential hopping[22], are normally used to describe the electron transport through a molecular wire. When organic molecules are involved in the electron transport process, the molecular orbitals serve as the bridge between the electrodes.

In this regard, the coupling strength of the molecular bridge to the electrode will strongly influence the transport. These two transport models can roughly be classified according to the coupling strength Γ between the molecule and the electrode. The electron transport is often coherent if Γ is strong and if Γ is weak it can often be described as sequential hopping. This difference will be discussed in more detail in section 1.2.2 and 1.2.3. At the same time, there is no dichotomy between the coherent tunneling and the sequential hopping mechanism of electron migration in the molecular wire. Depending on the properties of the molecule or the environment, these two transport mechanisms can play different roles, or even show their signature within the same molecular junction at the same time.

1.2.1 Ballistic electron transport

Ballistic transport is observed when the length of the transport channel is much smaller than the mean free path of the electron. The transport is restricted to 1D along the transport channel[20, 21, 23]. For the studies of a metal wire suspended in vacuum, the single atom or several atoms are regarded as the transport channel for the electrons. A schematic view of ballistic conductance situation is shown in figure 1.1. The conductance reaches a limiting value G, when the length of the conductor (L) is smaller than the mean free path of the electron[4, 24, 25].
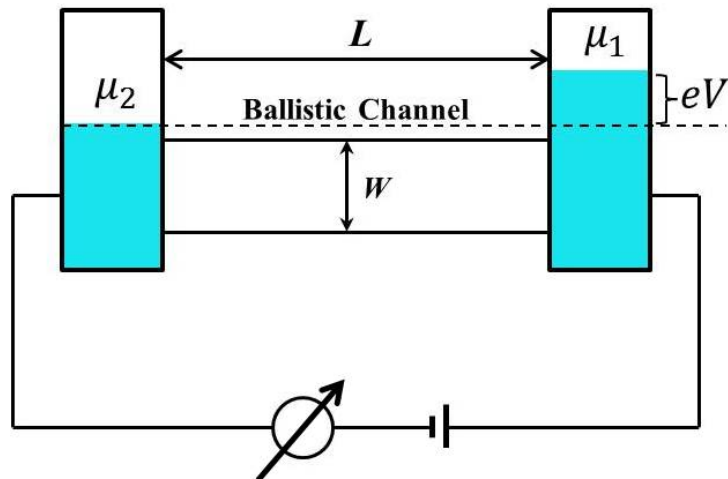

FIGURE 1.1: A ballistic conductor connected to two electrodes. A voltage is applied which forms a chemical potential difference of $\mu_1 - \mu_2$ between the electrodes. L is the length of the conducting channel.
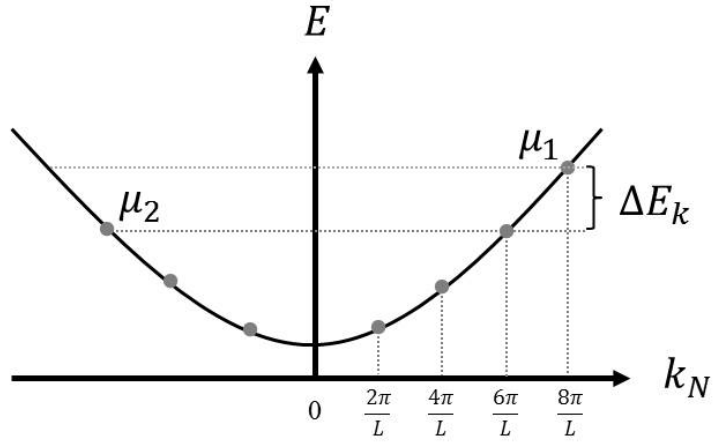
FIGURE 1.2: The schematic of a single eigenchannel model. The channel is described by discrete k-states at corresponding energies.

Figure 1.2 shows a single eigenchannel model, where $k_N = \dfrac{2\pi}{L}N$. The current carried by this bridge can be expressed as:

$$I = \frac{e}{L} \sum_k v(f_1(\varepsilon_k) - f_2(\varepsilon_k)) \tag{1.1}$$

where $\dfrac{e}{L}$ is the electron density, v the velocity of the conducting electrons, and $f(\varepsilon_k)$ the Fermi distribution. For a one-dimensional conductor, considering the electron spin and converting the sum over k into an integral, it turns into

$$I = \frac{2e}{h} \int_{\mu_2}^{\mu_1} (f_1(\varepsilon_k) - f_2(\varepsilon_k))d\varepsilon = \frac{2e}{h}(\mu_1 - \mu_2) \tag{1.2}$$

As shown in Figure 1.1, the electrochemical potential difference can be written as $\mu_1 - \mu_2 = eV$, thus

$$I = \frac{2e^2}{h}V. \tag{1.3}$$

This leads to an expression, where the conductance is not depending on the length of the conductor and is given by:

$$G = \frac{2e^2}{h} \approx \frac{1}{12.9}\frac{1}{k\Omega} \tag{1.4}$$

More generalized one has to sum up all contributing conductance channels,

$$G = \frac{2e^2}{h} \sum T_n \tag{1.5}$$

where T is the transmission possibility[26].

According to the Laudauer formula, the resistance R of the bridge between the electrodes can be further described by.

$$R = \frac{h}{2e^2}\frac{1}{T} = \frac{h}{2e^2}\left(1 + \frac{1-T}{T}\right) = \frac{h}{2e^2} + \frac{h}{2e^2}\frac{R'}{T} \qquad (1.6)$$

For a nanobridge in between the electrodes, the resistance can be devided into two parts. The first part $\frac{h}{2e^2}$ represents the quantized resistance. The second part represents scattering from the barriers. If R' is 0, the conductor is a perfect conductor, where quantized conductance is observed (that is, the conductance exhibited steps near 4, 3, 2 and 1 quantum units)[25, 27, 28]. If a molecular wire is is decoupled from the leads, R' will govern the transport mechanism, which will be discussed below.
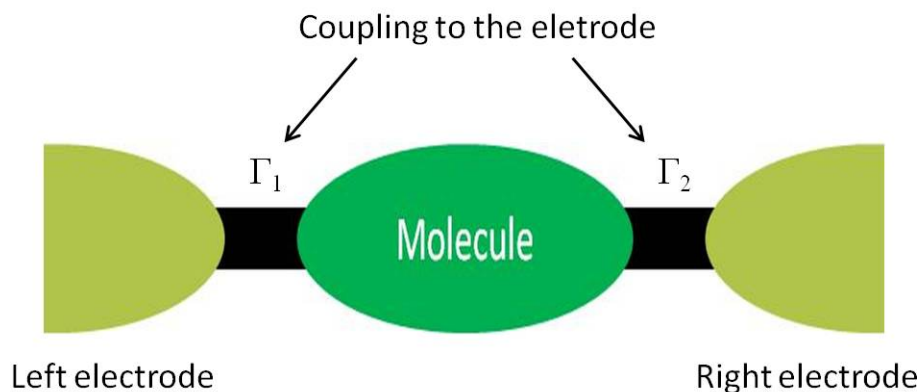
1.2.2 Coherent transport

FIGURE 1.3: Sketch of metal-molecule-metal-junction to model the transport. The molecule couples to the electrodes with the coupling strength Γ_1 and Γ_2.

Coherent tunneling is one of the mechanisms that describes electron transport through a single-molecule junction. In this process, the phase information of the wavefunction of the electron is preserved and the inelastic interactions take only place well inside the electrodes[1, 29, 30]. Coherent transport is not sensitive to the temperature of the environment. Theoretically, coherent transport is mainly influenced by the coupling strength Γ between the molecular wire and the lead (figure. 1.3). A strong coupling will change the electron transport into a scattering problem.

For coherent transport, the molecular orbitals play the role of the conduction channel and will influence the transport process. Interactions can be among all molecular levels, and they can couple to the electrode with a coupling strength Γ(figure 1.3). Due to the interaction between the molecule and the metal electrodes, some charge rearrangements and geometric reorganization will occur. After this process, the simplest model for the
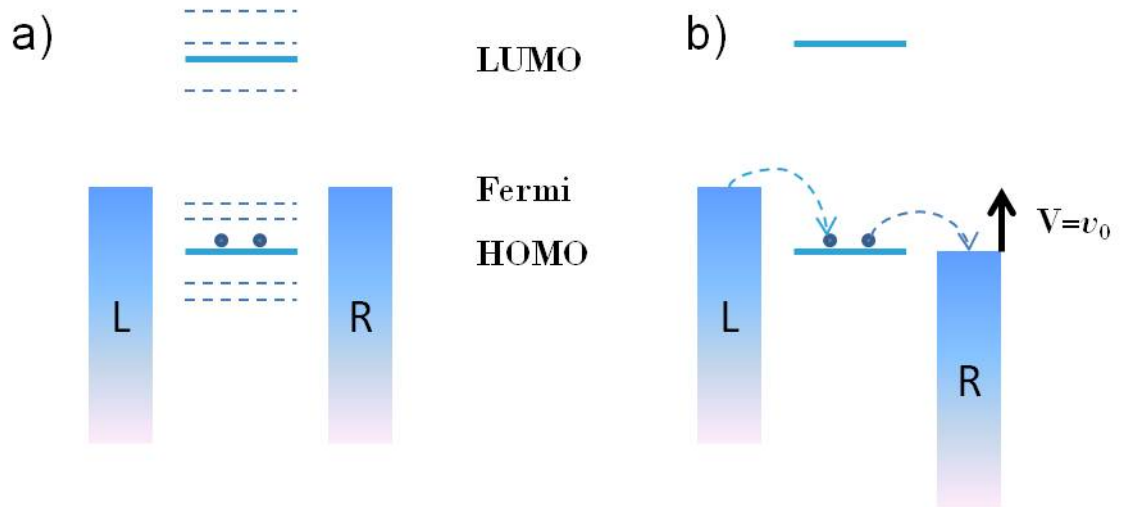
FIGURE 1.4: (a)Simplified molecular model of molecular orbitals between the electrode at zero bias region. The molecule has a series of sharp resonances corresponding to the different molecular orbitals, whereas the metal has a continuum of states that is filled up to the Fermi energy. (b) Molecular junction with a certain applied voltage v_0 where the HOMO is aligned with the chemical potential of one of the electrodes[16].

coherent transport is described by the level scheme in figure 1.4 a. The Fermi level of the leads lies in between the highest occupied molecular orbital (HOMO) and lowest unoccupied molecular orbital (LUMO) of the bridge molecule[16, 29, 31]. Moreover, the Fermi level is not necessarily halfway in the HOMO-LUMO gap but could lie anywhere in between. This picture is oversimplified, assuming that mixing between a molecule and an electrode is relatively weak compared with the inter-atomic interactions that develop the molecular electronic structure.

In principle, different molecular orbitals can participate in the electron transport simultaneously. However, in most cases, one specific level (HOMO or LUMO) lies closest to the Fermi level of the metal and therefor dominates the transport in a certain voltage range. With such a single-level tunneling model, we can explain the shape of the I-V curves of coherent transport. In our discussion, the HOMO is assumed to be the specific level that dominates the electron tranport.

Figure 1.4 b) shows the electron transport of the molecular junction at a certain voltage. For coherent transport, the current is symmetric with respect to votage inversion and it has a characteristic shape where one can distinguish three different regions. For the first stage at low bias, the current is quite low and independent of the voltage. For a certain voltage (v_0) where the HOMO level is aligned with the chemical potential of one of the electrodes, the current is greatly enhanced and shows a steplike feature(figure 1.5)) in the observed I-V curves. The corresponding differential conductance, $G = dI/dV$, exhibits peaks at the resonant conditions. If the applied voltage exceeds v_0, the current
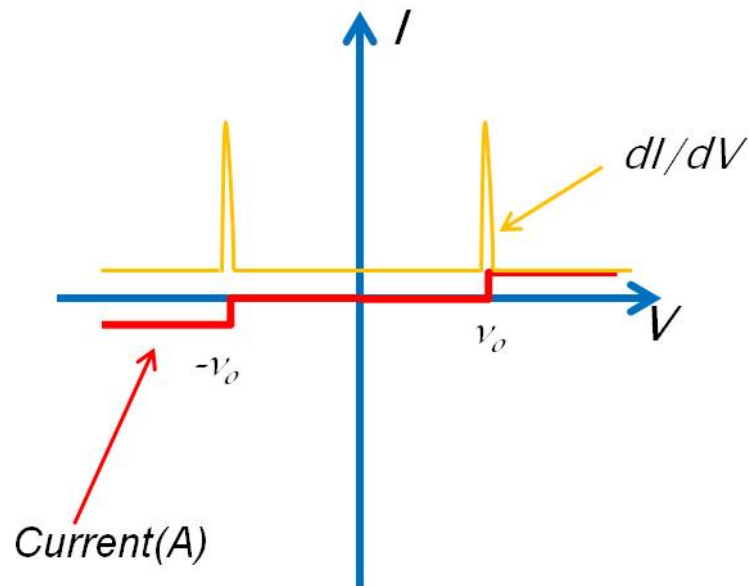
FIGURE 1.5: Current vs. bias voltage in the resonant tunneling model(red curve). The corresponding differential conductance $G = dI/dV$ (yellow curve).

stays constant until the next molecular orbital gets in resonance with one of the chemical potentials of the electrodes.

1.2.3 Sequential hopping

Besides the coherent transport mechanism, sequential hopping describes the electron transport through a nano-bridge with a scattering character when the coupling strength Γ is rather weak. Figure 1.6 shows the transport processes governing the electron behavior in the regime of sequential hopping. Here, the molecular bridge has N sites (or states) and the incoherent tunneling between them is described by the transfer rates $k_{i,j}$ (from state j to state i).

During the hopping transport, the electrons occupy each site and an energy barrier has to be overcome during this process. In this case, the sequential hopping regime is normally characterized by the following two main signatures[32–36]: Firstly, the conductance depends on the number of sites and therefor on the length of the molecular wire. Secondly, the conductance can depend exponentially on the temperature which is called thermally assisted sequential tunneling. These two features are totally different from the coherent tunneling mechanism[22, 37]. The transport in non-conjugated molecular wires, e.g: mainly consisting of C-C bonds, is well described by sequential hopping, as well as through the DNA-based molecular junctions[37].
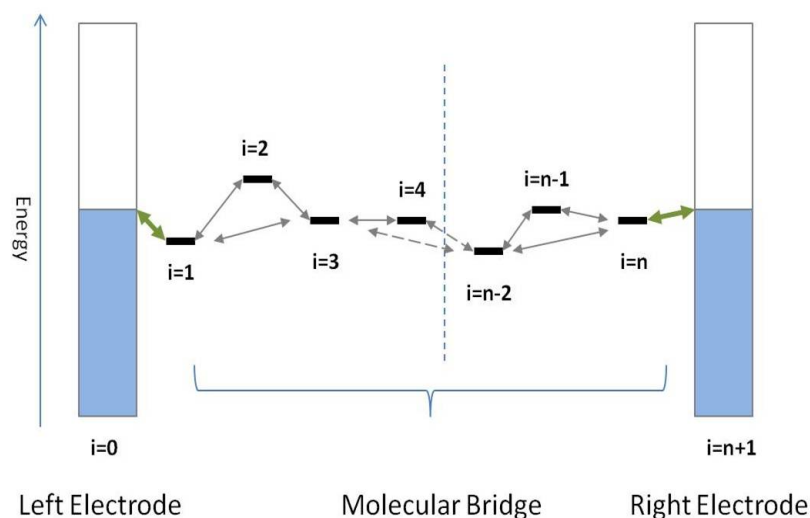
FIGURE 1.6: The sketch shows a modeled long-wired molecular conductor with N bridge sites embedded between metallic leads. Only next-neighbor tunneling is considered[22].

1.3 Single-molecule junctions

The ability to measure and control the current through a molecule is one of the central parts to build electronic devices, using individual organic molecules. This also offers us a unique opportunity to understand charge transport behavior in nanoscale devices, which is important as well for organic displaying techniques, organic solar cells or computational units.

In recent years, a variety of techniques have been developed to realize single-molecule devices[2, 38–40]. Lots of experiments and theoretical discussions have been published to characterize the behavior of single molecules in a conductive junction. We will mainly focus on the fabrication methods (section 1.3.1), the unique properties of conjugated single-molecule junctions (see section 1.3.2) and finally vibrational effects of single-molecule junctions (section 1.3.3).

1.3.1 Techniques to characterize single-molecule junction

A number of techniques to study the electron transport through organic molecules and monolayers of those have been developed within the last decades[17, 18, 30, 41]. Here, a brief overview on the most common techniques is given.

Scanning-tunneling-microscope break junction

The scanning-tunneling-microscope (STM) break junction experiment is one of the most popular methods for single-molecule junctions[42–44], which uses the metallic tip as one
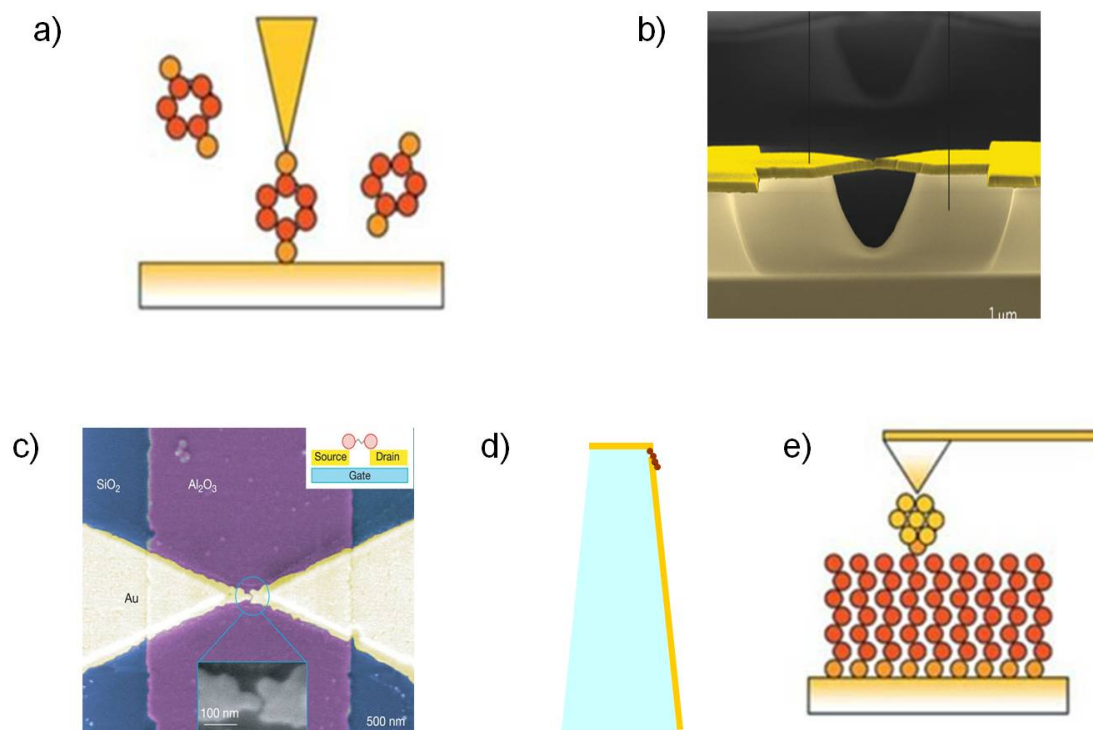
FIGURE 1.7: Techniques to form single-molecule junctions. (a) Scanning tunneling microscope break junction. (b) Mechanically controlled break junction. (c) Electromigrated gaps. (d) Tip-end junction. (e) Nanoparticle-molecule metal junction. Adopted from[30].

electrode and metal substrate as the other electrode. Normally, self-assembled monolayers (SAM) grown on the substrate serve as the molecular bridge. The tip is moved towards the SAM. By carefully controlling the tip position, one can build the molecule junction in between the tip and the substrate, as shown in figure 1.7 a). This method offers the possibility to repeatedly build the molecular junction[42] to collect statistical data. The main drawback of this method is the insufficient stability of the set-up to keep covalently linked molecules for a sufficiently long wire between the electrodes. Furthermore, this method gives the possibility to vary the materials of the tip and the sample.

Mechanically controlled break junction

Mechanically controlled break junction is supposed to be the most reliable method to build a single-molecule junction. Lots of set-ups and experiments rely on this method[29, 45]. The unique properties of the single-molecule junction have been discussed in detail[16, 29, 40, 45]. The working principle of the mechanically controlled break junction (MCBJ) is shown in figure 1.7 b). The pre-structured suspended metal bridge is mechanically broken by bending the substrate. Hence, the molecular bridge can be formed between the electrodes. There are two methods to deposit the organic molecules. One is placing a drop of solution[29, 40]. The other method is exposing the fractured electrode

pair to a gas that bonds on the metal[45]. The contact is established between the electrodes by mechanically controling the gap distance. Similar to the STM method, MCBJ also enables the studies of the electromechanical properties of single molecules[46]. A recent modification includes a variable electric-field gate that allows correlations between the structure of the junction and its energy level positions[47]. With the merit of the mechanical stability of MCBJ, reliable low-temperature measurements (4.2 K) could also be achieved[40].

Further methods for single-molecule junctions

Except for the most popular methods of STM break junctions and MCBJ, some other methods are also used to study single-molecule junctions.

The first one is to form small gaps by means of electromigration. An e-beam-patterned metal structure (figure 1.7 c)) is formed either on an oxide-covered Si surface or on an Al strip covered with a condensed-oxide layer. Both of the substrates serve as back gates to the junction[48–51]. The substrate is immersed in solution or exposed to vapor of the desired molecules to achieve the molecules adsorption in the region where the gap will be created. Afterwards, the treated substrate is transferred into vacuum or sometimes cooled to cryogenic temperatures. When a high current is passing through the constriction, electromigration induces an opening of a junction. As a consequence, molecules will bridge the occurring gap eventually. The process is usually stopped when the resistance of the junction rises to > 100 KΩ, indicating that a tunneling gap has formed. This method is useful to offer a on-chip single-molecule device which can be used for repeated measurements. However, the width of the gap is not very reproducible.

As shown in Figure 1.7 d), the tip-end junction is also a method that has been used for the fabrication single-molecule junctions. This method[39] combines advantages of both tunable and fixed contacts. It is based on the fabrication of metal single electron transistors on scanning tips and is highly dependent on the second gold evaporation process. A metal electrode (Au) is deposited on the top face of a cubic shaped quartz tip. Then, the apex of the tip is dipped in the solution with molecules. Afterwards, a sublayer of a molecular film will grow at the apex of the tip. By controlling the evaporation angle, the other electrode is evaporated on top of the tip. And the conductance of the forming junction is monitored to achieve a singl-molecule junction. For this method, the evaporation angle should be well controlled and the molecular junction is easy to be influenced by the evaporated gold atoms.

Besides the methods described above, there was also lots of effort devoted to modifying the tip or the substrate. As shown in figure 1.7 e), gold coated conducting atomic force microscope probe is used to locate and contact individual gold particals bonded to the

monolayer. The measured I-V curve depends directly on the number of the molecules contacted or bridged in the junction[25].

1.3.2 Conjugated molecular junctions

For the studies of single-molecule junctions, the wire shaped molecule plays the role of the conduction channel. Despite biological systems, the molecular wires can loosely be divided into two categories, saturated and conjugated chains[52]. Non-conjugated molecular wires mainly consisting of C-C bonds are well studied[25, 42, 53–55]. The large bandgap (HOMO-LUMO) of these molecules has limited the further use of this kind of molecular wires. However, they serve as a model to study the transport mechanism. They exhibit sequential hopping transport, where the conductance decreases exponentially with molecular length (L)[25, 36, 56]. Due to the rapid decrease of the tunneling rate with the molecular length, experiments with saturated chain molecules are limited to molecular lengths of $2 - 3$ nm.

By contrast to the saturated molecule junctions, conjugated chains play the major role for the investigation of electron transport and potential appliction in the future.

Influence of side groups on the conjugated molecular wire

For conjugated molecules, the delocalized π electrons facilitate the electron transport through the molecular junction. Experiments have demonstrated that charge transport could occur over a better conjugation molecular junction (figure 1.8)[37, 57].
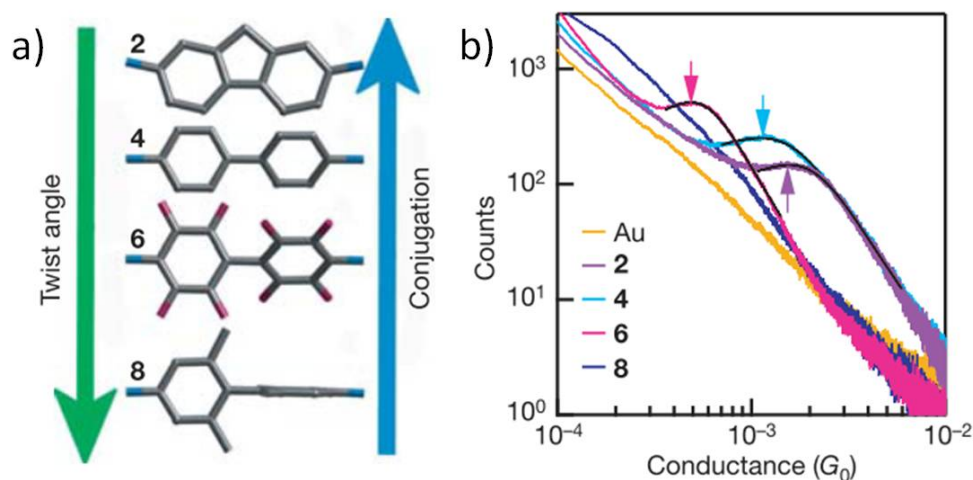

FIGURE 1.8: a)Structure of a subset of the biphenyl series studied, shown in order of increasing twist angle or decreasing conjugation. b) Conductance histograms of the different molecules obtained with a STM at a bias voltage of 25 mV. [58]

For certain conjugated molecular junctions, the electrical conduction highly depends on the degree of the delocalization of the molecular obital. In other words, the introduction of the side group can influence the conduction of the molecular wire by interrupting the whole $\pi-$conjugation of the system (figure 1.8). Venkataraman and coworkers have presented a set of experiments in which the properties of electron transport through different biphenyl molecules have been studied[58, 59]. They found that the conductance decreases with increasing twist angle between the phenyl rings, consistent with a cosine-squared dependence, which is expected in transport through $\pi-$conjugated biphenyl systems. The transport through a molecular junction depends crucially on the position of the relevant orbitals in the molecule with respect to the Fermi energy of the electrodes and also on their degree of delocalization. Thus, the internal electronic structure of a molecule plays a fundamental role and it can be chemically tuned to a certain extend with the inclusion of appropriate side-groups or substituents. In principle, side-groups can cause two main effects: (1) They can control the structure of a molecule which in turn determines the degree of conjugation (delocalization of the molecular orbitals) and (2) they can tune the position of the frontier orbitals. Both effects have an impact on the conductance of a junction. These effects are well known in the field of electron transfer, but so far they have been difficult to test systematically in molecular junctions.

Switching behavior in conjugated molecular junctions

The controlled switching of single-molecule junctions could be considered to have great potential in the field of computational applications. In recent years, these properties have been intensely discussed experimentally and theoretically[60–65].

For instance, the molecular wire, bipyridyl-dinitro oligophenylene-ethynylene dithiol (BPDN-DT)(figure 1.9 b)), was reported to have the potential to show switching behavior in several studies[60–62]. By applying a voltage pulse to the molecular junction, the observed I-V curves suggest the existence of a switching behavior. This process could be realized by repeating the procedure with inverted bias. The molecule gets stuck in a (meta)stable state which has a characteristic I-V curve. The physical origin of the switching behavior of the molecular junction is still being discussed. He *et al.* attributes it to a change in the oxidation state of the molecule in their experiment[64]. At the same time, Galperin *et al.* proposed the assumption that a polaron-caused bistability is a possible explanation[65]. On the other hand, Keane *et al.* announce that a bias-driven modification of the contacts may be responsible[61, 62]. Velimir Meded *et al.* give a more detailed discussion about the physical origin of the switching behavior[63]. Both, possibility of charging and conformational changes are discussed. In summary, the switching behavior of the single-molecule junction is intensely discussed and the related
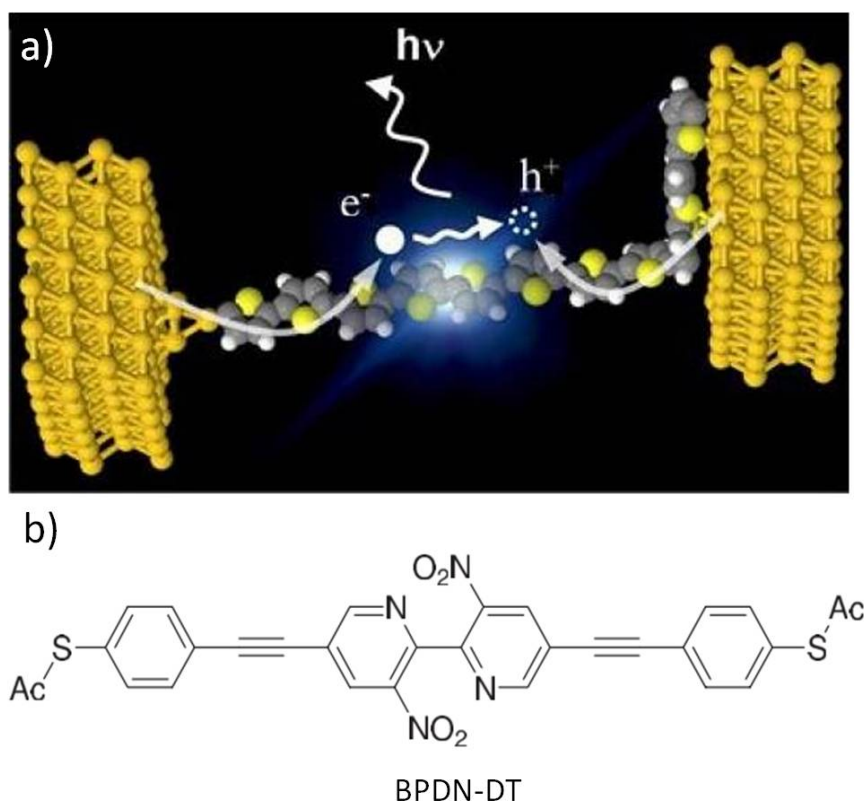
FIGURE 1.9: a) Conjugated molecule as a computational unit. b) Molecule BPDN-DT shows the switching behavior in several studies. Adopted from [66].

theoretical models have been proposed. However, no direct evidence has been shown for the explanation of the switching behavior.

1.3.3 Vibrational effects in single-molecule junctions

By contrast to inorganic quantum dots, organic molecules have certain degrees of flexibility, and can, for instance, undergo a series of internal changes that can strongly affect transport behavior[8, 12, 67–72]. These experimental observations have motivated theoretical work[8, 11, 69, 73], and the theoretical considerations predict that current transport through single-molecule junctions depends strongly on parameters such as the strength of the electron-phonon coupling and the vibrational relaxation rates[73–77]. Molecules can be characterized by a discrete spectrum of vibrational modes.

When an electron is hopping to or from the molecular orbital, it can trigger a molecular vibration. The probability for this to happen is described by the electron-phonon constant λ. The Franck-Condon principle plays an important role for describing a molecular vibration during transport (figure 1.10). For a charged molecule, the final vibrational state of the excited molecule highly depends on the square of the overlap integral between the vibrational wave functions of the initial, Ψ_i, and the final state, Ψ_f[78]. The

Fanck-Condon constant, describes this degree of overlap. The coupled system of electrons and vibrations in a molecular contact can be generally modeled by the following Hamiltonians:

$$H = H_e + H_{vib} + H_{e-vib} \tag{1.7}$$

$$H_e = \sum_{ij} d_i^\dagger H_{ij} d_j \tag{1.8}$$

$$H_{vib} = \sum_\alpha \hbar\omega_\alpha (b_\alpha^\dagger b_\alpha + 1/2) \tag{1.9}$$

$$H_{e-vib} = \sum_{ij} \sum_\alpha d_i^\dagger \lambda_{ij}^\alpha d_j (b_\alpha^\dagger + b_\alpha) \tag{1.10}$$

Here ω_α are the vibrational frequencies, $H_{ij} = \langle i|H|j \rangle$ are the matrix elements of the single particle electronic Hamiltonian H in the atomic orbitalbasis $\{|i\rangle\}$. Furthermore λ_{ij}^α are the electron-vibration coupling constants.
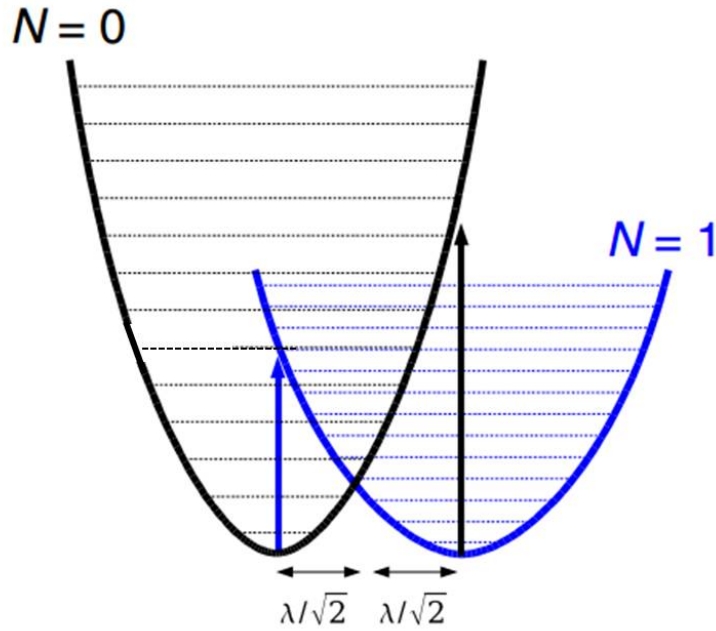

FIGURE 1.10: Schematic representation of Frank-condon effect principle. for the neutral ($N = 0$, black) and charged ($N = 1$, blue) electronic state of the molecule. The large charging energy has been subtracted since near the charge degeneracy point only changes in the vibrational energy are of importance for the differential conductance. Adopted from [76]

$$\lambda_{ij}^{\alpha} = \left(\frac{\hbar}{2\omega_{\alpha}}\right)^{\frac{1}{2}} \sum_{k\mu} M_{ij}^{k\mu} A_{k\mu,\alpha} \qquad (1.11)$$

where the ionic masses are described by $M_{ij}^{k\mu} = \left\langle i|\nabla_{k\mu}H|_{\vec{Q}=0}|j\right\rangle$, and A represents the transition matrix.

The current suppression originates from the behavior of the Frank-Condon matrix elements. This will determine the rates of the phononic transitions. Depending on the electron-vibration coupling constants λ_{ij}^{α}, the coupling could be classified into weak coupling, where $\lambda_{ij}^{\alpha} \ll \sqrt{\triangle E^2 + \Gamma^2}$, and strong coupling, where $\lambda_{ij}^{\alpha} \gg \sqrt{\triangle E^2 + \Gamma^2}$[37, 79–81]. In the limit of weak electron-phonon coupling, the vibrational modes give rise to a small inelastic current that is superimposed in a background caused by the elastic contribution.

For the case of strong coupling, vibronic effects can dominate the transport characteristic of a molecular junction. In some works, the Frank-Condon blockade was discussed during the strong coupling situation[79]. The observation of the Frank-Condon blockade has recently been reported for the suspended carbon nanotube quantum dots[69]. In practice, the calculation of the vibrational modes is restricted to a central region that includes the molecule and a small portion of the electrodes. In principle, one should also describe how these central vibrations are coupled to the phonons of the electrodes.

1.4 Raman spectroscopy at the nanoscale

Raman spectroscopy is one of the most efficient methods to study the vibrations in molecular systems. Various chemical informations related to the molecular system is supposed to be observed from the Raman spectrum[82]. C. V. Raman and K. S. Krishnan reported the phenomenon of Raman scattering for the first time in 1928[83]. After that, enormous progresses regarding Raman spectroscopy as well as in understanding plasmonics have been achieved.

When illuminating the matter(organic or inorganic), light can interact with it in different ways: being scattered elastically, being absorbed or it can inelastically interact with several excitations of the material. Inelastic, nonresonant interactions with vibrational modes of the material are called Raman scattering. In this process, an electron in one of the molecular obitals is excited by an incoming photon into a virtual state, which is energitically located in between the HOMO and the LUMO level of the molecule. From this short-lived virtual state, the electron can radiatively decay back into a vibrationally

excited state. In this process, a vibration is created on the molecule. The energy of the photon depends on the energetic difference of the initial and final state of the electron. As illustrated in figure 1.11, the incident light, with an excitation energy of $\triangle E$, will be absorbed and emitted as Rayleigh scattered light, with a same energy $\triangle E$. A small ratio of the incident light will be scattered to a lower or higher energy, termed as stokes Raman scattering and anti-Stokes Raman scattering. If the final state of the molecule has a higher energy than the initial state, the frequency of emitted light is red shifted. This red shift in the frequency is called Stokes shift. At the same time, the vibrational modes of a molecular system might be already strongly occupied. Electrons with an energies higher than the ground state can be excited and the generated photon could absorb the energy of the vibration. The resulting blue-shift is called anti-Stokes shift. Because the different vibrational modes have discrete energies and represent a clear fingerprint of the chemical structure and conformation of the material, the Stokes and anti-Stokes Raman spectra show the same red and blue shifted energies with respect to incoming laser light.

By analyzing the Raman shifted light one can measure the photon spectrum of the scattering object. In general, Raman shifts are expressed in terms of wavenumbers, whose unit is the inverse wavelength (normally cm^{-1}):

$$\Delta\omega = (\frac{1}{\lambda_0} - \frac{1}{\lambda}), \tag{1.12}$$

where $\Delta\omega$ is the Raman shift, λ_0 the wavelength of the incident light and λ the wavelength of the Raman spectrum.

Raman scattering cross sections are extremely weak, which challenges the detection of the Raman signal. We will briefly review the surface plasmon polaritons (section 1.4.1), the development of scanning near-field microscopy (section 1.4.2), tip-enhanced Raman spectroscopy (section 1.4.3) and finally the Raman spectrum of individal molecule (section 1.4.4). Near-field enhancement mechanisms offer signal enhancements of several orders of magnitude in respect to conventional Raman scattering. Furthermore, surface enhanced Raman spectroscopy (SERS) has facilitated the detection of the Raman spectra on rough metal surfaces. Another technique employs enhanced Raman scattering in the proximity of an atomically sharp tip, which displays a single hot spot and enables the detection of enhanced Raman spectra even on the single molecular level. This approach is called tip-enhanced Raman spectroscopy (TERS). It gives the possibility to perform spectroscopic imaging with sub-diffraction spatial resolution ($<$20 nm) by scanning the local *hot spot* at the end of the tip across the sample surface.
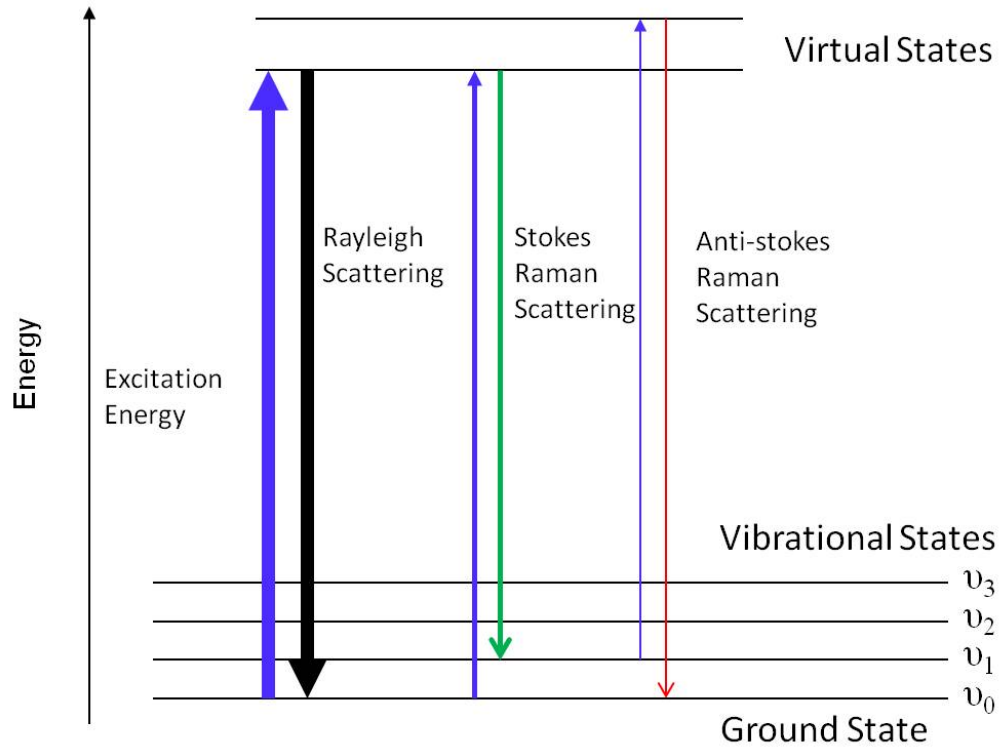
FIGURE 1.11: Energy level diagram of Stokes and anti-Stokes Raman scattering.

1.4.1 Surface plasmon polaritons

Surface plasmon polaritons (SPPs) are collective electromagnetic excitations propagating along the interface between a dielectric/vacuum and a metal (figure 1.12 a)). SPPs involves charge motion in the metal and an electromagnetic wave propagating along the interface with an exponential decay perpendicular to the interface(figure 1.12 b)). Wood *et al.* observed such a phenomenon for the first time in 1902[84]. Many years later, Cunningham and co-workers introduced the term of surface plasmon polariton[85]. From then on, the research kept developing by different groups in this field[86–98].

Normally, the excitation of SPPs is discussed at a single interface between the metal and the dielectric. For a thick layer of metal on a dielectric layer, the excitation should generate two independent SPPs waves on both interfaces of the metal. In this case, the evanescent field of the two uncoupled SPP waves cannot overlap in the metal. When the metal film is thin enough, the evanescent field in the metal starts to overlap, and coupling of the two SPP waves occurs at the interface. As a result, the SPP waves split into two coupled modes, symmetric and asymmetric ones. For the symmetric SPP mode, the loss of the electric fields is very small and its propagation length is very long. This mode is termed as long-range SPP. In contrast, the asymmetric mode shows a decaying electric field. Consquently, the propagation length is much shorter due to the large ohmic losses in the metal. The asymmetric mode is termed as short-range SPP.

Figure 1.13 visualizes the dispersion curve of SPPs in metal, the linear behavior of light with $k = \varepsilon/c$ in vacuum, and the linear behavior of light in dielectric. k_x is the wave-vector parallel to the surface. c is the velocity of light, ε_d and ε_m are the frequency dependent complex dielectric functions of the dielectric and the metal, respectively. ω_P, ω_{SP} and ω_{SPP} represent the volume plasmon, surface plasmon and surface plasmon polariton frequencies.

$$\omega_{SP} = \omega_P \sqrt{\frac{1}{1 + \varepsilon_d}} \tag{1.13}$$

The expression of the wavenumber k_x for the propagation of SPPs along the x-axis as a function of the frequency ω_{SPP}, can be derived by solving *Maxwell's equations* in both media taking into account the boundary conditions at the interface.

$$\omega_{SPP} = \sqrt{\frac{\varepsilon_m + \varepsilon_d}{\varepsilon_m \varepsilon_d}} c k_x \tag{1.14}$$

According to the SPP dispersion relation (equation 1.14), the interaction between the electromagnetic wave and surface charges will cause an increase in the SPP momentum, but at the same time, increase the momentum mismatch between the light and SPP. In order to efficiently excite surface plasmon polaritons, different configurations have been proposed[90, 91, 102, 103].

Figure 1.14 shows different SPP excitation configurations. In the Kretschmann configuration, shown in figure 1.14 a), a thin film is illuminated from within the dielectric in total
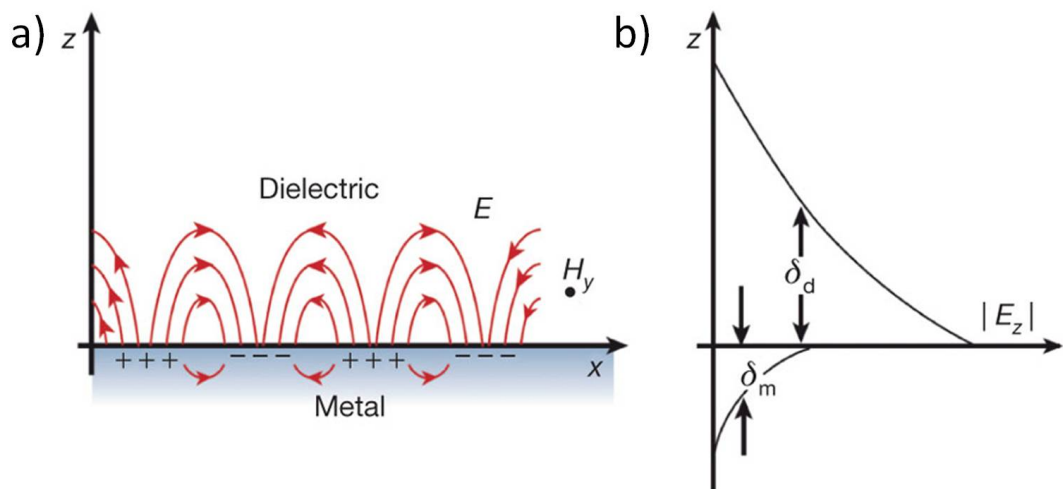

FIGURE 1.12: (a) Schematic illustration of electromagnetic waves and surface charges at the interface between the metal and the dielectric material, (b) the local electric field component near the surface. It decays exponentially with distance in the direction normal to the interface. Adopted from [99].
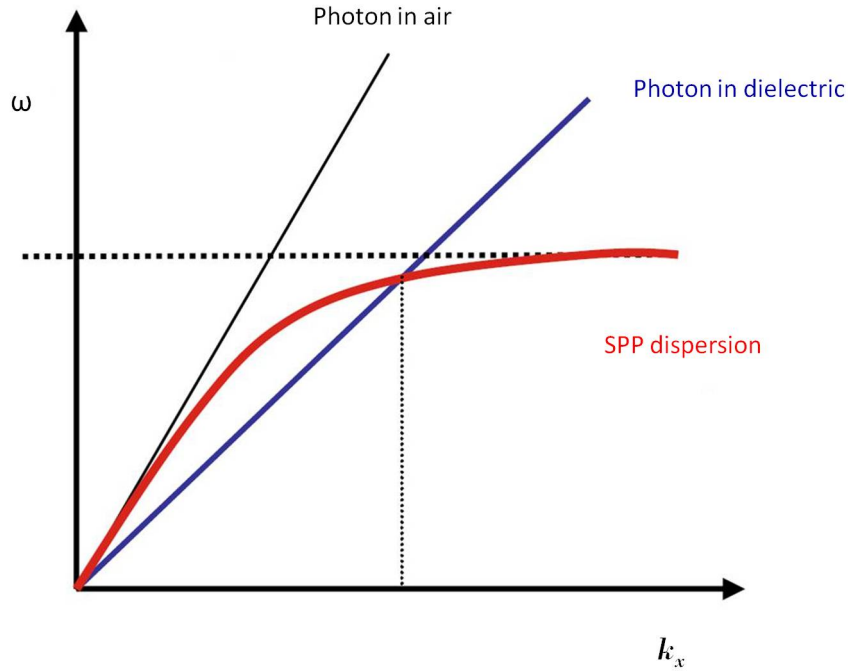
FIGURE 1.13: Disperion curves of light and SPPs. Generally, a momentum mismatch prevents an excitation of SPPs by light at a metal-vacuum interface. Adopted from [100].

reflection geometry. This way, SPPs are generated on the metal-vacuum interface.[91]. The in-plane component of the light wavevector in the dielectric coincides with the SPP wavevector on an vacuum-metal interface. As a result, the light is coupled to the SPPs. Figure 1.14 b) shows the two-layer geometry of the Kretschmann configuration. The dielectric layer between the prism and the metal film has a refractive index smaller than the one of the prism ($n_{prism} > n_L$). This geometry enables the excitation of SPPs on the internal metal interface at different incident angles θ_α. However, the Kretschmann configuration is not suitable for the excitation of SPPs on a thick metal film. The Otto configuration solves this problem by placing the prism close to the metal-vacuum interface (figure 1.14 c)). In this case, SPPs can be excited through the air gap between the prism and the surface[90]. By reducing the prism to a dielectric tip, the Otto configuration can also excite SPPs as illustrated in figure 1.14 d)[102, 103]. This can be realized by a scanning near-field optical spectroscopy tip, namely an optical fiber that is covered by a metal coating. In this configuration, SPPs can be provided locally on the metal surface (see section 1.4.2). On the other hand, the excitation of SPPs can also be achieved by employing diffraction gratings or a randomly rough surfaces (figure 1.14 e) and f)). Surface enhanced Raman spectroscopy, as well as tip-enhanced Raman spectroscopy will be discussed in detail in the following section.
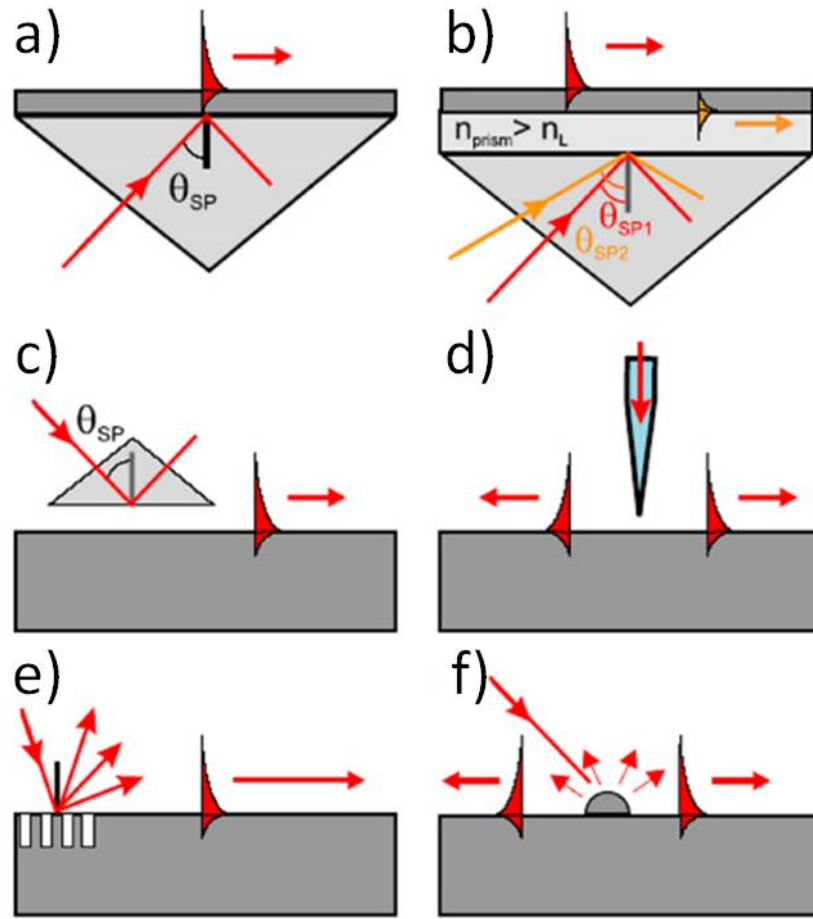
FIGURE 1.14: SPP excitation configurations: (a) Kretschmann geometry, (b) two-layer Kretschmann geometry, (c) Otto geometry, (d) excitation with a SNOM probe, (e) diffraction on a grating and (f) diffraction on surface features. Adopted from [101].

1.4.2 Scanning near-field optical spectroscopy

The concept of scanning near-field optical microscopy (SNOM) was introduced by Pohl et al. for the first time in 1984[104]. SNOM has become a powerful optical tool in the field of nanostructure investigation. One can not only get the optical image of the nanostructure, but also study their dielectric properties as well as gain spectroscopic information. For these applications, the technique of SNOM could be considered as a combination of optical microscopy and high resolution scanning probe microscopy (SPM).

Differently from the conventional optical microscopy, SNOM can overcome the diffraction limit by exploitation of non-propagating evanescent waves in the near-field zone of the light emitter (figure 1.15)[93–95]. In this regard, the development of SNOM makes it possible to investigate the properties of single molecules. At the same time, it retains

some important features of this technique, e.g. the possibility to investigate the nanostructure in their local field and more importantly, the ability to study the properties of an individual particle, like polarization, charge transport and geometry rearrangement. Moreover, SNOM also offers the oppotunity to scan over the sample and get a optical map of the scanning area.

Depending on the probe configuration, the SNOM can be roughly classified into aperture and apertureless probes. The aperture probe configuration was firstly realized in 1984 and is still commonly used (figure 1.16 a)). However, the inherent resolution of aperture probe SNOM is limited to about 20 nm and highly depends on the size of the fiber.

Apertureless probes (see figure 1.16 b)), as a promising alternative, have a larger potential for high resolution detection. For this method, the choice of the tip is decisive for the excitation of the SPPs. There are two categories of tips, the solid metal tips and the metal coated glass tips. The solid metal tips are externally illuminated by a focusing lens. In contrast, metal coated prisms could be internally illuminated to excite SPPs. The fabrication process, as well as the excitation mode of the metal coated prism will be discussed in detail in section 2.1.

Solid metal wires are widely used as an apertureless SNOM tip. As discussed in section 1.4.1, the solid metal wire, as a simplified rough surface or the hot spot on the surface, offers a high near-field intensity at the apex. Together with the development of the tip-enhanced Raman spectroscopy (TERS), different external illumination geometries have been proposed to optimize the field enhancement(see section 1.4.3). Bin Ren *et al.* have illustrated the general fabrication (etching) process for an efficient SNOM-metal tip[105]. The enhancing mechanism of the tip is normally discussed, to be a combination of the lightning rod effect and surface plasmon excitations. In our discussion, we mainly focus on the surface plasmon effect of the tip. There are three fundamental SPP modes
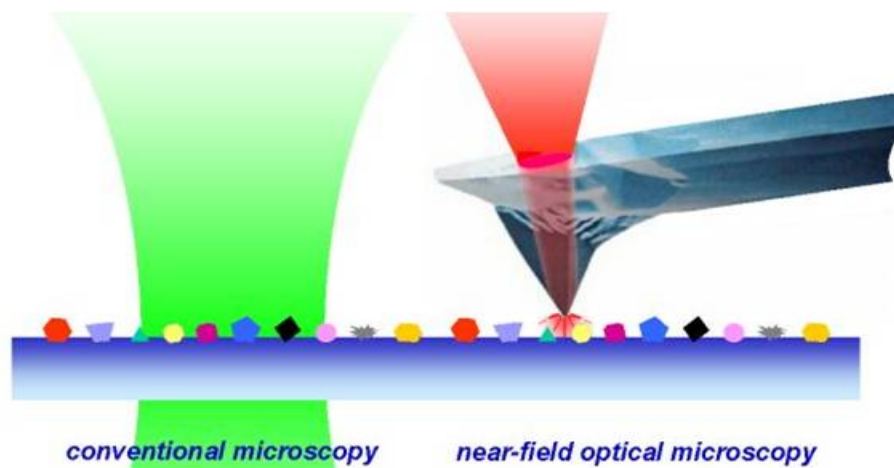

conventional microscopy   near-field optical microscopy

FIGURE 1.15: Conventional microscopy and near-field optical microscopy.

for solid metal tips. The modes are classified as transverse magnetic mode (TM) and two other hybrid modes(HE_1 and HE_2). Among them, the TM-SPP mode is proposed to be the most efficient mode for tip-enhanced Raman spectroscopy. The TM-SPP mode could be generated in any of the illumination geometries.
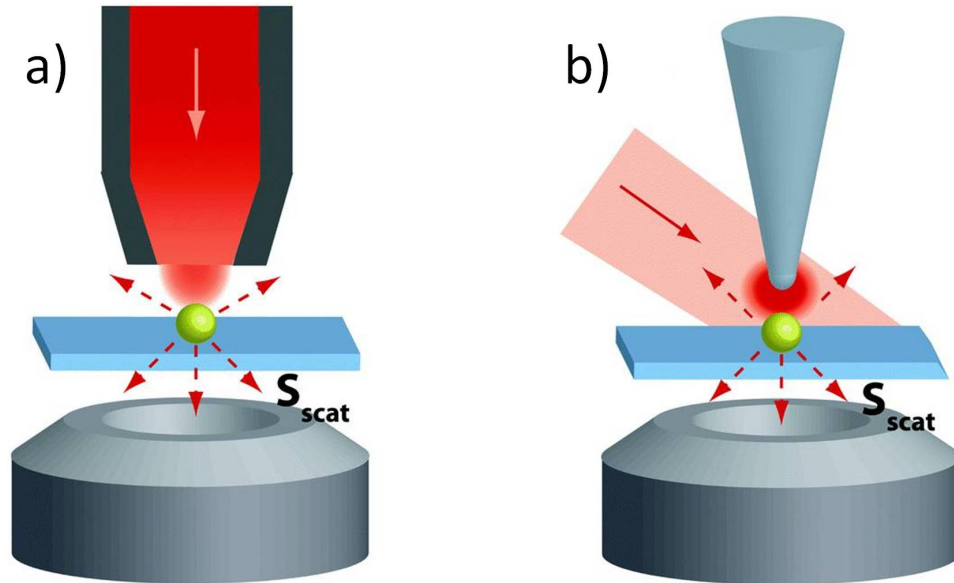

FIGURE 1.16: Schematic geometry of scanning near-field optical microscopy (SNOM) of a single nano-object: a) aperture SNOM in illumination mode where the evanescent wave emerging from the tip is scattered by the object into far-field radiation, part of which is collected by a detector. b) Apertureless SNOM with a side illumination mode. The scattered light is collected by the objective below the sample. Adopted from [106].

Besides the solid metal tip, a metal-coated dielectric probe is also considered to be efficient for the excitation of SPPs. For this probe, the tip is illuminated from the inside, using a top illumination geometry. The metal-coated dielectric tip has two dielectric-metal interfaces, usable for the excitation of SPPs. Along the metal-glass interface, the SPPs is excited during the internal illumination process. Besides, the normal SPPs mode is excited at the metal-air interface.

1.4.3 Optical geometries for TERS

With the development of TERS, different methods were applied to get an enhanced Raman signal from the apex of the tip efficiently and conveniently. We will focus on the illumination channel and the collection efficiency in this chapter.

The most popular methods, bottom-, side- and top-illumination are shown in figure 1.17, and will be discussed in the following. The numerical aperture(NA) of the objectives is an important factor for a high collection efficiency in the TERS experiments[107, 108]. Bottom illumination is the only method that can use oil immersion objectives and

achieves very high NAs of up to $1.4 - 1.6$. However, for the top or side illumination method, objectives with considerable working distances have to be used. Here, objectives with NAs typically ranging from 0.28 to 0.85 have been used in the top-illumination scheme[109]. Besides the methods above, parabolic mirrors (PM) as focusing elements enable an alternative top illumination to reach a NA of approx. 1.

Focusing the laser on the apex of the tip is also an important factor concerning the NA of the objective. A high NA offers a smaller diffraction limited laser spot and the spot can be accurately focused on the apex of the tip, which increases the Raman intensity and reduces simultaneously the far field background.

Bottom illumination

The earliest TERS experiments mainly used the bottom-illumination geometry[110–112]. In these studies, an objective was placed under a transparent substrate at the bottom. The tip can be approached and retracted from the substrate. As shown in figure 1.17 a), the objective at the bottom is focused on the connection point of the tip and the substrate[113]. AFM is normally used to control the gap between the tip and the substrate, but STM feedback is also used in this bottom illumination configuration with the help of optically transparent, conducting substrates like indium tin oxide (ITO) or thin gold films[114, 115]. However, two other factors highly influence the collecting efficiency, the transparency of the substrate and the loss of Raman signal which is emitted into the substrate.

Side illumination

The first side-illuminated TERS instrument has been presented in 2001 to dispose of the transparent substrate[116]. Shortly after this experiment, several other experiments were reported with side illumination and collection[117–120]. In these set-ups, long working distance objectives were placed with angles between $45 - 70°$ relative to the tip axis. As shown in figure 1.17 b), long working distance objectives are required to reach the tip and the sample, thus the NA of the objectives is in a range between 0.28 and 0.55. The limit for the choice of the objective is the main drawback of this method. The collection potential of these systems is limited by the small collection angle of the lenses. The advantage of this method is the is the variety of possible substrates.

Top illumination

As shown in figure 1.17 d), the objective is placed right above the tip. Using this geometry, one can illuminate the tip and collect the Raman signal right above the substrate. This method combines the advantages from both, side and bottom illumination. The NA of the objective in this method can be increased up to 1 and the laser be focused
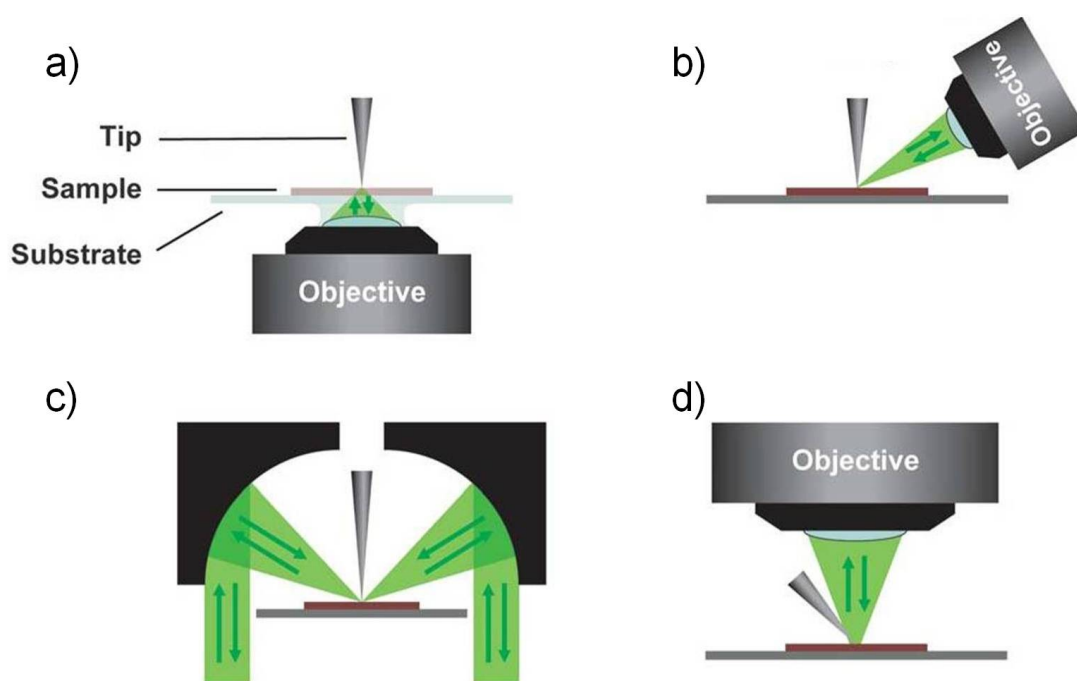
FIGURE 1.17: Illustration of the different possible illumination and detection geometries for tip-enhanced Raman spectroscopy. a) Standard bottom illumination, b) side illumination, c) top illumination with a parabolic, d) top illumination with a lens. Adopted from [108]

symmetrically on top of the tip. Additionally, the substrate can be chosen freely as for the side illumination. Non-transparent substrates can reflect the Raman signal emitted into the substrate.

Besides the application of the fully metal coated glass tip as an apertureless SNOM-tip, it can be operated in top-illumination geometry, where the tip is internal illuminated by the incident beam from the top. The tetrahedral SNOM-tip has been introduced by Fischer *et al.*[121] in 1993 for near-field microscopy studies. The T-tip is employed as an optical channel for illuminating the apex of T-tip through its glass body as well as collecting the back scattered light. In this thesis, we employ this T-tip in our molecular junction set-up with a top illumination geometry. Detailed information for this method will be given in section 2.1.

Parabolic mirror based focusing

Near-field measurements, using a parabolic mirror, were firstly proformed in 2003[122]. Similar as the application of the T-tip, this method was used to do the TERS experiments in 2007[123–125]. As shown in figure 1.17 c), a small hole is drilled in the center of the parabolic mirror. The tip controlled by the piezo tube is placed within this small hole. The incident light is focused by the parabolic mirror around the tip, and the Raman

scattered light is collected using the same pathway. In this configuration, the maximum of the Raman signal scattering is supposed to be collected without employing an oil imersion objective.

1.4.4 Raman spectroscopy of individal molecules

Enhanced Raman spectroscopy offers the possibility to study the properties of a small sample volume. Information related to the topography, vibrational states, or even charge distribution of individual molecules can be obtained by the Raman spectra. Moreover, the impact from the environment can also be detected by Raman spectroscpy (figure 1.18). In this section, we mainly focus on the spectral changes as well as effects of charging of a single molecule.

Selection rules of Raman scattering

The Raman scattering of a molecule is composed of bands representing some active normal vibrations. Groups of atoms have certain characteristic vibrations in the Raman spectra, which provide a unique spectral fingerprint of a material. For individal molecules, the observed Raman spectrum depends on the masses of the atoms in the molecule, the strength of their chemical bonds and the atomic arrangement[126, 127]. In this respect, the Raman scattering is dependent on selection rules. During the interaction between a molecule and a photon the total angular momentum in the electronic ground state has to be conserved. As a consequence of this requirement only specific vibrational transitions are possible.

A Raman active vibration can be detected if the polarizability α in a molecule is changed during the vibration. The intensity of a Raman active band I$_{Raman}$ depends on the change of polarizability α during this vibration:

$$I_{Raman} \propto \left(\frac{\partial \alpha}{\partial q}\right)_0^2 \tag{1.15}$$

where q is the normal coordinate.

The Raman selection rule is analogous to the selection rule for an infrared-active vibration, meaning that there must be a net change in permanent dipole moment during the vibration. If a molecule has a center of symmetry, vibrations that are Raman active will be silent in the infrared, and vice versa. Scattering intensity is proportional to the square of the induced dipole moment, i.e., to the square of the polarizability derivative. As a consequence of the selection rules, Raman spectroscopy contributes to the characterization of the carbon backbone of organic substances or polymers.
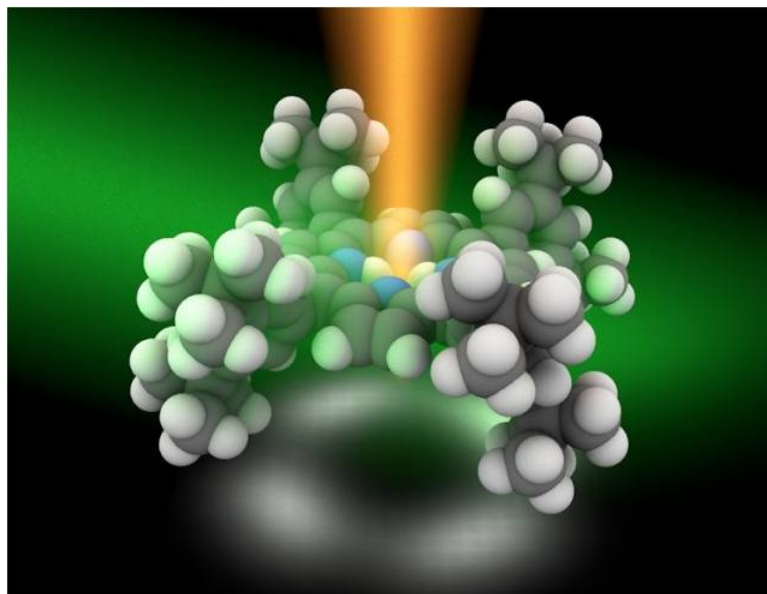
FIGURE 1.18: Raman detection of a single molecule. Adopted from [131]

Raman spectra of individual molecules

Towards the direction of the single molecular Raman spectroscopy detection, there are always two major questions: (1) Whether the signal of the collected spectrum originates from a single molecule or from an ensemble, (2) whether the low intensity of the observed Raman spectra is due to the low amount of molecules or bleaching of the organic molecules. [128]

Despite previous single-molecule SERS experiment, first attempts of single-molecule TERS were published at around 2006. Malachite green and malachite green isothiocyanate were used for these studies[117, 129]. The observed spectra showed large fluctuations in signal intensities and peak positions. A single molecule moving within the enhancement zone, and electric field gradient effects were thought to be the explanation for these fluctuations[130]. Bleaching behavior in the TERS measurement should also be concerned. Later, Zenobi's group chose another molecular system to investigate the single-molecule Raman spectra and to observe the single molecular spectrum fluctuation of brilliant cresyl blue[130].

In 2007, Pettinger opened the discussion whether the observed Raman spectra fluctuation come from a single molecules or from carbon fragments[128]. In their discussion, some of the reported result, which claim the obosservation of possible Raman spectra fluctuation, could be demonstrated to come from carbon fragments. Organic molecules under the tip can be easily destroyed in the strong optical field and in the presence of oxygen and can turn into undefined carbon fragments.

Except for the achievements in early years, different groups keep finding evidence for single-molecule TERS. Recently, R. Zhang *et al.* presented their observations of single molecular TERS of an isolated H2TBPP(figure 1.18). They ascribe the different signal strengths to different positions on top of the single molecule[131]. Earlier, Zheng Liu *et al.* proposed the application of their fishing mode STM for single-molecule STM. They also observed the spectral fluctuations[132]. Besides, the combination of TERS and MCBJ also offers the evidence of single-molecule Raman spectroscopy[133].

Moreover, charge transfer processes are also considered to potentially influence the Raman spectra of the single-molecule junctions. Electron transport through the molecular junction will definitly involve the electrons in the frontier molecular orbital. For the former single-molecule SERS studies, charge transfer could be understood in a manner that electrons in the HOMO could transfer to the Fermi-level of the metal substrate or to the LUMO of the same molecule. As a result, the ratio of Anti-stokes and Stokes Raman intensity will increase[134]. For a TERS experiment, there is also the possibility that electron transfer from the tip to the substrate, and the molecule as the conduction channel, or vice versa. Moreover, mechanically controlled single-molecule junctions were studied with near-field Raman spectroscopy in order to determine the influence of the charge transfer on the Raman spectrum. In 2007, Daniel R. Ward *et al.* reported a series of experiment on the simultaneous measurements of electronic conduction and Raman response in molecule junctions[135, 136]. In their work, the intensity of the Raman modes and the change of mode positions are suggested to be the result of charge transport through the single-molecule junction. Furthermore, they ascribed these effects to changes in conformation and binding of an individual molecule. Jing-Hua Tian *et al.* also reported that an increased Raman intensity for a conducting single-molecule junction[133]. More recently, different methods were developed in order to study the charge transport process by its influence on the Raman spectrum. Unfortunately, more clear evidence and better interpretations are still required.

Chapter 2

Experimental Procedures

In the beginning of this chapter, the so called tetrahedral SNOM-tip (T-tip), whose SPPs modes have been briefly discussed in section 1.4.2, will be introduced. The T-tip is employed as a tool to probe the electrical conductance and as an optical channel for Raman investigations of the single-molecule junction between the tip and the substrate. In section 2.2, the set-up is introduced in detail from the inner part to the entire optical system. The electronical part and the optical part for the TERS measurements are separately introduced. In section 2.3, the molecular junction spectroscopy (MJS) system is tested in the electrical and optical configurations. An atomic sharp SNOM-tip is characterized by conductance quantization[25, 28]. The optical properties, including the laser coupling efficiency and the tip enhancement, are evaluated and compared with previous work in section 2.3.

2.1   Fabrication process of the T-tip

In this section, the fabrication and the properties of the tetrahedral SNOM-tip will be discussed with an emphasis on its application for enhanced Raman spectroscopy.

Fabrication process of the T-tip

The SNOM-tip consists of a tetrahedral dielectric glass body and a metallic cover layer. Three sides including the apex of the tip are covered with a thin metal film. The glass body of the T-tip consists of microscope glass cover slips bought from Thermoscientific/ESCO with a size of 22×22 mm^2 and a thickness of ~ 0.25 mm. Before the fabrication process, every cover slip is cleaned with a special cleaning process, in order to remove any organic contamination on the T-tips. Firstly, the glass is placed on top of a heating plate, and heated to $310 - 320$ K. Afterwards, CO_2 gas is led through a so
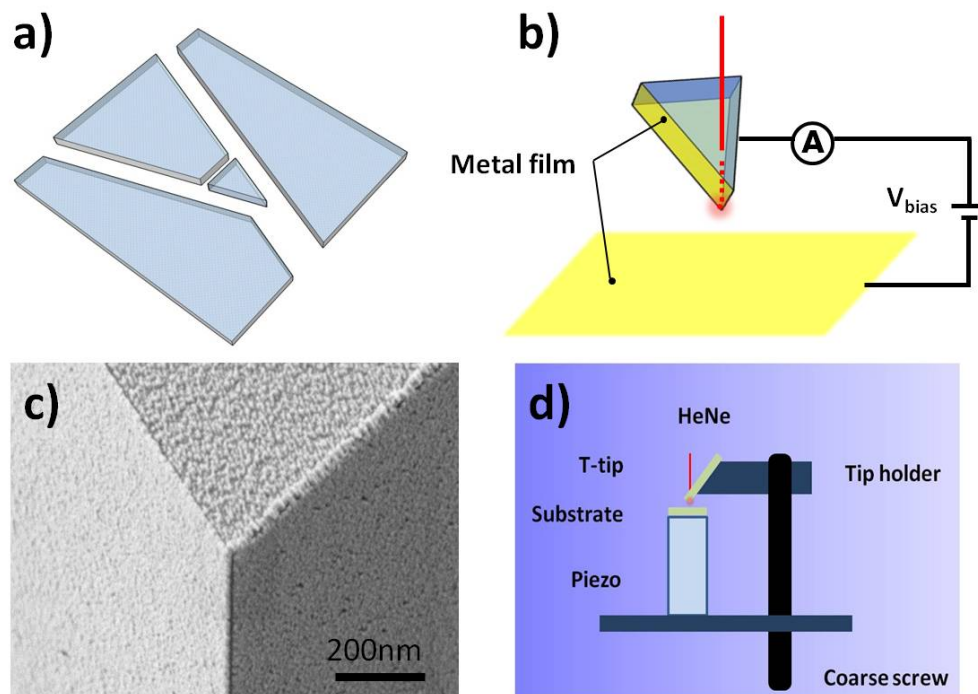
FIGURE 2.1: The tetrahedral SNOM-tip. (a) Cleaving process of the glass fragment. (b) Tip illuminated from the backside and used as an apertureless near-field emitting counter electrode. (c) SEM image of the T-tip. (d) Schematic of T-tip fixed on the holder.

called snow jet pistol (Applied Surface Technologies) which creates small dry CO_2 ice particles in a high velocity gas stream. The contaminations on the substrate, especially the hydrocarbon-based contaminations as well as small particles on the glass cover slide, are cleaned by this dry CO_2 flow. The cover slip is heated to prevent water condensing on the surface, which is considerably cooled down during the exposure to the snow jet. After the cleaning procedure, the cleavage process is performed manually. Figure 2.1 a) shows a sketch of the cleavage process. The cleaned glass cover slip is slightly scratched with a diamond cutter at two edges that include an angle of about $90°$. This angle can be varied to adjust the sharpness of the tip. By breaking the glass carefully along this edges, a glass prism of $3 - 5$ mm side length, with an atomically sharp apex, is formed. The tips are subsequently coated with an amouphous gold layer with variable thickness. In our experiment, the evaporated thickness is chosen to be around 14 nm, the minimal thickness to be still conducting. The evaporation process is preformed in an evaporation chamber (Leybold) at a base pressure of 10^{-8} mbar at room temperature. The thickness of the metal coating on the edges and on the planes strongly depends on the incident angle of the metal beam with respect to the surface of the sides of the glass fragment. A variety of metals can be chosen for the conductive layer or for the TERS measurement. Gold is used on the one hand because of its chemical inertness, on the other hand because the molecules used in the experiments bind covalently to gold.

Notably, the thickness of the gold film influences the conductivity and the near-field intensity achieved at the apex of the tip. According to the discussion above, a thinner layer of the gold film result in a better local plasmon intensity at the apex of the tip. The scanning electron microscope (SEM) image of Figure 2.1 c) shows a rough gold layer. During the experiment, the T-tip is fixed on the tip holder in a similar angle as it was fabricated, shown in figure 2.1 d). The operational process will be discussed in section 2.2.

Properties of the T-tip
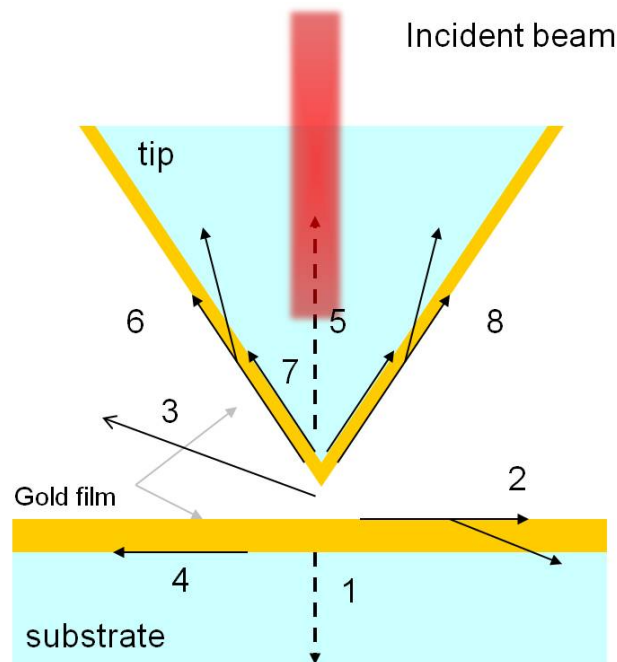
FIGURE 2.2: Plasmon modes along the tetrahedral SNOM-tip. The tip is illuminated from the inside exciting different plasmon modes. For signal detection radiative channels are required, these are the channels 1,3,5, which are detectable in the far field. The leaky modes (branched arrows 2,6,8) are also efficient detection channels for tip-enhanced Raman spectroscopy, in contrast to the non radiative modes (4,7) which are dissipative and not accessible in the optical far field. Adopted from [137].

The T-tip introduced here, as a scattering type or apertureless SNOM-tip, has been introduced by U. C. Fischer *et al.* in 1993 for the first time[121]. Later, the group of Fischer applied the T-tip in the field of TERS measurements. The basic idea of the T-tip is, to create a light source that is intrinsically smaller than the diffraction limited focus of far-field optics. Bortchagovsky *et al.*[137] demonstrated the potential application for the T-tip, not only as SPPs source but also as the collecting channel. A lateral optical resolution of 10 nm was achieved by Koglin *et al.*[139]
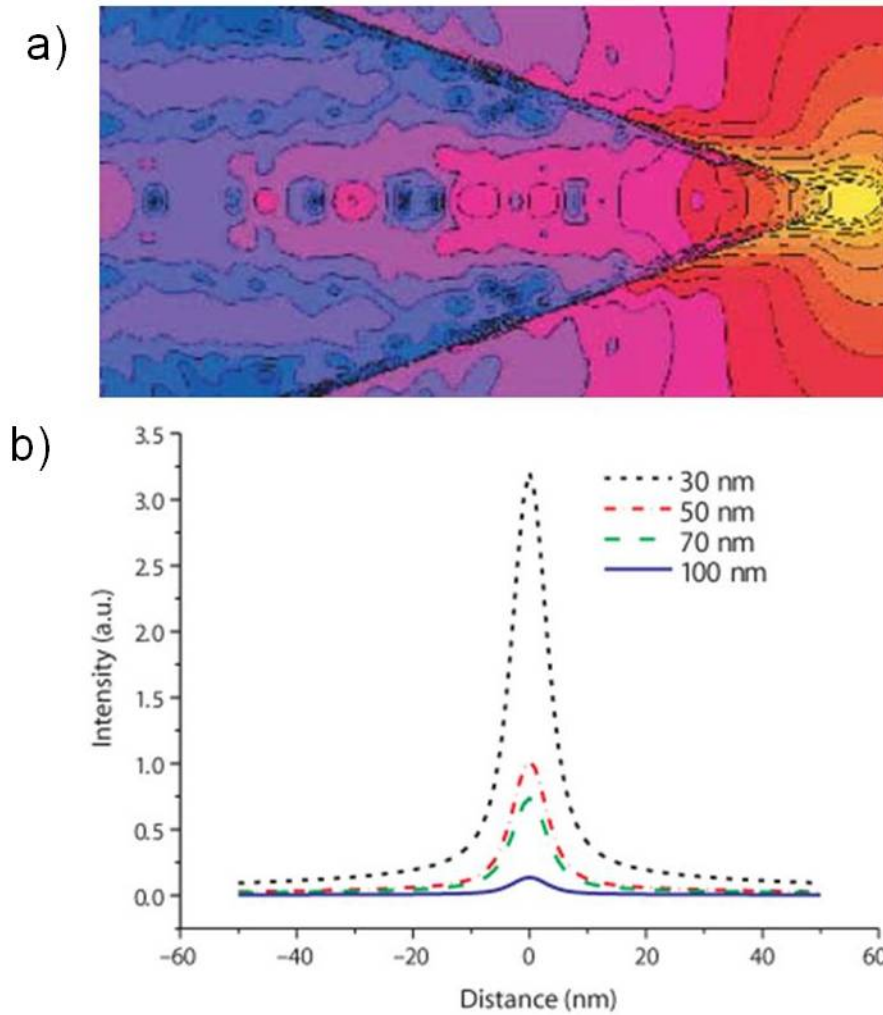
FIGURE 2.3: a) Intensity distribution at the end of a gold-coated glass tip. b) Thickness dependence of the near-field intensity at the apex of the tip. Adopted from [138].

SPPs are efficiently coupled into the planes and edges of the tip and converges at the apex of the tip. By contrast, external illumination of the bare metal tips always creates a bigger far field background. Thus, the tetrahedral tip has a reduced background radiation as well as a reduced photo bleaching of the entire sample. In the following, different detection pathways of the tip for optical spectroscopy are presented and discussed. As a SNOM-probe the tetrahedral tip provides access to signal detection from the metal substrate surface to the optical far field. Bortchagovsky *et al.*[137] specified signal detection channels for different experimental configurations, using the T-tip depicted in figure 2.2. Channel 5 shows the direct radiation into the tip. Beside this, the reflection of the channel 1 will also contribute to channel 5 if the gold substrate is thick enough. The two major leaky edge modes of the tip are channel 6 and channel 8. These two modes are suggested by Bortchagovsky *et al.* to be an efficient signal mediator for Raman spectroscopy on the molecular level[137]. A non-radiative SP 7 propagates along the metal-dielectric interface. This mode acts as the waveguide mode that could couple

to the SPPs mode at the gold-vacuum interface. Channel 1, 2 and 4 are the modes that propagate along the substrate.

For the excitation of SPP modes, there are two interfaces involved: 1) The inside interface between the gold layer and the glass body, and 2) the outside surface of the gold layer and the vacuum. Due to the top illumination geometry, the waveguide mode at the inside interface and the SPP modes outside the gold coated layer are excited and converge towards the apex of the tip, where they create a highly intense and localized optical field.

Figure 2.3 a) shows the distribution of the transverse field on a plane perpendicular to the tip axis. At the same time, they investigated four different thicknesses of the gold layer and evaluated the field on a line transverse to the tip axis and beneath the tip[138, 140, 141]. The resulting curves are shown in figure 2.3 b). They found that a thinner layer of gold provides a stronger field enhancement. However, the penetration through a thin layer is also stronger, hence a thin layer leads to a larger far-field background. By contrast, for a thick coating the penetration is much weaker leading to less far-field background, but also to a much weaker field enhancement[138, 142, 143]. In other experiments, a much thinner gold film yielded a better near-field intensity as well[137, 140, 141].

Besides this, significant efforts have been made within the past decade to understand the optical and plasmonic properties of the tetrahedral SNOM-tip[108, 144–147]. The evaluation of the field distribution and the near-field intensity at the apex of the tip is still investigated. For an early work in our group, the near-field intensity at the apex of the tip with a value of 3.5 kW / cm^2 is deduced for the first time. In that experiment, a solar cell using a single bio-molecule was realized for the first time[148].

2.2 Experimental set-up

2.2.1 The experimental configuration

The set-up, which allows the investigation of covalently bonded single molecules in a strong optical field, is called a molecular junction spectroscopy (MJS) set-up. Figure 2.4 shows the set-up with the already described SNOM-tip acting as a counter electrode and as a local light source at the same time. A gold substrate with immobilized molecules is fixed on a high precision piezo crystal and a sample holder with the SNOM-tip is placed above the substrate. Both components are situated inside a UHV chamber. A sourcemeter serves as a DC voltage source and measures the current.

A HeNe laser(12 mW, 632.8 nm) is employed during the experiments. The laser is first filtered by a line filter. Several removable neutral density filters are used to adjust the beam intensity. Subsequently, the filtered laser beam is converged to the multi-mode fiber, and at the other end of the fiber collimated by an objective. The parallel laser beam is then reflected by a 45 degree assembled dichroic beamsplitter(Semrock, RazorEdge Dichroic^{TM} laser-flat beamsplitter, $LPD01 - 633RU - 25$), perpendicular through a quartz viewport into the UHV chamber. The laser is focused by a moveable, high numerical aperture objective (NA = 0.8, Olympus) through the glass body into the apex of the tip. The objective is mounted on X, Y, Z linear piezo actuators (attocube systems AG, Linear positioners $2 \times$ ANPx101NUM, $1 \times$ ANPz101NUM and Piezo controller ANC 35) which allows a maximum displacement of 5 mm. The light originating from the junction is then recollected through the same objective. Consequently, one has to separate the inelastically scattered light of the junction from the laser light. This is done by the dichroic beamsplitter in the first place. The inelastically scattered light can pass through the beamsplitter while the laser light is reflected. Afterwards, the scattered light propagates through a lens which produces a real-time image of the sample on a CCD camera. When focusing the laser to the apex of the T-tip by adjusting the X, Y and Z pizeo, a removable 45 degree slant mirror is placed above the lens to reflect the image of the sample into a camera. After adjustment, the mirror is removed and the signal propagates through a notch filter(Semrock, StopLine single-notch filter, $NF03 - 633E - 25$), which is designed to absorb all remaining light of the incident laser. In the end, the signal is focused by an objective into a multi-mode optical fiber, and then collected by a spectrometer (Prinston Instruments, Acton Series Monochromators and Spectrographs, $Spectra - pro$ $2310i$) with a highly effcicient liquid N_2 cooled CCD for optical analysis.
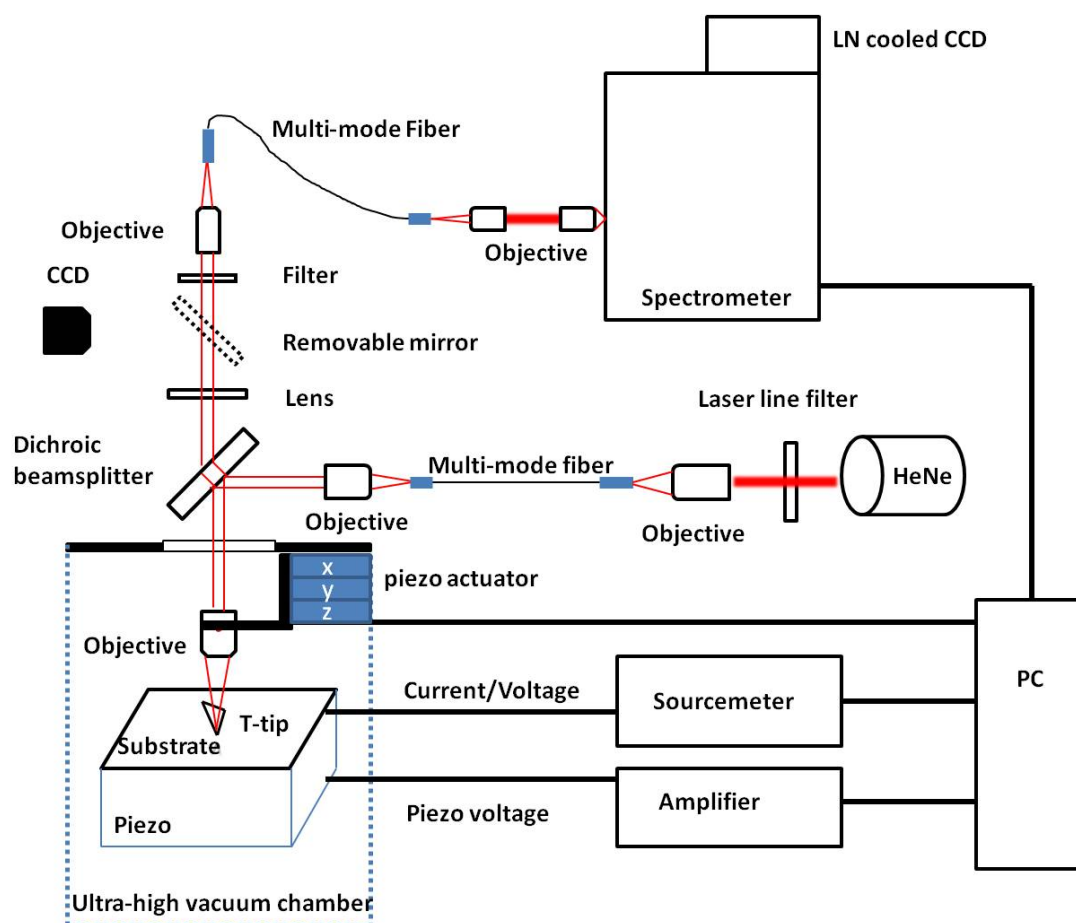
FIGURE 2.4: Schematic illustration of the MJS set-up. The SNOM-tip acts as a counter electrode and a light source at the same time. Light is coupled into the T-tip by an adjustable microscope objective. The back scattered light is collected and guided to the spectrograph, where the light is spectrally analyzed. The metal substrate is fixed on top of a low-temperature high precision piezo. To accurately control the distance between tip and substrate, the piezo can be feed-backed on a given tunneling current. Current-voltage characteristics are recorded by a sourcemeter. Vacuum conditions are established, to avoid adsorbent layers and oxygenation of molecules in high optical fields.

Cryostat / UHV-chamber

The experiments are performed under high vacuum (UHV) conditions at room temperature to prevent any adsorbent layers on the substrate or oxygenation of molecules in the high optical fields. A turbo molecular pump system (TPU 060 from Balzers/Pfeiffer) and a rotary pump (Edwards) are attached to the chamber, generating a base pressure of 10^{-8} mbar. The sample holder is mounted on top of the cryostat inside the UHV chamber as depicted in figure 2.5. With a commercially available He flow cryostat (Cryovac), low-temperature measurements down to 30 K can be realized.

Sample holder
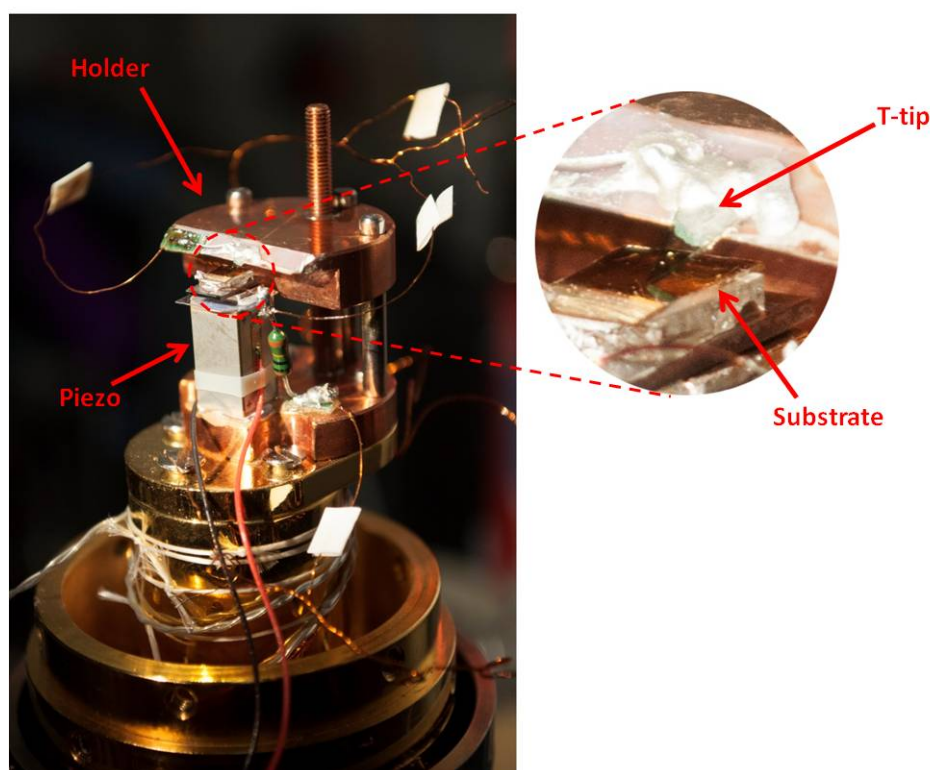
FIGURE 2.5: Image of the home-built MJS set-up. The sample holder is positioned on the top of a helium flow cryostat. The T-tip is fixed on the sample holder. The enlarged image shows the T-tip and the substrate.

As illustrated in figure 2.5 the molecular junction is formed between a tip in a fixed position and a moveable planar substrate. The planar substrate can be moved in vertical direction to control the tip-sample distance in a range below 12 μm. As depicted in figure 2.5, the surface where the SNOM-tip is mounted is tilted, to ensure that only the apex of the SNOM-tip gets in touch with molecules and not the whole cleaved edge. This surface is covered with an insulating glass plate which is glued onto the copper holder. The SNOM-tip is glued onto the glass plate in a way, that the apex sticks out about 1

mm. For the connection to macroscopic leads a copper wire is fixed with colloidal liquid silver to the SNOM-tip, that leads to the sourcemeter. A fine thread enables a coarse manual adjustment from outside of the chamber for the tip-sample distance. The fine thread is composed of two ends with different screw threads, thus the difference between the threading defines the height change per rotation. The fine thread is required to approach the SNOM-tip to the substrate to a distance smaller than 12 μm, the working distance of the piezo crystal. The pitch of the thread is 150 μm for one rotation of 360°, that corresponds to a height difference of 2.1 μm, when the fine thread is turned 5° by the rotary feedthrough.

Piezo control

A low-temperature high precision piezo crystal (Physik Instrumente(PI)) is used to position the sample laterally with respect to the tip. The substrate is fixed on an electrically isolating layer. Since the SNOM-tip and the substrate are metal-coated the distance can be controlled by a STM feedback technique which is based on the tunneling effect. The tunneling current I_{tunnel} through a rectangular barrier for voltages lower than the work function of the gold electrodes is described in a good approximation by an exponential dependence which is exploited by common scanning probe techniques such as STM, SNOM and AFM. For such scanning probe technique, it is difficult to keep a tip over a molecule at a fixed position without any thermal drifts in the time window of tens of seconds. By sacrificing the ability to scan over the surface, but one gains the mechanical stability that enables single-molecule transport measurements in the time range of several tens of seconds. The operating voltage of the piezo ranges from 0 to 90 V, realized with a home built high voltage amplifier with a voltage resolution of 3 mV that corresponds to a step size of about 0.0018 nm.

Sourcemeter

A sourcemeter from *AgilentTechnologies* (model *E5263A*) with a high speed medium power source measuring unit (MPSMU) acts as a DC high precision voltage source. The resolution of the voltage output up to ±2 V is ±0.1 mV. This sourcemeter is accessed via GPIB with a computer and shows a current measuring accuracy of ∼ 5 pA up to a limit of 100 nA. The current detection limit for the given set-up is < 1 pA. By applying a voltage between SNOM-tip and substrate current-voltage characteristics are measured and time-averaged in units of power line cycles (PLC). During a PLC 128 samples are measured and averaged for each voltage step. The minimum integration time is 100 μs and the maximum number of steps is 1001 per voltage sweep measurement. The typical acquisition time for current-voltage characteristics is 10 − 30 s.

2.2.2 Operational procedures

Preparation of the sample

The fabrication process of the glass substrate is generally the same as for the T-tip except the geometry which is given by a square plane (5×5 mm^2). The glass slide is coated with a $50 - 100$ nm gold film, whose roughness is about $20 - 30$ nm. A droplet of the molecular solution is deposited with a pipette on the gold covered substrate. Then the substrate is put in an atmosphere saturated with the solvent (tetrahydrofurane) for three hours which leads to a self-assembly of the molecules anchored covalently to the substrate. The formation of a self-assembled molecular layer covalently anchored to the substrate. During the exposure time, the acetyl protection groups of the molecule split off, and the sulfur covalently bonds to the gold surface on one side. Meanwhile, the other side of the molecule remains acetyl-protected.

Transport measurement
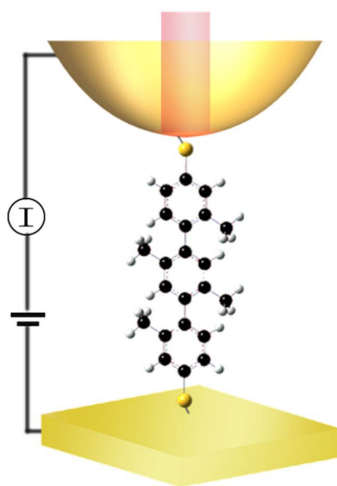
FIGURE 2.6: Scheme of the single-molecule junction. The molecule is [(2,2',2'',5'-tetramethyl-[1,1':4',1''-terphenyl]-4,4''-diyl)bis(methylsulfane)] which is covalently bound between the gold coverd T-tip and the gold substrate.

The T-tip is fixed to the sample holder with conductive glue at an angle of $45°$. The substrate is magnetically attached to the pizeo. A sourcemeter serves as a DC voltage source and measures simultaneously the current in the circuit which consists of the T-tip, the substrate and the probed molecule (figure 2.6).

In a first rough approach, in order to bring the tip into the working distance of the piezo, the distance is controlled by a home-built feedback electronic. The feedback loop withdraws the sample, as soon as the tunneling current between tip and sample exceeds a specific set point while the tip is approached mechanically with a differential screw

towards the sample. The main difference to the common STM set-up is, that the piezo can only move in vertical direction to minimize drift effects and ensures a high stability of the molecular junction.

After the coarse approach, the piezo voltage is controlled manually to bring the electrode close to the tip. At small distances, the resistance of the junction decreases exponentially with the distance as the tunneling effect depends exponentially on the width of the tunneling barrier. At a certain distance, one can observe a steplike increase in current and the current becomes stable, indicating that a molecular junction formed between tip and sample. When the metal-molecule-metal contact has stabilized, current voltage characteristics can be recorded by sweeping the bias voltage in a given range (normally ± 1 to ± 2 V) and recording the current simultaneously.

Focusing the laser

Because we use a objective with a high numerical aperture for focusing and collecting the back scattered light, the focused laser spot is very small (with a the radius ~ 5 μm). At the same time, the image of the apex of the tip in the CCD camera is a combination of reflections from the upside of the tip, the gold coated layer, the prism interfaces and the tips mirror image on the substate. For a highly efficient signal collection, one has to focus right on the apex of the tip. After the optimization of the objective position, the Raman signal propagates along the optical route described above and finally gets analyzed in a spectrometer.

2.3 Test experiments

To characterize the MJS set-up for the further experiments, a series of electrical and optical experiments have been carried out. The ability to build a molecular junction stable enough for the further experiments are demonstrated by conductance quantization in single atomic gold contacts (section 2.3.1). The optical properties of the MJS set-up are characterized by the TERS of a monolayer of malachite green isothiocyanate(MGITC) (section 2.3.3).

2.3.1 Tip-substrate distance stability

For a molecular junction set-up, an atomically sharp tip are required to ensure that only a few or single molecules are bridging the junction. In order to test the stability and sensitivity of our set-up, we measured the conductance of a gold point contact formed between tip and sample. The amorphous gold film on the T-tip ($\sim$ 20 nm) and the

substrate ($\sim$ 100 nm) were prepared by thermal evaporation. A DC-voltage of 10 mV was applied between the gold substrate and the T-tip. Subsequently, a metallic contact between the tip and the sample is formed and broken afterwards.

Figure 2.7 shows the conductance when slowly breaking the gold-gold junction. The conductance is shown in dependence of the time as well as the piezo voltage to demonstrate the stability of the set-up. When slowly retracting the gold substrate, conductance quantization in multiple integers of $G_0 = \dfrac{2e^2}{\hbar}$ (where e is the charge of an electron and $\hbar$ is the Planck constant) is observed. The conductance curves show pronounced stairlike features at 1 G_0 to 5 G_0 (Figure 2.7). This conductance quantization occurs when the size of a metallic contact is much smaller than the wavelength of the electrons at the fermi level. This result indicates an atomically sharp contact between tip and substrate, as well as mechanical stability of the set-up.
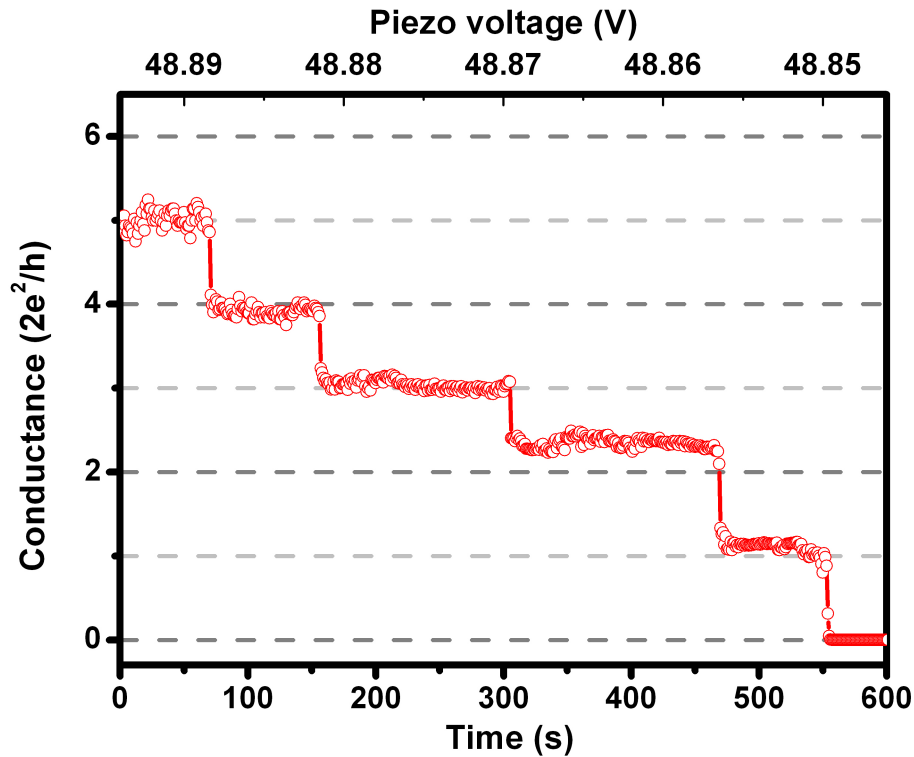
FIGURE 2.7: Conductance quantization of a gold quantum point contact, formed between tip and sample.

2.3.2 Interferometric calibration of the tip-sample distance

To test the optical part of the set-up, a first preliminary experiment to estimate the efficiency of the light coupling was carried out with the HeNe laser. The experiment begin with a metalic contact between the tip and the substrate. The incident red beam
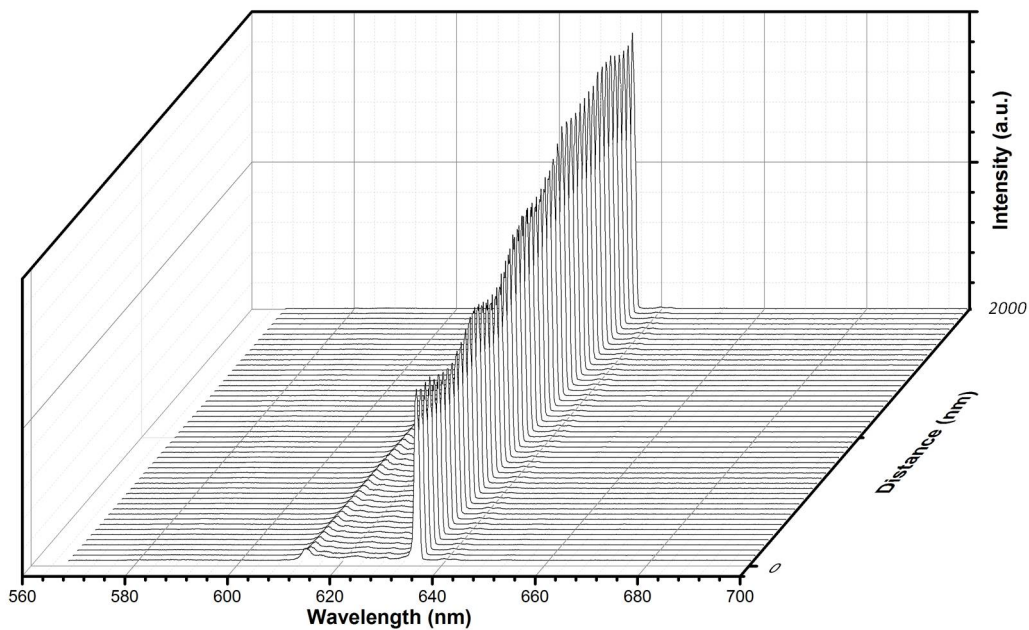
FIGURE 2.8: Standing wave behavior when the substrate removed from the tip in the far field.
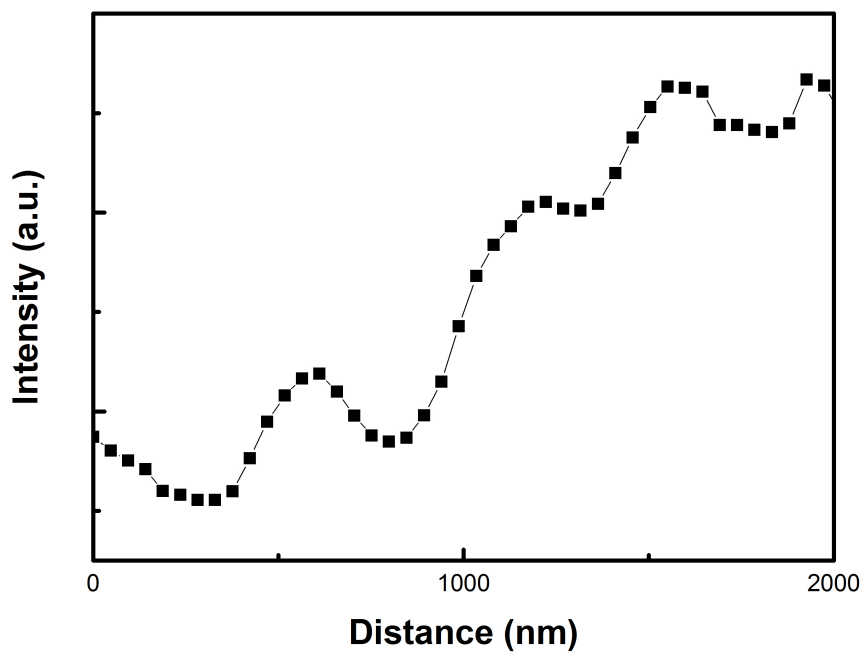
FIGURE 2.9: Laser intensity in dependence of the substrate-tip distance.

is focused on the tip and the back reflected light is collected with the optical part of MJS set-up. The back reflected light is recorded every 40 nm from an atomic connection up to 2 μm.

Figure 2.8 shows spectra in dependence of the tip-sample distance. An optical standing wave pattern is identifiable, which can be attributed to specific distances between tip and substrate where the distance fits with multiples of the excitation wavelength. In case of a minimum in the absorption, the wavelength or its multiples do not fit in to the given tip-sample distance in contrast to a maximum absorption, where a standing wave between tip and substrate is formed. Figure 2.9 shows the absolute value of the peak intensity (633nm). The peak periodicity is used to calibrate the piezo constant which consequently results in a working distance of the piezo of about 12 μm. This result coincides well with the data sheet value of the piezo. To conclude, the measurements reveal that light is coupled into the apex, resulting in a standing wave pattern between tip and sample. Furthermore, the data indicates that the set-up is spectroscopically sensitive to the region between the SNOM-tip and the sample at the length scale up to several microns.

2.3.3 Field enhancement of the T-tip

To characterize the near-field at the apex of the T-tip, Raman spectroscopy has been performed with a monolayer of malachite green isothiocyanate(MGTIC) adsorbed on an amorphous gold substrate. For a long time, MGTIC has been used for the investigation of TERS, due to its high Raman cross-section. Pettinger *et al*. reported the single molecular Raman spectroscopy detection with this molecule[149]. U. C. Fischer *et al*. also characterized the T-tip with this molecule[142]. For the formation of a sub-monolayer of dye molecules, the substrate was wetted with a droplet of a 1 mM ethanolic MGITC dye solution, which dried off quickly. During the drying of the droplet, the dye was adsorbed irreversibly at the metal substrate through its sulfur atom. Subsequently, the crystal was rinsed with copious amounts of ethanol, to remove all dyes not directly bound to the metal.

The Raman spectra with and without the proximity of the T-tip are shown in figure 2.10. A significantly stronger signal is observed when the tip is in tunneling contact with the substrate and the peak positions coincide well with those reported in the literature[142, 149, 150]. A bleaching behavior was not observed, probably because all of the experiment is preformed under high vacuum conditions[150].

With increasing distance, the signal decreases strongly in a nonlinear fashion. As show in figure 2.11, after less than 10 nm the peak intensity has decreased to $1/e'$ of the initial
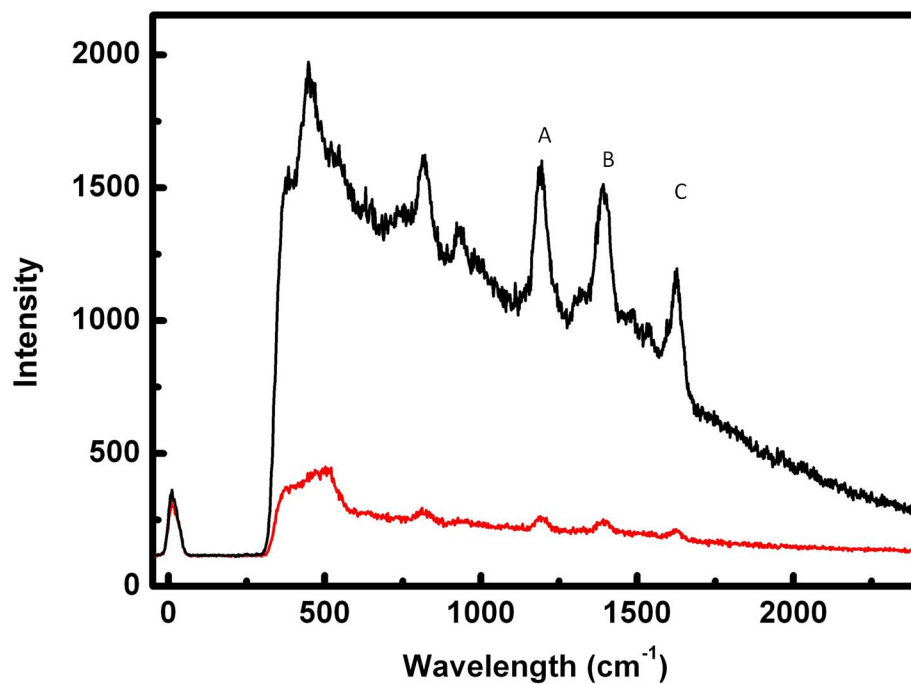
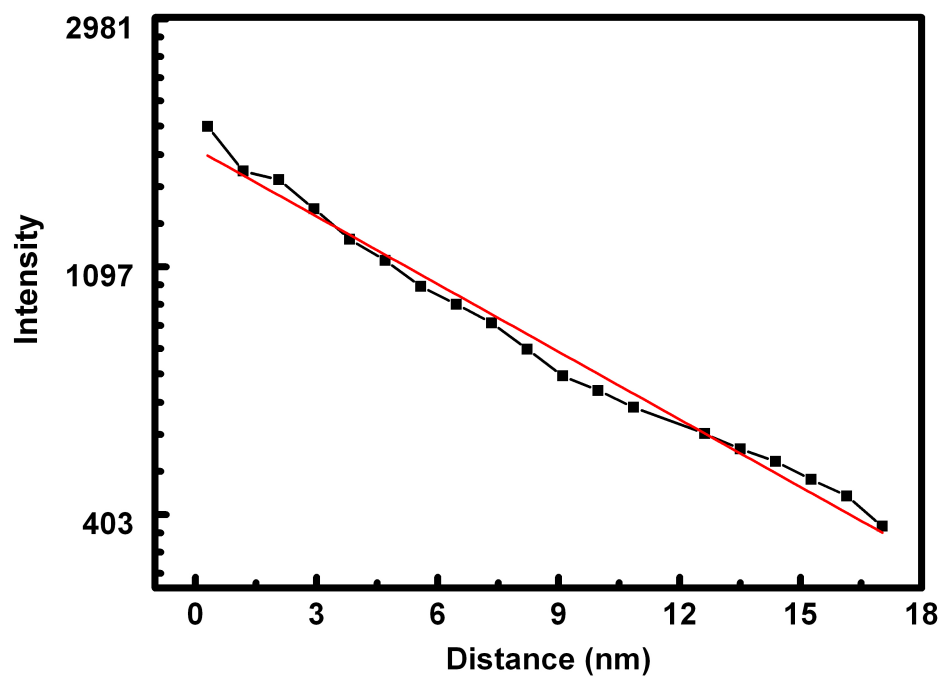FIGURE 2.10: Raman Spectroscopy of MGTIC. Integration time: 2 s. Laser power: ∼5 mW

FIGURE 2.11: Intensity of peak A in dependence to the tip substrate distance. Integration time: 2 s. Laser power: ∼5 mW

value. Thus, only a very small volume is exposed to the strong optical field at the apex of the tip. This translates to a lateral optical resolution of ~ 10 nm which is comparable to SNOM experiments performed with this tip. In previous work, the near-field intensity at the apex of the tip was found to be ~ 3.5 kW cm^{-2}, which corresponds to a tip enhancement of a significant field enhancement factor of 12.77 [148].

Chapter 3

Results and Discussion

In this chapter, the electron transport and the Raman spectra of single-molecule junctions are discussed in the context of the experimental and computational results for three different molecules (figure 3.1). We address the role of inelastic processes during electron transport and the switching behavior of current-driven single-molecule junctions.
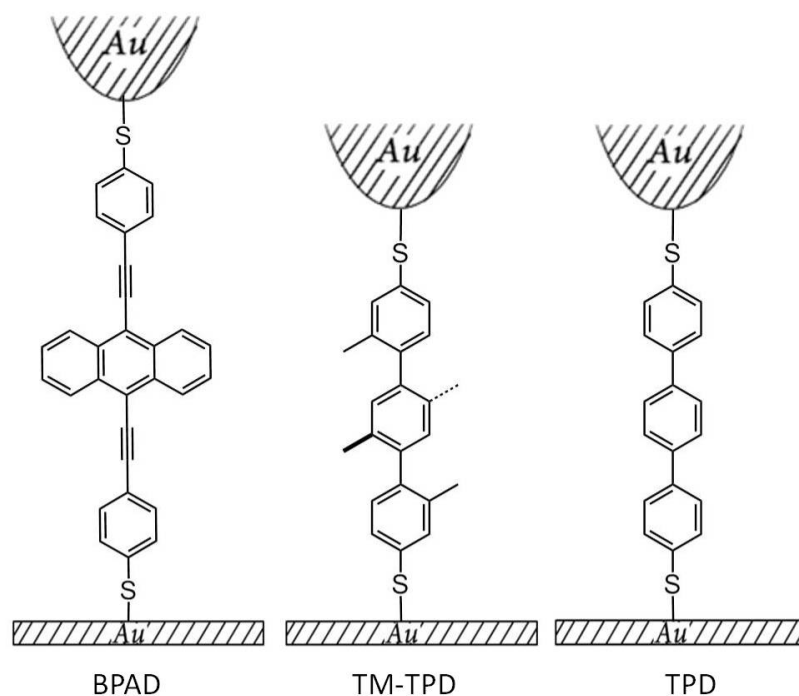
FIGURE 3.1: Schematic overview of the investigated systems: the rigid molecule **BPAD** ([9,10-Bis((2'-para-mercaptophenyl)-ethinyl)-anthracene]) and two similar molecules **TM-TPD** ([2,2',2",5'-tetramethyl-[1,1':4',1"-terphenyl]-4,4"-dithiol]) and **TPD** ([[1,1':4',1"-terphenyl]-4,4"-dithiol]) are covalently bonded to the gold covered T-tip and the gold substrate.

The conductance of single-molecule junctions is governed by the structure of the molecule in the gap and the information contained in a Raman spectrum is ideal to examine it.

44

Recent progress in single-molecule TERS detection have proven TERS to be an alternative method to study vibrational, rotational, and other low-frequency modes of molecules, which not only chemically identifies the molecules adsorbed on a surface, but, also yields information about adsorption configuration and chemical bonding in or between molecules. Current-driven phonon excitations of conjugated molecular junction are studied by the BPAD molecule. Raman spectra of single-molecule junctions of BPAD are examined at different applied voltages. Interesting effects are observed regarding both, the Stokes and the anti-Stokes Raman spectra. The positive charging of a current driving single molecule is demonstrated and a novel model for the phonon distribution caused by electron-phonon coupling is proposed. Furthermore, the switching behavior of a single-molecule junctions are discussed in detail with both, experimental and computational results. The physical origin is proven to be related to the positively charge status of the molecule.

3.1 Current-driven phonon excitations of a conjugated single-molecule junction
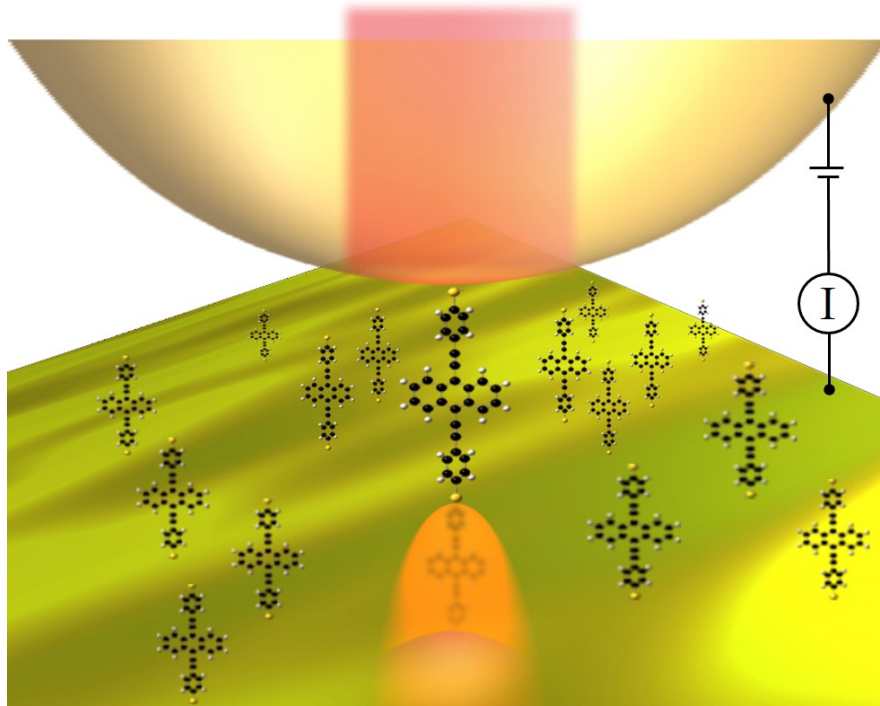
FIGURE 3.2: Molecule junction spectroscopy (MJS) set-up illustrating a single BPAD molecular junction to gold contacts.

Understanding transport and dissipation of charge through single molecules is fundamental for the development of (macro)molecular[1, 2] and quantum molecular circuitry. In metal-molecule-metal junctions[3, 4], where $\pi-$conjugated single-molecules show a conductance about 0.5 μS[40, 41], the control over electron-phonon coupling would make it possible to steer a wide range of dissipation effects from suppression[69] to optimization[5, 6]. In order to gain insight into electron-phonon mediated transport through molecules, articulated knowledge on non-equilibrium, nonadibatic quantum molecular energy landscapes must be attained. Because of this serious theoretical challenge, vast studies[7, 8] have been preformed focused on giving qualitative explanations for the current-induced vibronic progressions observed upon sequential low-temperature transport experiments[9, 10], as well as tunneling spectroscopy[11, 12] at the single molecular level. For sake of simplicity, these studies have used electron-phonon (λ_{el-ph}), electron-vibron and transport window-averaged electron-vibron coupling concepts interchangeably. In order to achieve exquisite control over electron-phonon coupling however, it is desired to understand the exact phonon excitations a single electron will trigger[68, 70].

In this section, the charge transport in single-molecule junctions are studied by its Raman spectroscopy. The experimental situation is sketched in figure 3.2. The molecule BPAD is covalently bound to the electrode, whereby the Raman spectra during conduction were recorded simultaneously. By employing a simple model, where a single low-lying vibrational state is excited by the electrons, an electron-phonon constant of λ_{e-ph} is extracted. Our measurements confirm a significant electron-phonon coupling in metal-molecule-metal junctions where low-lying vibrational modes at 300 K play the major role during current transport. The conjugated organic molecules were designed specifically for the single-molecule junction experiment, shown in figure 3.1. It consists of a rigid rodlike central section with additional thiol functions on both ends to form stable covalent bonds to the gold electrodes.

3.1.1 Electronic transport characteristics

In contrast to single-electron transistors based on metallic islands, molecular devices have a more complicated, but in principle, tunable electronic structure. Interesting and novel effects, such as negative differential conductance, were observed, and theoretical explanations are proposed in some of these experiments[40, 151, 152].
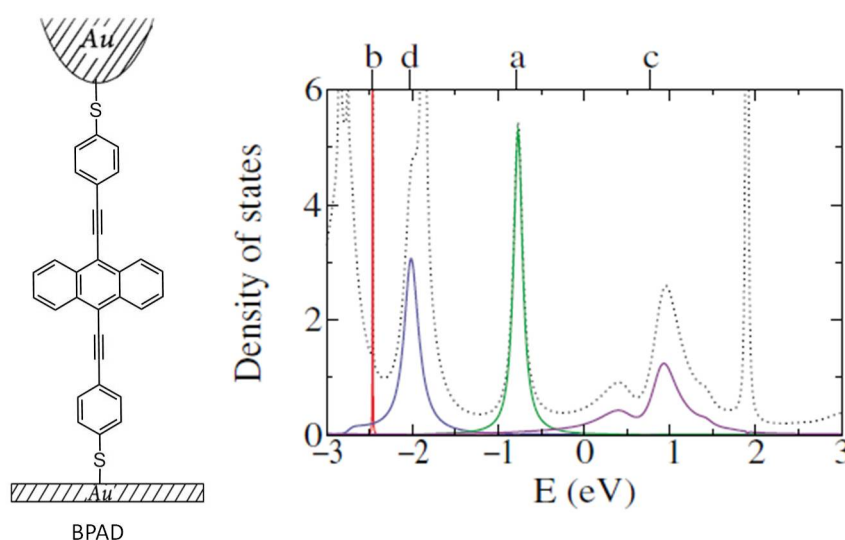
FIGURE 3.3: Schematic of the investigated system: The conjugated molecule BPAD and its total density of states of the molecule (dotted line) and the individual contributions of the four of the molecular orbitals (color lines). Adopted from [152].

The rod-like molecule BPAD has been used to in this field of molecular electronic for a long time due to its long range $\pi-$conjugated system. The electronic transport properties of it have already been experimentally investigated by J. Reichert *et al.* [40, 151] and theoretically studied by J. Heurich, F. Evers *et al.* [152] As shown in figure 3.3, the molecule is covalently bound to the gold electrodes. The calculated total density of

states of the molecule and the individual contributions of the molecular orbitals are illustrated by the coloured lines in figure 3.3. In their caculation, multiple molecular obitals, including HOMO, LUMO and two additional orbits, are able to contribute to the electron transport though the molecular junction.
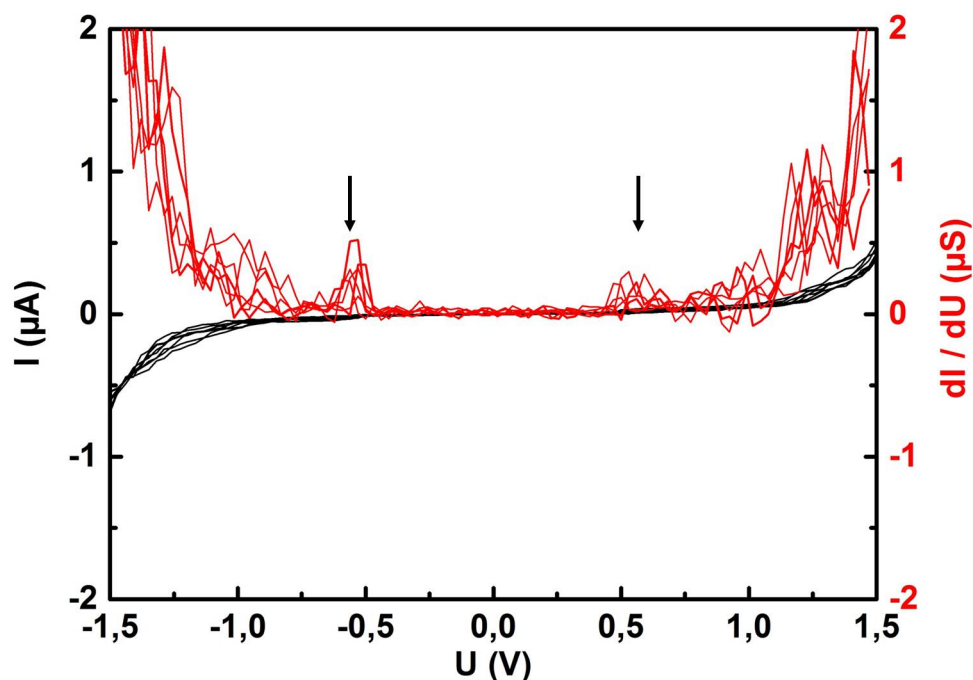

FIGURE 3.4: I-V characteristics of BPAD. The black curves represent the variation of current as a function of the applied voltage. The step-like features expressed as peaks in the differential conductance curves at approximately ±0.6 V are clearly visible in the red curves, as well as high lighted by the arrows.

Figure 3.4 shows current-voltage (I-V) curves of BPAD measured with our set-up. They are obtained in a stable tip-molecule-substrate junction. Its step-like features and the corresponding conductance peaks appear at approximately ±0.6 V. These resonances are assigned to elastic and inelastic processes and their pertinent interferences. In the molecular picture, adding or removing an electron to the molecule will cause the molecule to excite vibronic states. In the weak coupling regime, such excitations occur in the adiabatic Franck-Condon picture with a probability proportional to the overlap of the vibronic wavefunctions. It has been theoretically proposed that electron-phonon coupling can also be estimated from the phonon populations of the pertinent coupled modes during electron transport. This mechanism will be studied with Raman scattering of the same molecular junction in section 3.1.2.

To check the conductance of BPAD, the current distance curves were measured. The substrate, covered with a monolayer of BPAD, was carefully moved towards the tip.
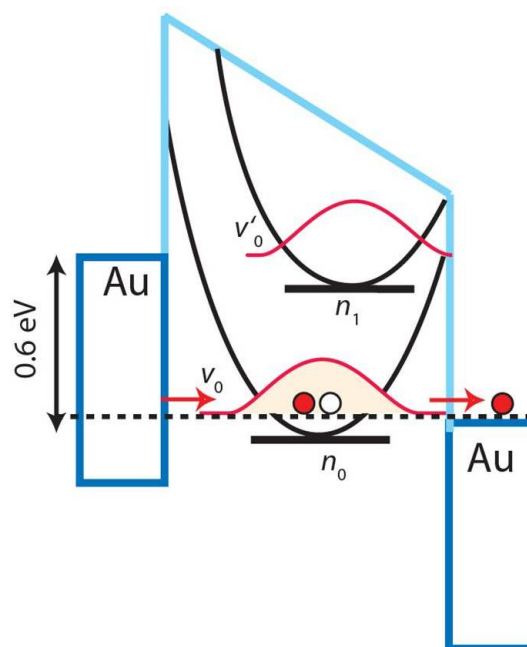
FIGURE 3.5: Schematics of charge transport in a molecule junction illustrating the case for one-quanta electron-phonon coupling to ν_1 during the conduction process through ν_0.
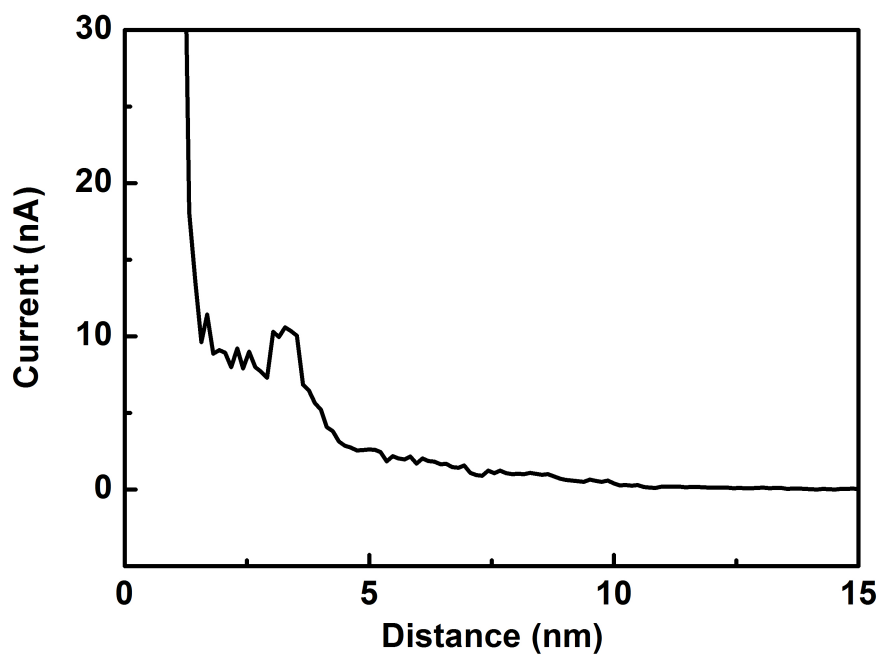

FIGURE 3.6: Current-height characteristics of BPAD. The tip approaches a submonolayer of BPAD from 15 nm down to a metallic contact to the substrate at $V_{bias} = 0.5\,V$.

With an applied voltage of 0.5 V, the current was recorded. As can be seen from figure 3.6, a considerable tunneling current is firstly recorded when the gap between the tip approaches the substrate. With the gap reaching 2.5 nm, the current rises up to 10 nA, indicating the formation of the bond between the tip and sulfur of the molecule. The observation of this "lock in" behavior suggests that a single molecule, but not a large ensemble, is bridging the electrodes.

3.1.2 Raman spectra of a current-driven molecular junction

When a stable single-molecule junction has formed, our home made set-up enable us to measure the Raman spectra of current-driven single-molecule junctions. For the purpose of studying the electron-phonon coupling process during electron transport of BPAD, we monitored the phonon population by vibrational spectroscopy in the bias voltage range of 0 V to ± 1.2 V. By comparing the Stokes Raman spectra of the single-molecule junction at different applied voltages, we could deduce the charge status of the junction during transport. By analysing the anti-stokes Raman spectra, the phonon distribution of the current-driven junction and the electron-phonon coupling factor λ could be evaluated.

Stokes Raman spectra

Figure 3.7 shows Stokes Raman spectra in the bias voltage range of 0 to 1.2 V, and reveal no change in the stokes spectra intensities at biases between 0 and ± 0.6 V. At and beyond 0.6 V, remarkable changes, including peak intensity losses and the appearance of new peaks, could be found. Firstly, a noticeable peak enhancement, two times higher than the initial peak, is found at 1060 cm^{-1}. Secondly, a new peak at 1375 cm^{-1} appears in the Stokes Raman spectrum. Finally, comparing the peak intensity at 2160 cm^{-1} with the other peaks, one can easily notice that the peak intensity at 2160 cm^{-1} decreases slightly. In the following discussion, we will compare these differences with computational results. A detailed discussion about the corresponding modes of these peaks is presented in section 3.1.4.

The DFT calculations in this study were carried out with the $GAUSSIAN$ 09W software package. First, the geometry of the molecular models is optimized. After that, the optimized coordinates are extracted to set-up an input file for calculation of vibrational frequencies. In all cases, the DFT methods calculate ground state properties in gas phase (without the electrodes), neither current or electric field are taken into account. The hydrogen atoms at both ends of the molecular models are constrained in order to simulate the rigid bond situation between thiolate group and gold electrodes The calculated Raman spectrum is compared with the experimental spectrum, and the vibration modes and the molecular orbitals (MOs) are studied.

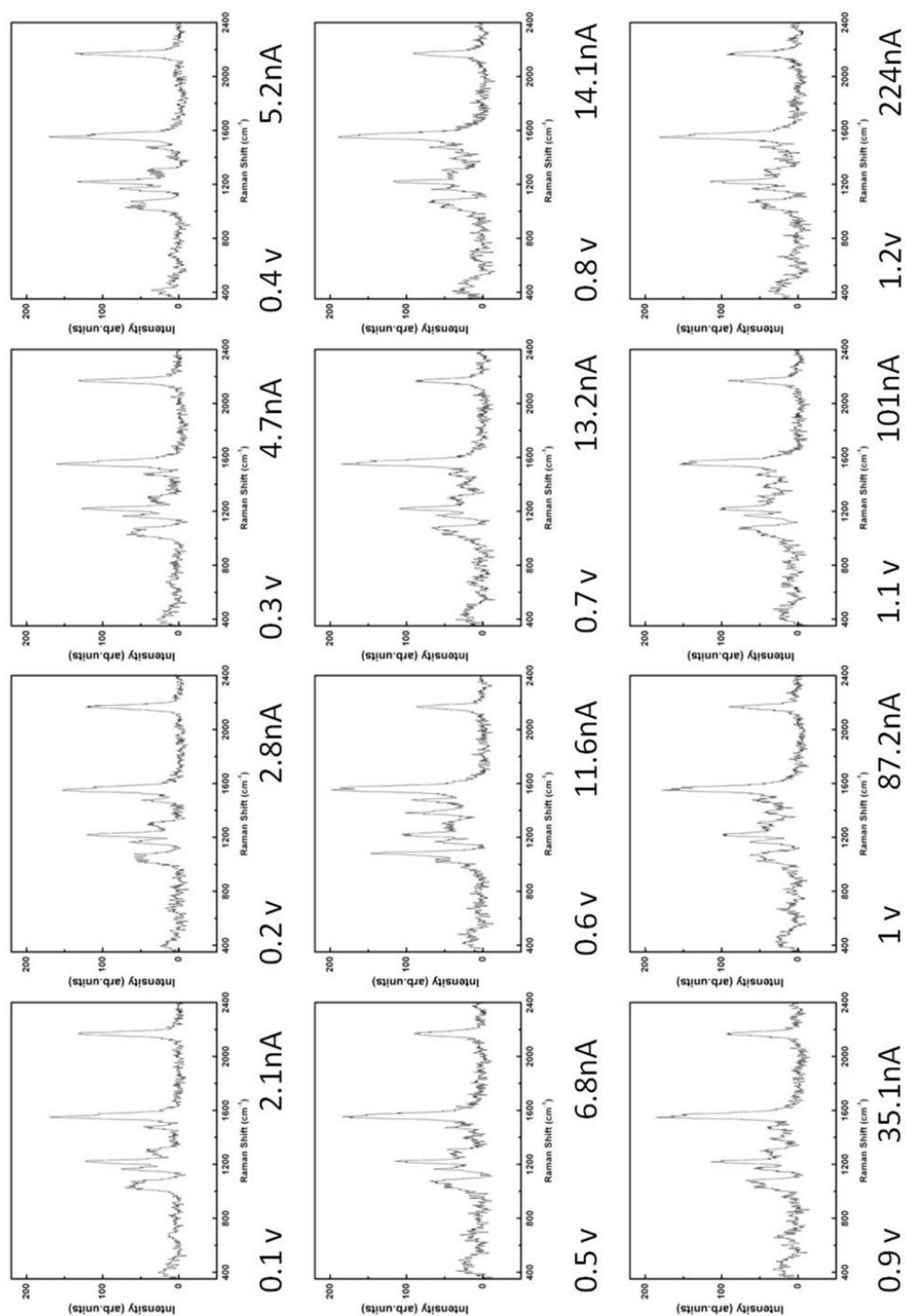FIGURE 3.7: Stokes shift of BPAD at different applied voltages (0.1 to 1.2 V). Exposure time: 5 s.

The experimental spectra of the single molecuar junction are compared with the calculated data of neutral, cationic and anionic species. In figure 3.8, the experimental spectra at 0 V a) and 0.6 V b) are plotted in the same intensity scale and the computational spectra of neutral c), cationic d) and anionic e) models are displayed below in arbitrary units at the same scale. The positions of the major peaks of the calculation results of the neutral, cationic and anionic molecules are nearly the same. Between the neutral and the anionic modes, one can easily find the differences. The triple peaks at around 1600 cm^{-1} shown in neutral species, has turned into two separated peaks for the anionic species. The relative intensity of the peak at around 850 cm^{-1} shows a remarkable enhancement for the anionic species by contrast to the other two. The peak positions and the relative peak intensities do not change too much between the neutral and cationic molecule except for a new peak, marked as c, and the decreasement of the peak, named as g.

When comparing the experimental data with the calculation results, one can easily determine that the spectrum at 0 V fits well to the calculated spectrum of the neutral molecule. Each peak on the experimental data could clearly attribute to the calculation data for both, on the peak position and the intensities. In other words, the observed Raman spectra also indicate that the single-molecule junction is well described by the gas phase molecule, used for the DFT calculations. By contrast, the Raman spectra of solid state materials often differ strongly from the calculated results. The spectrum at and above 0.6 V fits best to the calculated spectrum for the positively charged cationic molecule (and not to the neutral or negatively charged). At first, peak intensities of the calculated spectra show almost the same pattern in comparison to the experimental spectra, especially the peak highlighted by the dotted line at 1384 cm^{-1}. The same is true for the prominent peak at around 2200 cm^{-1}, whose intensity decreases in the cationic case d) compared to the neutral spectrum c). Second, the positions of the prominent peaks in the calculated spectra match well with those in the experimental spectra. The peak at $\sim$ 1600 cm^{-1} in spectrum b) consists of two overlapping peaks at 1591 cm^{-1} (peak e) and 1625 cm^{-1} (peak f) in spectrum d). The peaks in the computational cationic spectrum agree well with the experimental spectrum at 0.6 V, with an overall rms error of 35.6 cm^{-1} whereas the negatively charged spectrum e has a rms error of 69.2 cm^{-1}. These results strongly indicate that the molecule gets positively charged during the electron transfer process, showing hole transport through the highest occupied molecular orbital.

Anti-Stokes Raman spectra

When the applied voltage reaches ± 0.6 V, an anti-Stokes Raman spectrum is also detected. The observed peak positions match well with the Raman spectra on the Stokes
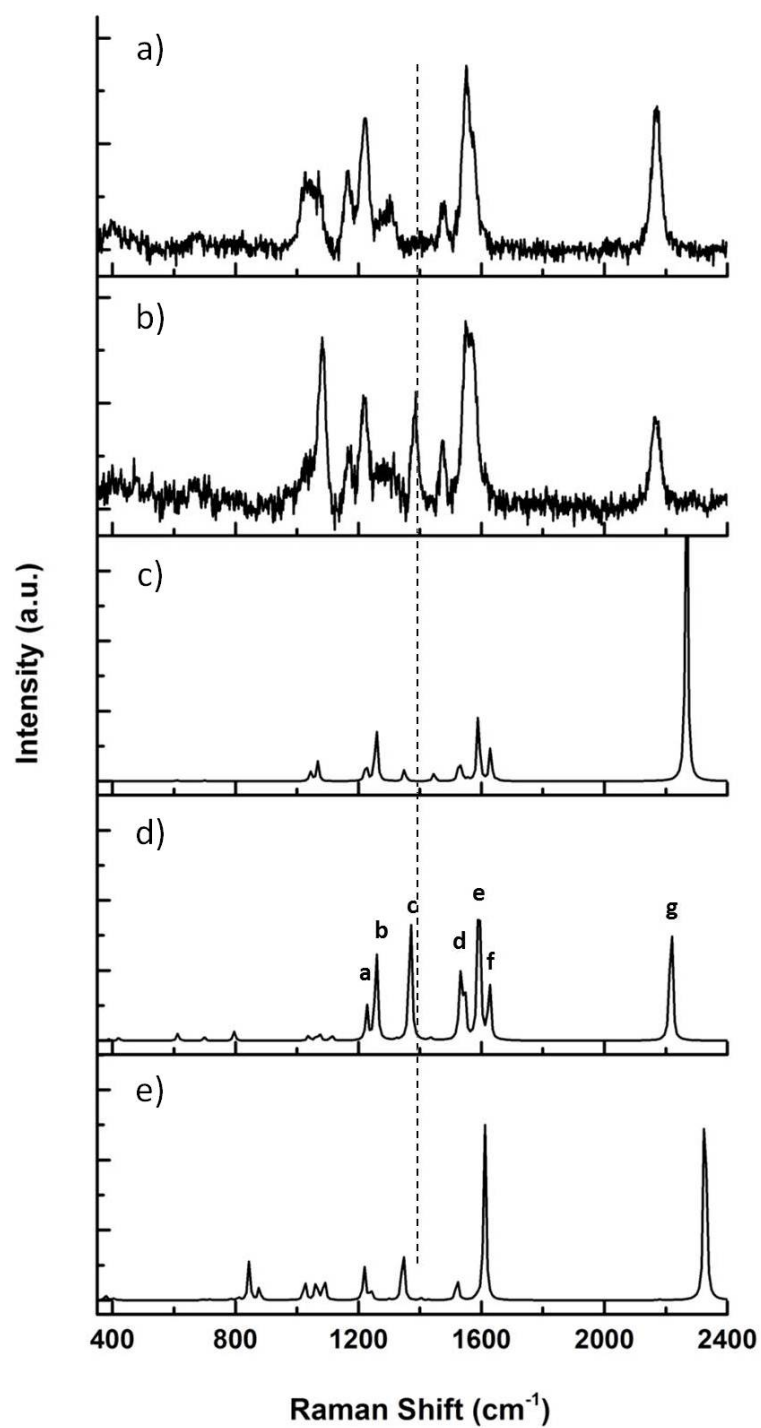
FIGURE 3.8: Computational and experimental Raman spectra of BPAD. a) experimental spectrum at 0.1 V; and b) experimental spectrum at 0.6 V; c) calculated spectrum of the neutral molecule, d) calculated spectrum of the cationic and e) calculated spectrum of the anionic species.

side. Two important features can be noted from the anti stokes spectrum. Firstly, the anti-stokes signal is detected starting at 0.6 V and investigated to remain constant up to 1.0 V. Note that measurements at higher biases were not possible due to junction instabilities. A higher voltage will lead to a unstable coupling between the molecule and the lead. Secondly, the anti-stokes spectrum follows a clear decreasing envelope of the Raman active modes (figure 3.9 the calculated spectrum is also sketched in red). The anti-stokes spectrum's envelope can be fitted to an exponential decay. This points out to the anti-stokes spectra being a distribution rather than a discrete spectrum obeying the Raman selection rules' intensities. Consequentely, the data suggests that each v_{th} anti stokes Raman active mode is weighted only according to the occupations of the $v \pm 1, v \pm 2, \ldots, v \pm n$ modes. This indicates that the Raman anti-Stokes spectrum represents a steady-state phonon distribution. In this picture, electron-phonon coupling populates low-energy phonon states whereas intramolecular relaxation and heat transfer to the metal leads depopulates the excited phonons.

3.1.3 Electron-phonon coupling factor

The analysis of the Stokes Raman spectra at different applied voltage have proven the molecule to get positively charged during the electron transport process. At the same time, an enhancement of the anti-Stokes Raman spectra is detected corresponding to the positively charged species. During electron transport through the molecule, the passing electrons can directly trigger off vibrations in the molecule. As a result, the phonon distribution increases remarkably. The exponential decay of the anti-stokes Raman spectra suggests a steady state phonon distribution on the molecule.

In this section, we will discuss the phonon population excited by electron transport in the junction. Figure 3.10 explains the origin for the exponential decay of the anti-Stokes Raman spectra. The equilibrium excited state of the molecule is sketched in figure 3.10 a). During electron transport, the low-lying vibration ν_0 is first excited and the phonon distribution reaches a non-equilibrium, as illustrated in figure 3.10 b). Simultaneously, the energy of this mode will relax to the neighboring mode ν_1 and to the electrode, and further to the mode ν_2, ν_3, ..., and ν_N. The final state is shown in figure 3.10 c). The intensities of the final distribution shows a clear exponential envelope. Restricted by the beamsplitter, the anti-Stokes Raman spectrum is cutted at around -600 cm^{-1}, which is definitely not the first excited mode. With the help of 50 : 50 beamsplitter, another peak at around 450 cm^{-1} could be observed, shown in figure 3.12.
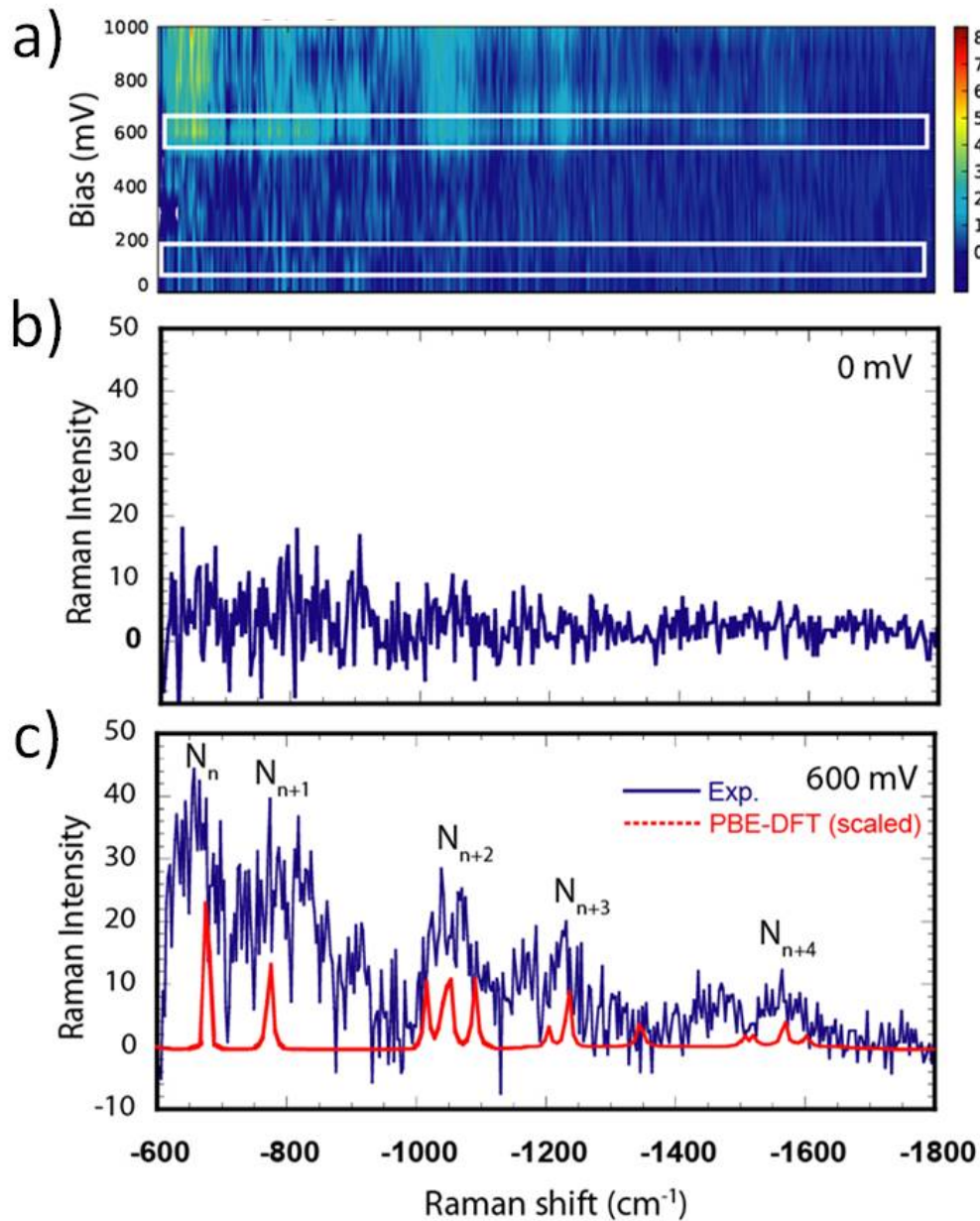
FIGURE 3.9: Anti-Stokes Raman spetra of BPAD at different applied voltage. The intensities of the peaks exhibit an exponentially decreasing tendency. a) Energy gain spectrum of the anti-Stokes Raman spectra at different applied voltage. b) anti-Stokes Raman spectrum at 0 V. c) anti stokes Raman spectrum at 1 V.

Consequently, a rate model can be exploited to fit the phonon population, excited by electrons in the junction. The task is vastly simplified by assuming that the electron-phonon coupling acts exclusively on a low-lying vibration $\nu 0$. The population of $\nu 0$, is thus allowed to relax to the next higher energy modes with a rate γ_{ph} and to the to the metal bath with a rate γ_m. Only $\Delta\nu = \pm 1$ relaxation steps are allowed such that $N_{\nu 0}$ is additionally populated at a rate $\gamma_{ph} N_{\nu 1}$. Figure 3.11 illustrates such a phonon population increase due to adiabatic overlap and subsequent relaxation. The population
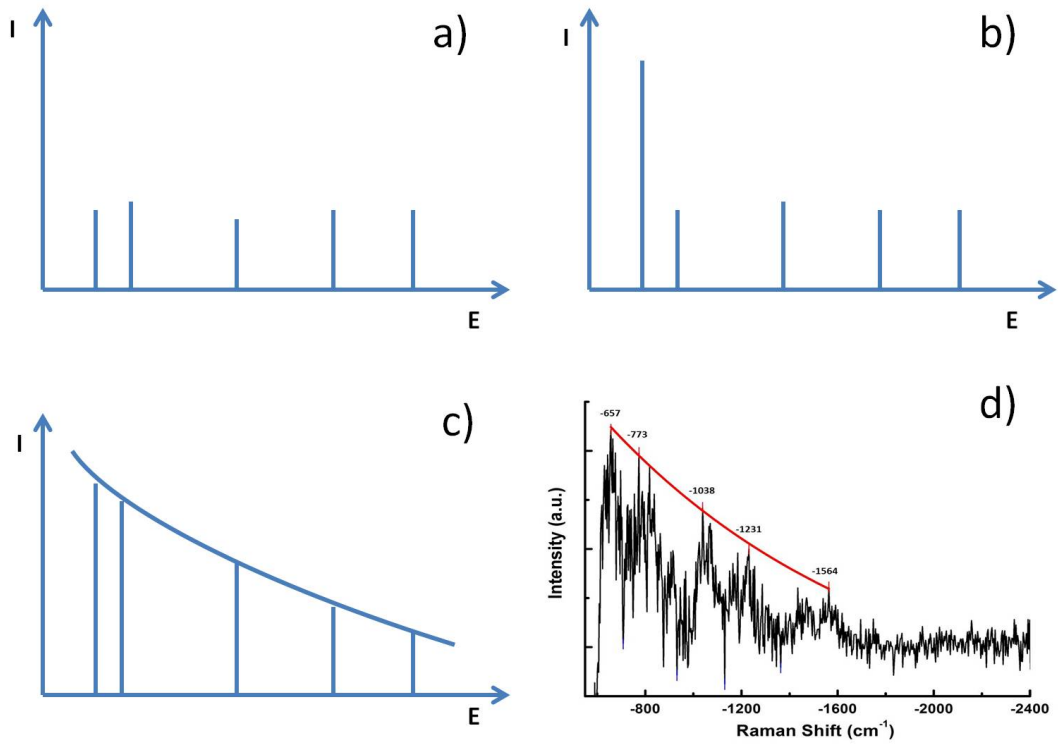
FIGURE 3.10: Model for the relaxation process. a)Equilibrium state for the modes of the molecue, b) Non-Equilibrium state after electron-phonon coupling, c) Final state after the relaxation. d) Exponiential fit of the anti-Stokes Raman spectrum.

rate of state $\nu 0$ can be described with the rate equation:

$$\frac{dN_{\nu 0}}{t} = \lambda I - \gamma_{ph} N_{\nu 0} - \gamma_m N_{\nu 0} + \gamma_{ph} N_{\nu 1} \tag{3.1}$$

and each following mode by:

$$\frac{dN_{\nu n}}{t} = \gamma_{ph} N_{\nu n-1} - \gamma_{ph} N_{\nu n} - \gamma_m N_{\nu n} + \gamma_{ph} N_{\nu n+1} \tag{3.2}$$
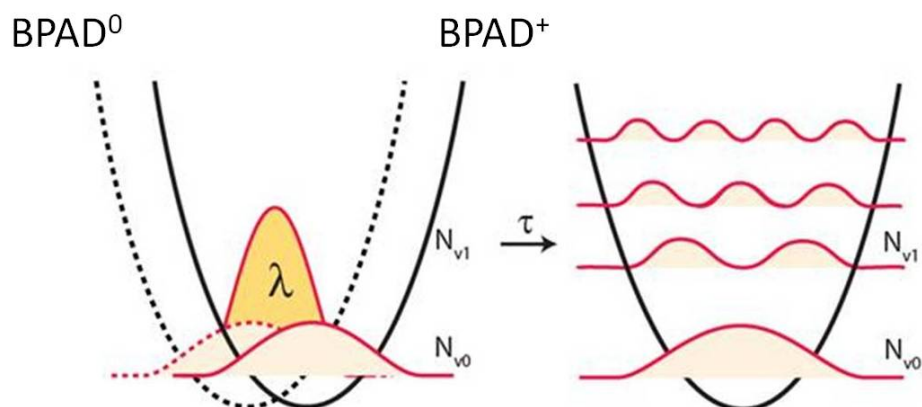
FIGURE 3.11: Modeling the electron phonon distribution. Electron-phonon coupling in the Franck-Condon picture, coupling to a $\nu 1$ state occurs through overlap between neutral BPAD and charged BPAD$^+$ adiabatic states followed by relaxion to higher energetic modes and the metal electrodes with a characteristic time τ.
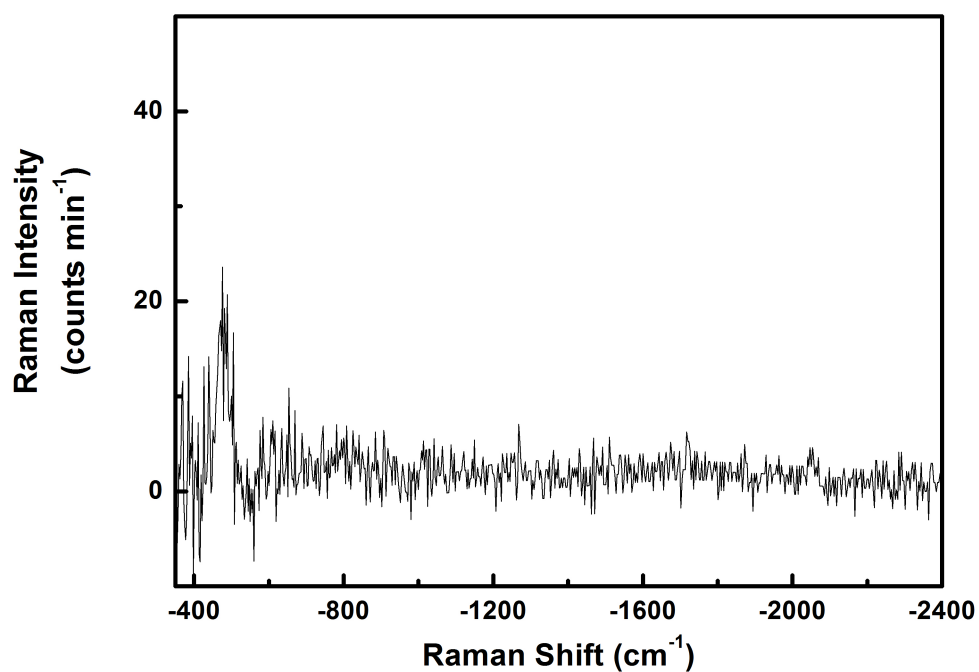
FIGURE 3.12: Anti-Stokes Raman spectrum of BPAD with $50 : 50$ beamsplitter

3.1.4 Vibrational modes of the observed peaks
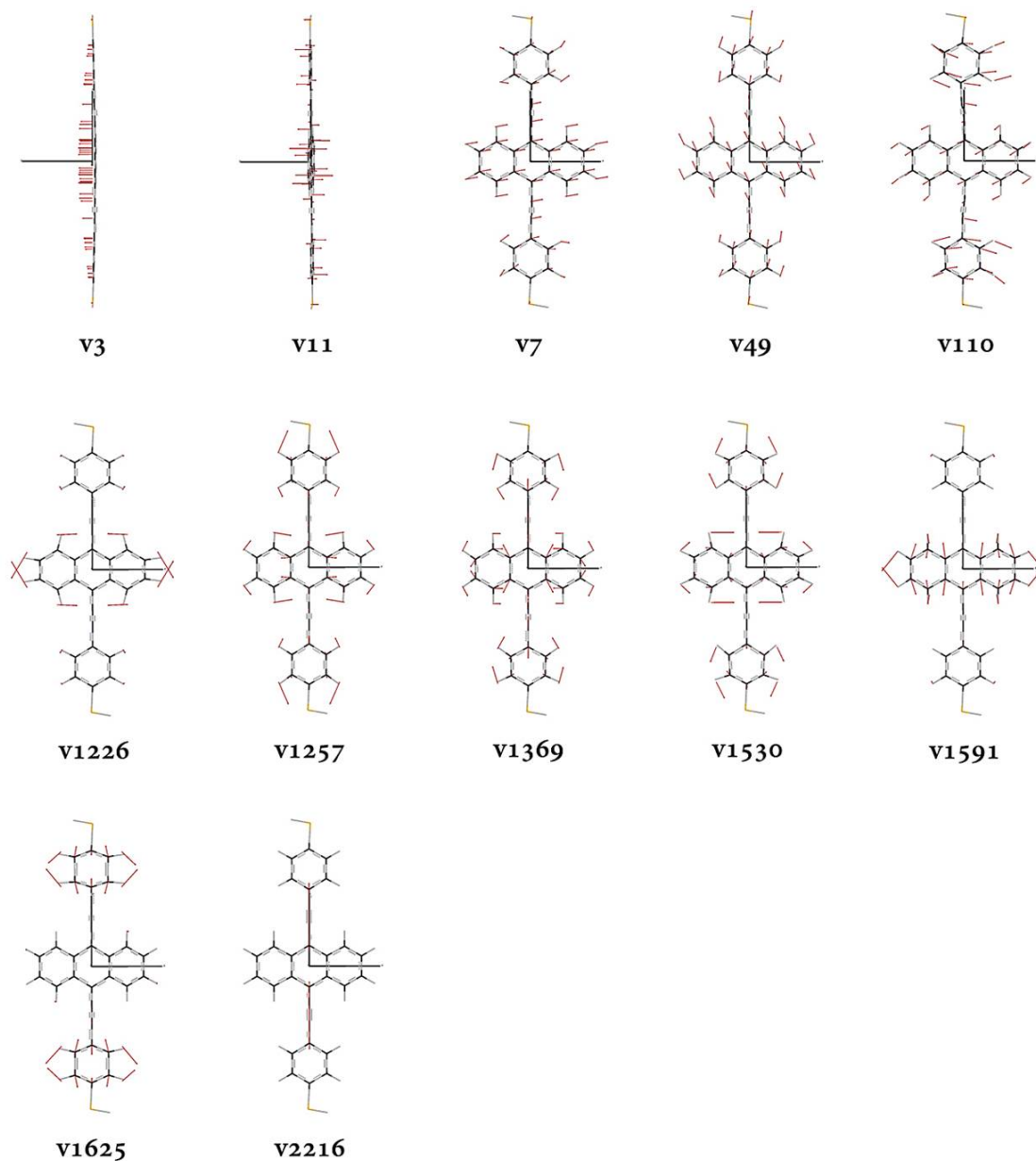
FIGURE 3.13: Vibrational modes of the cationic molecule. The modes are labeled with the corresponding frequencies which are given in cm^{-1}. The modes $v1226$, $v1257$, $v1369$, $v1530$, $v1591$, $v1625$, $v2216$ correspond to the peaks a, b, c, d, e, f, g in figure 3.8 d).

The geometry of all molecular models have first been fully optimized in gas phase using DFT with a B3LYP functional. After optimization, the Raman frequencies were calculated for the same models with constrained hydrogens at the sulfurs. Figure 3.13 shows some low-energetic vibrational modes and the modes for the most prominent peaks (a-g) in the cationic spectrum (figure 3.8 d)). The modes are labeled as v for vibration and

their corresponding peak positions. The vibrational modes in the first row in figure 3.13 are the ones with the highest amplitude which is indicated by the length of the displacement vectors. *v3* and *v11* are out-of plane modes, and *v7*, *v49* and *v110* are in plane rocking modes of the center of gravity of the molecule which do not exist for the unrestricted molecular model. These low-energy modes could be of significant relevance for electron-phonon interaction induced by the electron flow through the molecule.

One has to remark here that changes in the Raman spectrum (intensity as well as energy) may not only be induced by changes in the polarizability due to changes in the charge state of the molecule but also by strain on the molecule within the junction. *v1226* and *v1530* (Figure 3.8 d)-a, d)-d) are $C - H$ scissoring and rocking modes, which hardly can be influenced by these mechanisms. Thus the corresponding peaks almost remain at the same energy for different voltages. The peaks at 1591 cm^{-1} and 1625 cm^{-1} (Figure 3.8 d)-e, d)-f) overlap in the experimental spectrum and can be assigned to the vibrational modes *v1591* and *v1625* from the DFT calculation. These modes are stretching modes of the anthracene group and the mercaptophenyl groups. *v1257* and *v1369* are 'breathing' modes of both the anthracene group and the mercaptophenyl groups. The mode *v2216* is the stretch mode of the $C \equiv C$ bonds.

3.1.5   Temperature-controlled experiment

Notably, the ratio between the Stokes and anti-Stokes Raman intensities is normally depending on the sample temperature. The anti-Stokes side is here too small to be detected at zero bias. In our studies, the anti-Stokes spectra of the single-molecule junction are not observed at low voltage due to its low intensity. In order to distinguish between a steady state phonon distribution excited by a current and thermal junction heating, we increased the temperature of the environment. With the help of the MJS set-up, the temperature of the tip and electrode can be controlled and stabilized at a certain temperature. A series of Stokes Raman spectra of BPAD at elevated temperatures from 300 to 380K were recorded and are shown in figure 3.14. The obtained spectra show that BPAD is decomposing when increasing the temperature. Figure 3.14 b), c) and d) shows the decomposing tendency of the Raman activity of the molecule. The peak intensity gets weaker, the peak becomes broader and the peak positions are shifted. As shown in figure 3.15, the anti-Stokes Raman spectrum of BPAD is not observed even when the temperature reaches 380 K. The population of vibrations is not high enough to be detected before the molecule decomposes.
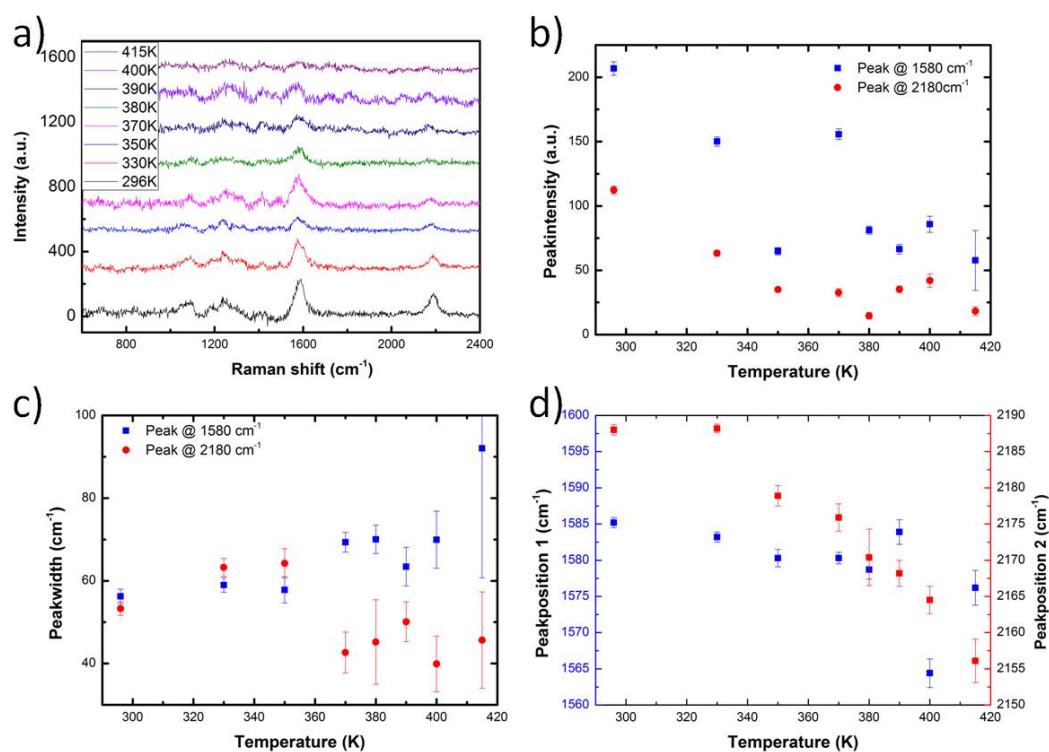
FIGURE 3.14: a) Raman spectra of BPAD at different temperature from 300 to 380 K. b) Peak intensities at different temperature. c) Peak width at different temperature. d) Peak position at different temperature.
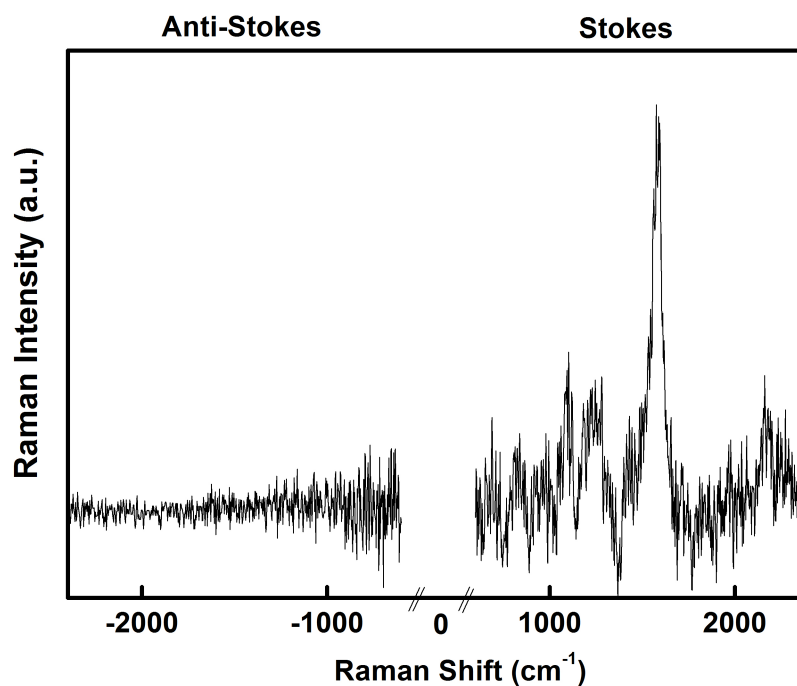

FIGURE 3.15: Raman spectrum of BPAD at 380 K

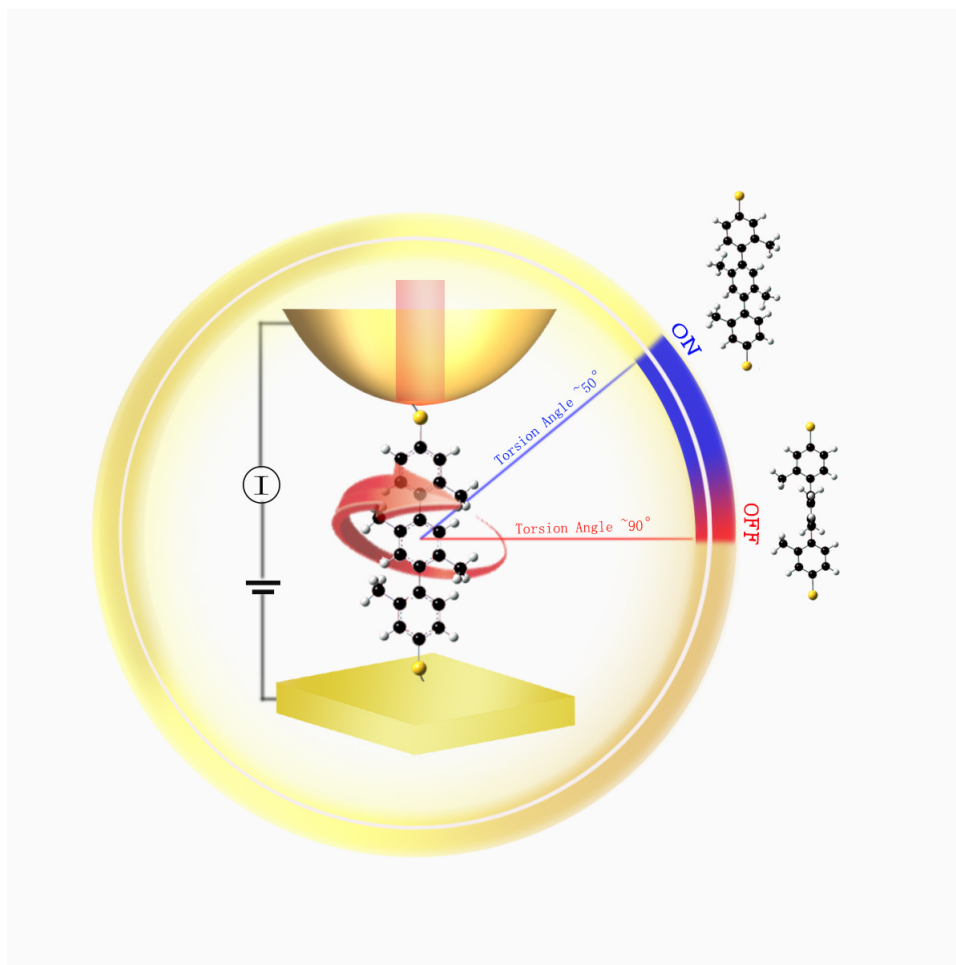## 3.2 Voltage-driven conformational switching in a single-molecule junction

FIGURE 3.16: Schematics showing conformational switching in a tip-molecule-substrate junction with Raman read-out.

Performing logic operations with molecules is regarded to as the next frontier in computation. Many strategies have been proposed towards this goal[153] based on bi- or multi-stable switching. Traditional engineering methods towards molecular switching have been trying to mimic contemporary semiconductor technology and implement charge state gating with single molecules[154, 155], macromolecules[156], or in organic thin-film transistors[157]. More elegant approaches rely on chemical[158–161] or conformational switching[162–166]. These studies often make use of photoisomerization in azobenzenes, diarylethenes or helical alkenes. Hybrid strategies have also exploited old and new, using gating and light[167, 168] in transistor devices. Light allows for detection of small changes in molecular conformations of quantum mechanical origin[162, 169, 170], exceeding outdated technology in terms of speed[167, 168] and power efficiency (by exploiting minimal electron-induced structural reorganization[171]). Moreover, recent work has

demonstrated the potential of single-molecules acting as logic elements[172]. However, while light stands as a versatile method for read-out during multi-logical operations, it adds additional challenges for the miniaturization of logics beyond current technology. In the order of single-molecules, molecular-scale computing to become reality, both switching and read-out must be demonstrated with single-molecule resolution.

In this section, we report on single molecule voltage-driven switching and single molecule read-out with Raman spectroscopy in self-assembled monolayers of substituted oligophenyls. By exploiting Raman selection rules through physico-chemical design, we show how Raman intensity can be turned "on" and "off" by nearly two orders of magnitude. Specifically, we use $p - terphenyl - 4, 4'' - dithiol(TPD)$, shown in figure 3.17 and remove its ground state polarizability by breaking planar $\pi-$conjugation, employing the tetramethylated (TM-TPD) analogue. In such highly hindered, non-planar TM-TPD, the Raman signature is turned off. By voltage-driven electronic transport via the highest occupied molecular orbital (HOMO), $\pi-$conjugation, and thus, polarizability and Raman response is recovered. Here, we introduces molecular switching and read-out at the 1 nm scale and, with the potential for ultrafast and minimum power dissipation computing.
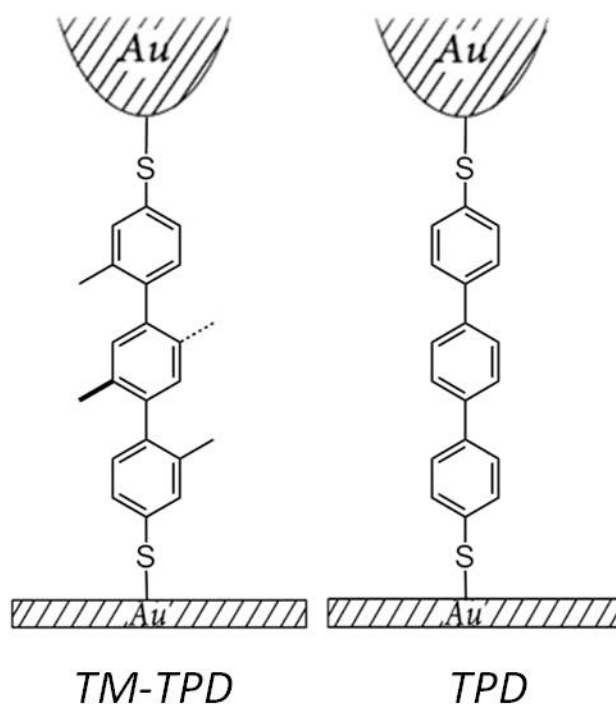

FIGURE 3.17: Molecular structure of TM-TPD and TPD

3.2.1 Electronic transport characteristics

In the studies of single-molecule junctions, numbers of experiments have shown the potential that current voltage characteristics of specific molecules can be switched in a controlled manner between "on" and "off" state by applying a pulse in a bias voltage. The physical origin of bistability in these experiments has also been intensely discussed in the past few years. He *et al.* attribute it in their experiment in an electrochemical environment to a change in the oxidation state of the molecule[64]. A polaron-caused bistability was also put forward by Galperin *et al.*[65] as a possible explanation for switching observed in a break-junction experiment. On the other hand, Keane *et al.* argue that the formation of a polaron is not a likely occurrence in their electromigrated gaps[61, 62]. They suspect rather that a bias-driven modification of the contacts may be responsible. Velimir Meded *et al.* give a more detailed discussion about the physical origin of the switching behavior[63]. Both, possibility of charging and conformational changes are discussed. Indeed, a convincing experimental description together with the theoretical explanation is needed to explain the observed switching behavior.

The rigid rod-like molecules, TPD and TM−TPD have been designed to perform systematic studies on the effect of the degree of π−conjugation of the molecule on charge
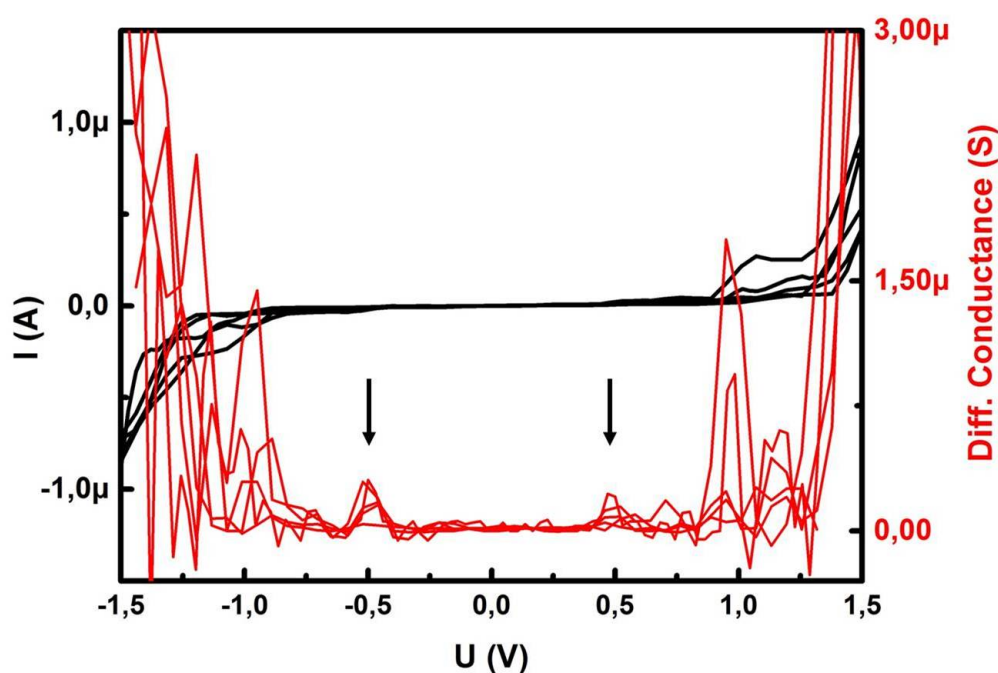

FIGURE 3.18: Electronic transport characteristics of TPD. One can see broad step-like features present at about ±0.5 V in the current-voltage curves, which correspond to conductance peaks in the differential conductance curves.
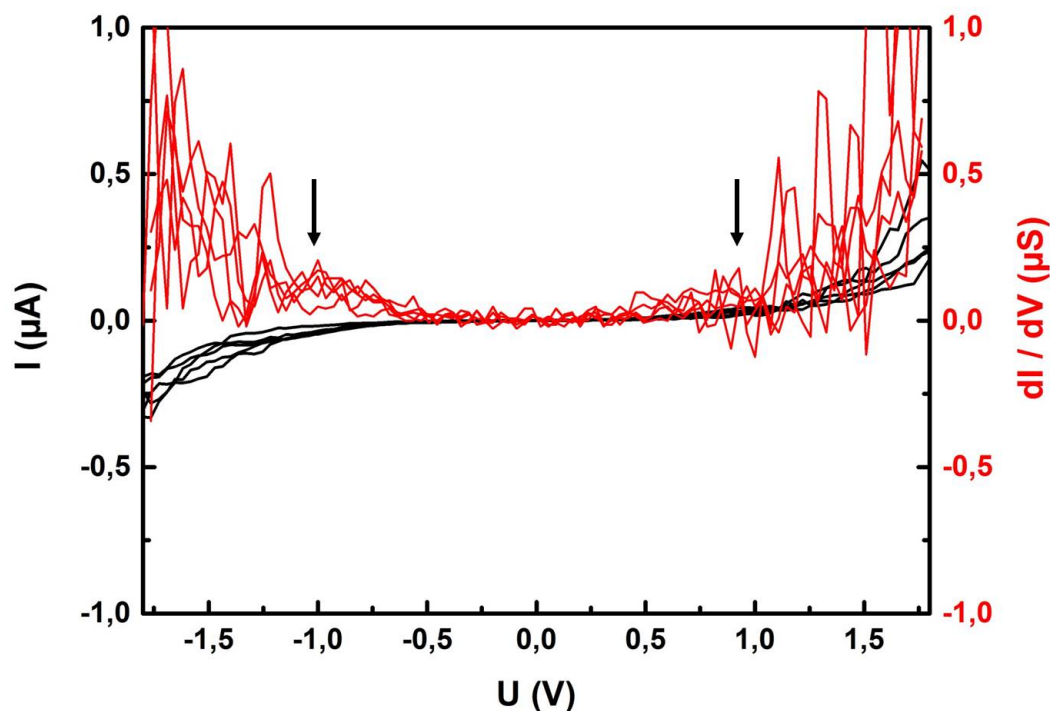
FIGURE 3.19: Electronic transport characteristics of TM−TPD. One can see broad step-like features present at about ±1.0 V in the current-voltage curves which correspond to conductance peaks in the differential conducting curves.

transport. For that reason, methyl groups of TM-TPD are attached to the phenyl rings at the ortho position to induce steric strain, resulting in the rotation of phenyl rings with respect to each other. Therefore, π−conjugation between the phenyl rings along the molecule is expected to be reduced rather than being strongly interrupted.

Figure 3.18 and figure 3.19, show typical IVs for TPD and its methylated analogue TM-TPD. Remarkable differences between the two molecules could be found. The single-molecule junction of TPD shows a conductance, which is at least two times higher than TM-TPD. At the same time, the steplike features in the I/V characteristic of TPD is typically easier to be distinguished when the applied voltage reaches ±0.5 V. Relating to a molecular orbital being in resonance with one of the electrodes electrochemical potential, enabling electron transport. For TM-TPD, this step-like feature is not so emphasized, but still observable in the windows of ±(0.8 to 1.3) V in its dI/dV curves. The lower conductance of TM-TPD indicates, that charge transport is highly suppressed. Notably, TPD achieves a conducting state at lower voltages than the TM-TPD. This is mainly attributed to an internal interruption of the π−system.

Figure 3.20 shows a typical dark current versus distance profile at $V_{bias} = 0.5$ V, when the tip approaches a submonolayer of TM-TPD from 15 nm down to a metallic contact to
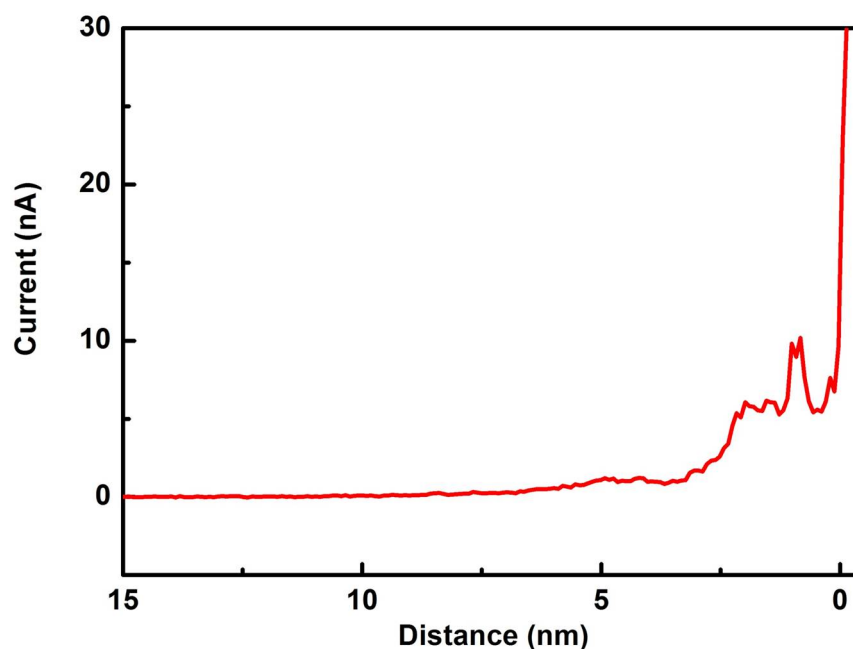
FIGURE 3.20: Current-distance profiles of TM−TPD. The tip approaches a submono-
layer of TM−TPD from 15 nm down to a metallic contact with the substrate at
$V_{bias} = 0.5$ V.

the substrate in an ultrahigh-vacuum environment at room temperature. We distinguish
two different conductance regimes. Between 10 and 2 nm, we detect a tunneling current
between the tip and the substrate. Below 2 nm, the current shows a steplike increase
up to 5 nA and stays stable for the tip approaching 0.5 nm. The tip is covalently bond
to molecule and shows a constant current. The small peak at around 1 nm could be
attributed to an additional molecule bond between the tip and the substrate. In this
regard, the observed data corresponds well to the estimated size of around 2 nm for the
molecule.

3.2.2 Raman spectrum controlled by applied voltage

Figure 3.21 a) and b) shows the experimental Raman signature of TPD molecule junction
at 0 and 1V. The Raman spectra stay same at different applied voltage. When increasing
the voltage up to ± 1.5 V, no significant change in the ~ 1600 cm^{-1} signal occurs.
What is more, both spectra of TPD show equal intensities for the D and L band at
1220 and 1280 cm^{-1}, which points towards the conjugation length not being altered.
Accordingly, we employed the sterically hindered TM-TPD derivative in order to remove
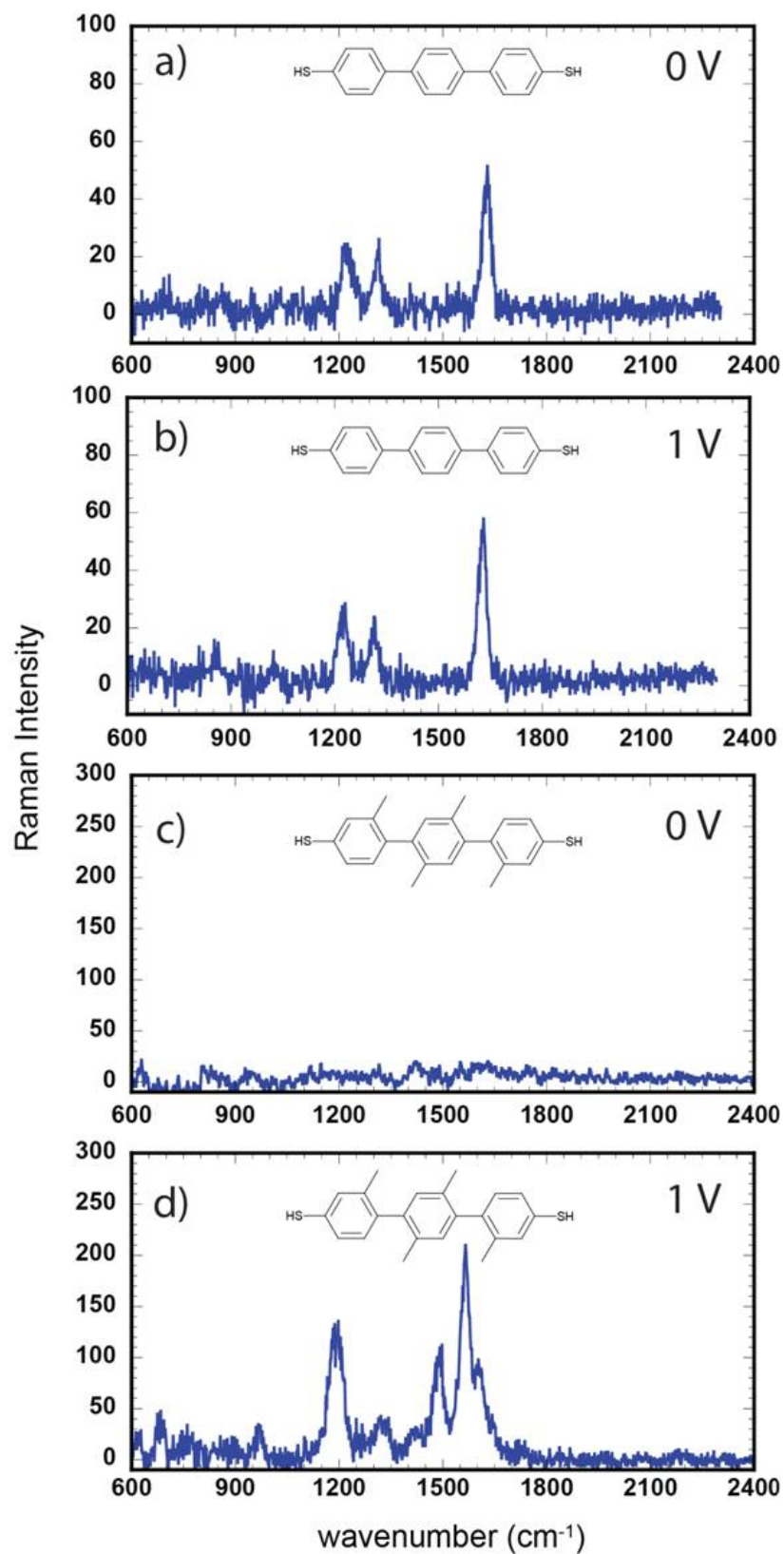any possible optical or temperature-induced inter-phenyl libration in the ground state,

FIGURE 3.21: Conformational switching in a single-oligophenyl monitored by Raman spectroscopy. Measured spectra of a) neutral (0 V bias) TPD b) charged (1 V bias) TPD$^+$ c) neutral (0 V bias) TM-TPD and d) charged (1 V bias) TM-TPD$^+$. Insets in correspond to chemical representations of the molecular structures.

thereby provoking a decrease in the $\sim$1600 cm^{-1} mode signal. Fig. 3.21 c) and d) depict the measured MJS Raman spectra of TM-TPD. This time, the Raman signal of the neutral state (at zero bias) decreases below instrumental detection limits, effectively switching off the optical junction. When the junction is biased to 1 V, in order to recover the TM-TPD$^+$ charged state through HOMO transport, the Raman signal is detected once again. In this respect, the Raman activity of TM-TPD highly dependent on the applied voltage, and the difference between TPD and TM-TPD offers the reason for this effect.

Unlike our previous Raman studies employing a phenylethynyl derivate, no anti-Stokes Raman signal was detected during HOMO charge transport for neither TPD$^+$ or TM-TPD$^+$. For a better understanding of the voltage driven molecular switching behavior, the computational analysis is discussed in section 3.2.3.

3.2.3 Computational analysis

With the MJS set-up, changes in the inter-phenyl torsion (IPT) angles can be resolved with single-molecule resolution, employing the Raman effect as optical read-out. The Raman spectrum can be tuned according to the selection rules for the different molecular conformational states. The Raman intensity is dictated by the internal product of the polarizability tensor with the overlap between initial and final phonon wavefunctions. Therefore, by both decreasing the mode's polarizability and/or making the product antisymmetric with respect to the pertinent molecular symmetries, a Raman signal can be decreased or even turned off. We thus investigated the modulation of the Raman spectrum due to the altered $\pi-$conjugation induced by charge transport. When an oligophenyl acquires quinoid character, the electron system becomes delocalized through the phenyl rings, hence increasing the states' polarizability. It is well known that the $\sim$ 1600 cm^{-1} Raman signature corresponding to phenyl-phenyl stretch mode is more intense in ladder-type parapolyphenylene than in pristine parapolyphenylenes. Therefore, it is expected that the Raman signature of TPD$^+$ is increased by HOMO charging, when $\pi-$conjugation character is dominant.

In fact, the calculated Raman intensities at the theoretical predicted geometrical stationary points of the neutral (IPT 34°) and charged (IPT 24°) TPD molecule in figure 3.22 a) and b) shows that the $\sim$ 1600 cm^{-1} mode's polarizability is twice as high for the latter. The polarizability is qualitatively assessed by taking the sum of the absolute values of the polarizability tensor elements (SAP). The neutral state's decrease in polarizability is accompanied by a 1.2 fold decrease in the Raman activity. The calculated intensities at the geometrical stationary points of the neutral and charged molecules in figure 3.22 a)
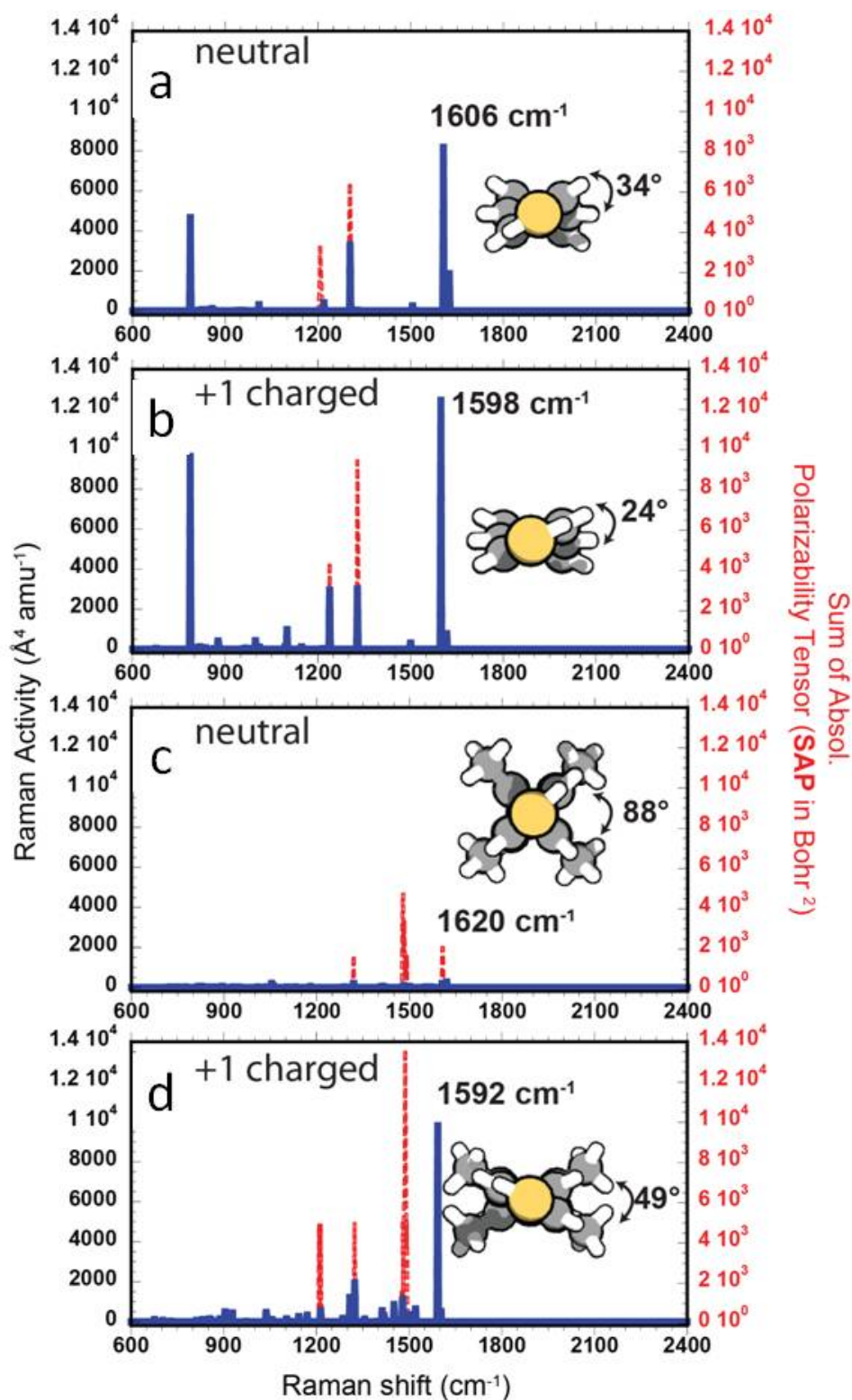
FIGURE 3.22: Caculational Raman spectra of TPD and TM-TPD. a) neutral TPD b) charged TPD$^+$ c) neutral TM-TPD and d) charged TM-TPD$^+$. Insets show the chemical representations of the molecular structures.

and b) show the reported dependence of the D/L ratio on the IPT. Both observations suggest that the $\pi-$conjugated character is also present in the neutral state configuration. This is since inter-phenyl librations of the neutral state configurations can be excited either thermally or optically during the measurement, thereby overcoming IPT barriers.

Figure 3.22 c) shows that the calculated geometrical stationary point for the neutral TM-TPD, which has now an IPT of 88°. Here, the calculated Raman activity falls below 1000 $A^4 amu^{-1}$. Interestingly, the charged state of the TM-TPD$^+$ features a geometrical stationary point with a reduced IPT angle of about 49° (figure 3.22 c). In this geometry, a fourfold increase of the SAP for the ~ 1600 cm^{-1} mode and more than a tenfold increase in the Raman activity when compared to the neutral state is observed. These observations indicate that polarizability is the major component behind Raman activity in $\pi-$conjugated systems.

Geometry optimization
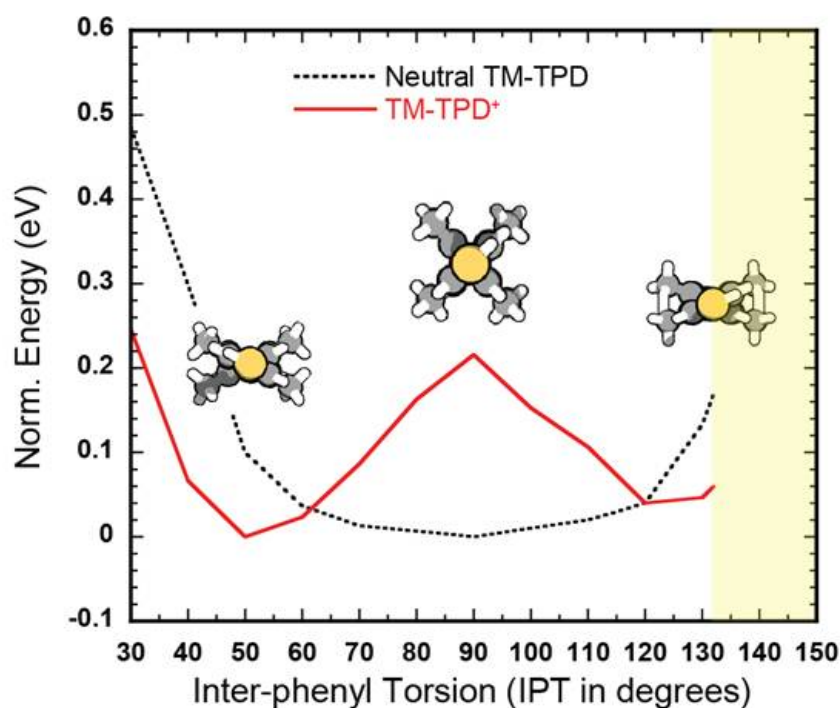
FIGURE 3.23: IPT energy landscape. a) Calculated adiabatic IPT vs. ground state energy where a barrier of 100 meV is observed for $\sim 20°$ libration around the geometrical stationary point of the charged TM-TPD$^+$. The area where methyl units of adjacent phenylenes overlap is indicated in yellow.

In order to investigate the energy landscape bias behind charge-induced $\pi-$conjugation, we studied the minimum energy in dependence of the IPTs in the TM-TPD$^+$ state.
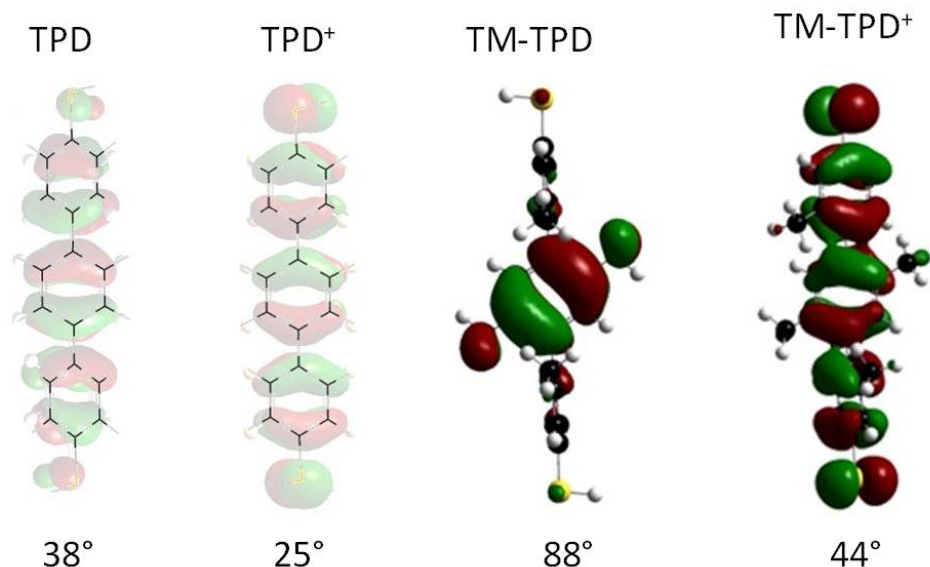
FIGURE 3.24: The optimized molecular structure and the charge density plot of TPD and TM-TPD. The torsion angle of the center phenyl ring in respect to the outer rings is labeled downside. TM-TPD$^+$ shows a clear $\pi-$conjugation through overlap of orbitals with equal parity.

Figure 3.23 depicts the dependence of the charged state minimum energy of different IPT angles. For each point, the structures were geometrically relaxed while keeping the IPT fixed. The results show that the barrier for libration between IPT angles of $35° > 49° > 75°$ is in the order of 100 meV. This is consistent with a polaron induced strong quinoid character upon charging. The much smaller angle of TM-TPD$^+$ for which quinoid character is recovered, indicates that $\pi-$twisted orbitals are formed. The $\pi-$twisted orbitals for TM-TPD$^+$ are depicted in figure 3.24.

A comparison of the optimized molecular structure of the neutral and cationic models of TPD and TM-TPD are shown in figure 3.24. For TPD, the torsion angle between the center and the outer phenyl groups of the neutral model is about 38° and for the cationic model about 25°. Both, the neutral and the cationic models show a good $\pi-$conjugation. Obviously differences can be observed for the TM-TPD. Almost no $\pi-$conjugation is observed due to the large IPT angles forced by the methyl groups. These results coincide well with the previous report that the TM-TPD possess a reduced conjugation between its $\pi-$conjugated subsystems[58].

Spectrum in dependence of the torsion angle

Additionally, calculations of the Raman spectrum of the neutral TM$-$TPD were preformed with different torsion angles (figure 3.25) of the tolyl groups to in order to understand the phenomena depicted in figure 3.21. Spectra a) to e) were calculated from fully optimized molecular structures with fixed hydrogens of the thiol-groups. From figure
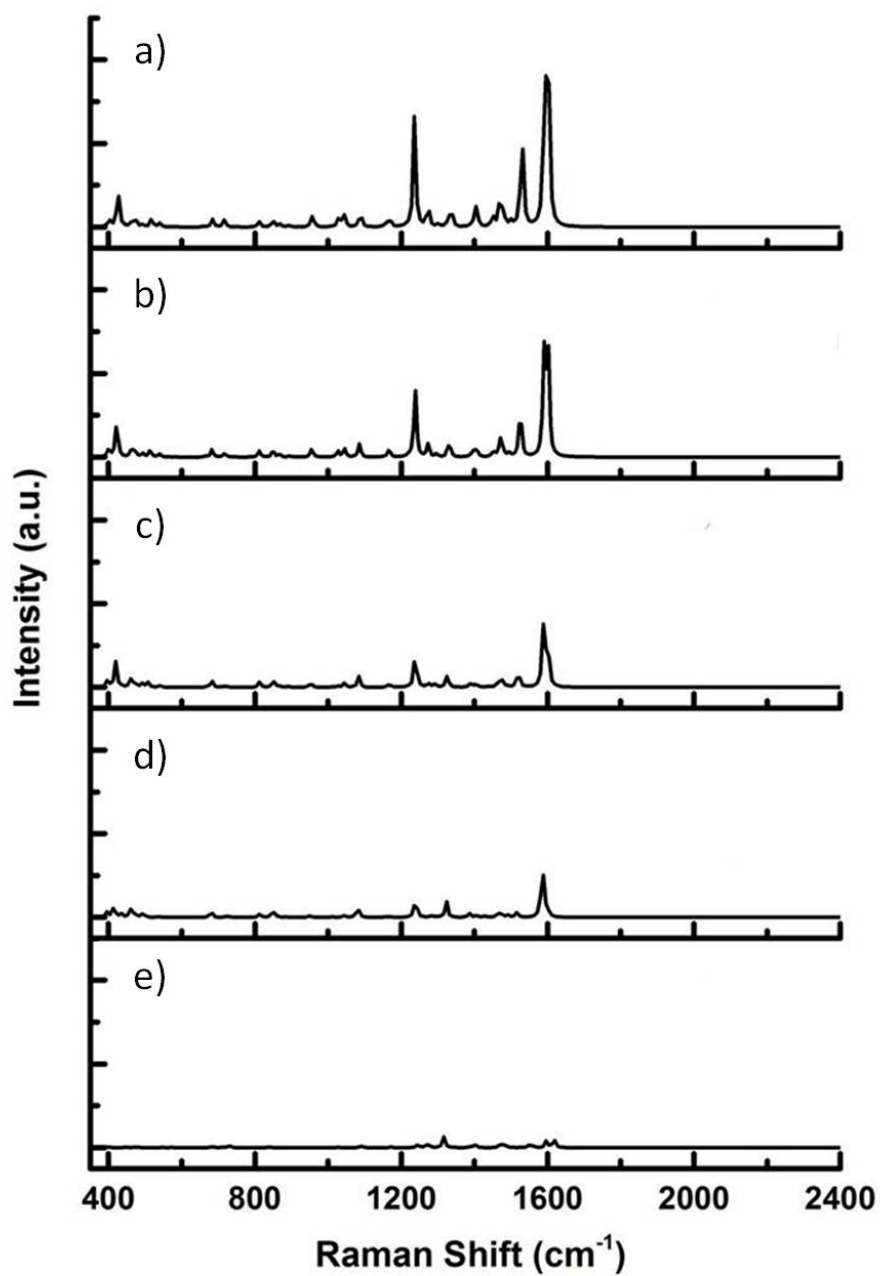
FIGURE 3.25: Computational Raman spectra for different torsion angles for cationic TM−TPD. Spectra (a), (b), (c), (d), (e) are calculated in different torsion angles separately 50°, 60°, 70°, 80° and 90° with corresponding molecular models.

3.25, we can extract that the Raman intensity of TM-TPD is highly dependent on the torsion angle of the tolyl groups. A better $\pi-$conjugation of the molecule will lead to a higher Raman intensity of the molecule. In other words, the better $\pi-$conjugation of the molecule will result in a better polarizability of the molecule. For the current driving single-molecule junction of TM-TPD, the applied voltage offers us a highly reproducable and reliable method to control the inter phenyl torsion angle. The positive charged state of TM-TPD will result in a strong $\pi-$conjugation. Finally leading to increasement of the Raman intensity. Surprisingly the positions of the peaks stay almost unchanged, when changing the torsion angles of the tolyl groups.

Traditional engineering methods towards molecular switching have been to mimic contemporary semiconductor technology and implement charge state gating with single molecules[18, 41, 165], macromolecules[155], or in organic thin-film transistors[163, 164]. More elegant approaches rely on chemical or conformational switching and combinations thereof[166, 167]. These studies often make use of photoisomerization in azobenzenes, diarylethenes or helical alkenes. Hybrid strategies have also exploited old and new, using gating and light in transistor devices.

Conformational switch

In our studies, we have achieved the minimum unit switch with the combination of the techniques of single-molecule junction and single-molecule Raman spectroscopy. The molecule Raman reponse of TM$-$TPD is turned *on* and *off* by the applied voltage. The measurement could start with an *on* state at 1 V. A strong the Raman signal could be observed in this state. When the applied voltage is set down to 0.1 V, the Raman signal of the single-molecule junction drops down below the detection limit. This process could be repeated several times until the molecular junction brakes.

Figure 3.26 shows a model of the conformational switch. First, the ground state geometry of the neutral and the cationic molecules exhibit different torsion angles. Furthermore, the Raman signal intensities decrease with the increase of the torsion angle, which is supposed to be caused by the polarizability change due to delocalization of the highest occupied molecular orbital (HOMO). The charge distribution of the HOMO changes from one, which is localized on the center ring to one which is equally spread across the whole molecule suggesting a transformation from the non-conduction molecular state to the conducting state.

In summary we could demonstrate conformational switching, controlled by the bias-voltage in a single-molecule junction. The investigations allowed us to experimentally identify $\pi-$conjugation as a strong dictating force of Raman activity. The possibility of addressing physico-chemical phenomena with molecular resolution performed here, may
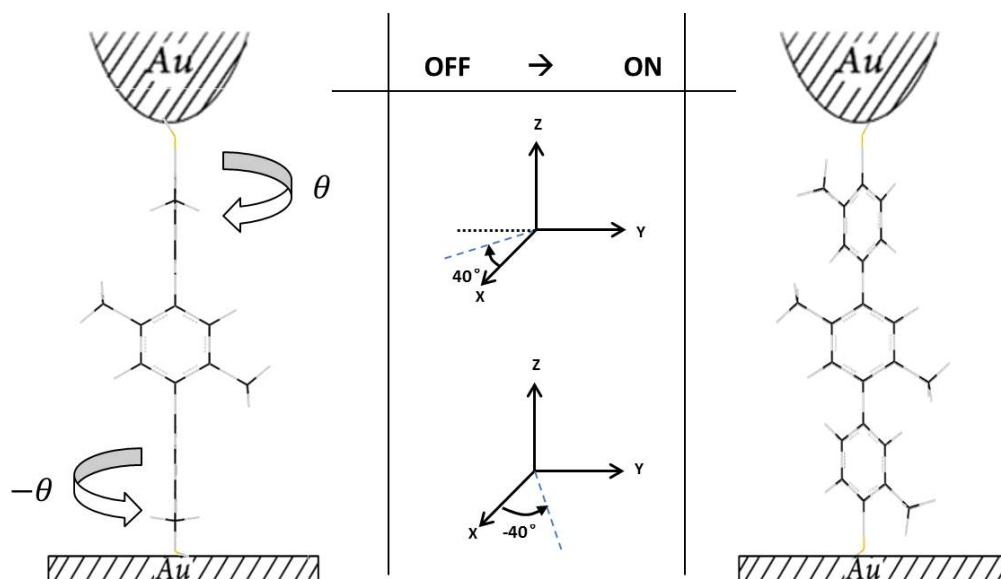
FIGURE 3.26: Schematic model of the conformational switch. The neutral molecule is presented on the left as the *off* state. The curved arrows indicates the rotation of the tolyl groups. In the middle, the rotational directions and angles are illustrated with cartesian coordinates. The cationic molecular junction is shown on the right as the *on* state.

serve as a departure point for a new generation of ultrafast and nanomechanical studies using the MJS technique. Technologically, our investigations present single molecular monitoring and manipulation. This opens up new avenues in multi-logic molecular computing.

Chapter 4

Summary

The role of inelastic processe during electron transport through single-molecule junctions as well as its influence on the electronic and conformational state have been investigated witch a novel MJS set-up by Raman spectroscopy in dependence of the voltage. A series of theoretical studies were also performed to interprete the experimental findings.

The observed Stokes−Raman spectra of the current-driven single-molecule junction with BPAD molecules match well with the calculated results of BPAD$^+$ above a certain threshold voltage. Our results show definitely that the molecule gets positively charged during electron transport through the HOMO of the molecule. Furthermore, the anti-stokes spectrum of the same molecular junction is also examined and shows an exponentially decreasing envelope of the peak intensities with the energy, which hints to a steady-state phonon distribution of the current carrying molecule. Furthermore, an excitation model is proposed and the electron−phonon coupling factor is deduced from the anti−Stokes Raman spectra.

Having identified the positive charge state of a current-driven single-molecule junction, we study the physical origin of the switching behavior of molecular junctions with TPD molecules and its analogue TM-TPD. The TPD species shows a well-pronounced, discrete Raman spectrum at any voltage. However, for the TM−TPD molecule, the planar $\pi−$conjugation is broken due to steric hindrance of the methy side-groups. Consequently, no Raman spectra is observable for TM-TPD in the uncharged case, which agree well with theoretical calculations. By controlling the bias voltage in the TM−TPD junction, the broken $\pi−$conjugation of TM−TPD could be recovered. The applied voltage causes a positive charge state for the TM−TPD molecule within the junction. The charged species, TM−TPD$^+$, shows a high $\pi−$conjugation, increasing the polarizabilty of the molecule. As a result, the Raman spectrum of TM−TPD is *turned on* upon exceeding a theshold voltage about 1.0 V. As a conclusion, the reason for the switching behavior

of this single-molecule junctions could be ascribed to the positively charge state cooling at specific conditions, which could be read out by Raman spectroscopy.

In our studies, the molecular wire of BPAD represents a highly conjugation system, whereas the $\pi-$system TPD and TM-TPD is steered by its side-groups. For both of the studies, we have investigated the current carrying single-molecule junction with near-field Raman spectroscopy. As a consequence of the charge transport, the Raman spectra of the two conducting molecular systems show that the molecule′s vibrations are excited by the charge transport. This effect could be real-time observed by near-field Raman spectroscopy. In this regard, we have got an efficient method to study electron-phonon excitations in current driven single-molecule junctions.

The MJS set-up has shown great potential for the further studies of the single-molecule junction. By detecting the conducting molecular junctions with Raman spectroscopy, lots of further experiment could be preformed to characterize organic materials on the single molecular level. The results of these studies will give us a better understanding of loss mechanism in organic light emitting devices and organic solar cells. The optical measurement of the current driver single-molecule junctions could also be extended to method beyond Raman spectroscopy. Other spectroscopy information such as, single-molecule fluorescence and infrared spectroscopy could also be exploited in the field of single-molecule junctions.

Bibliography

[1] A. Aviram and M. A. Ratner. Molecular rectifiers. *Chem. Phys. Lett.*, 29 (2):277–283, 1974. doi: 10.1016/0009-2614(74)85031-1. URL http://www.sciencedirect.com/science/article/pii/0009261474850311.

[2] Carlos-Andres Palma and Paolo Samorì. Blueprinting macromolecular electronics. *Nature chemistry*, 3(6):431–436, 2011.

[3] Stefan Frank, Philippe Poncharal, ZL Wang, and Walt A de Heer. Carbon nanotube quantum resistors. *Science*, 280(5370):1744–1746, 1998.

[4] Hideaki Ohnishi, Yukihito Kondo, and Kunio Takayanagi. Quantized conductance through individual rows of suspended gold atoms. *Nature*, 395(6704):780–783, 1998.

[5] Brian J LeRoy, SG Lemay, J Kong, and C Dekker. Electrical generation and absorption of phonons in carbon nanotubes. *Nature*, 432(7015):371–374, 2004.

[6] Sayed Hasan, Muhammad Ashraful Alam, and Mark S Lundstrom. Simulation of carbon nanotube FETs including hot-phonon and self-heating effects. *Electron Devices, IEEE Transactions on*, 54(9):2352–2361, 2007.

[7] Kevin D McCarthy, Nikolay Prokofev, and Mark T Tuominen. Incoherent dynamics of vibrating single-molecule transistors. *Physical Review B*, 67(24):245415, 2003.

[8] Johannes S Seldenthuis, Herre SJ van der Zant, Mark A Ratner, and Joseph M Thijssen. Vibrational excitations in weakly coupled single-molecule junctions: A computational analysis. *ACS nano*, 2(7):1445–1451, 2008.

[9] Edgar A Osorio, Kevin O'Neill, Nicolai Stuhr-Hansen, Ole F Nielsen, Thomas Bjørnholm, and Herre SJ van der Zant. Addition energies and vibrational fine structure measured in electromigrated single-molecule junctions based on an oligophenylenevinylene derivative. *Advanced Materials*, 19(2):281–285, 2007.

[10] Jiwoong Park, Abhay N Pasupathy, Jonas I Goldsmith, Connie Chang, Yuval Yaish, Jason R Petta, Marie Rinkoski, James P Sethna, Héctor D Abruña, Paul L McEuen, et al. Coulomb blockade and the Kondo effect in single-atom transistors. *Nature*, 417(6890):722–725, 2002.

[11] Niko Pavliček, Ingmar Swart, Judith Niedenführ, Gerhard Meyer, and Jascha Repp. Symmetry dependence of vibration-assisted tunneling. *Physical review letters*, 110(13):136101, 2013.

[12] BC Stipe, MA Rezaei, and W Ho. Single-molecule vibrational spectroscopy and microscopy. *Science*, 280(5370):1732–1735, 1998.

[13] Supriyo Datta. Electrical resistance: an atomistic view. *Nanotechnology*, 15(7): S433–S451, 2004.

[14] Yongqiang Xue and Mark A Ratner. Theoretical principles of single-molecule electronics: A chemical and mesoscopic view. *International journal of quantum chemistry*, 102(5):911–924, 2005.

[15] C Joachim, JK Gimzewski, A Aviram, et al. Electronics using hybrid-molecular and mono-molecular devices. *Nature*, 408(6812):541–548, 2000.

[16] Abraham Nitzan and Mark A Ratner. Electron transport in molecular wire junctions. *Science*, 300(5624):1384–1389, 2003.

[17] Yoram Selzer and David L Allara. Single-molecule electrical junctions. *Annu. Rev. Phys. Chem.*, 57:593–623, 2006.

[18] Abraham Nitzan. Electron transmission through molecules and molecular interfaces. *Annual Review of Physical Chemistry*, 52:681–694, 2001.

[19] MA Ordal, LL Long, RJ Bell, SE Bell, RR Bell, RW Alexander Jr, CA Ward, et al. Optical properties of the metals al, co, cu, au, fe, pb, ni, pd, pt, ag, ti, and w in the infrared and far infrared. *Applied Optics*, 22(7):1099–1119, 1983.

[20] Kees M Schep, Paul J Kelly, and Gerrit EW Bauer. Ballistic transport and electronic structure. *Physical Review B*, 57(15):8907, 1998.

[21] J Homoth, M Wenderoth, T Druga, L Winking, RG Ulbrich, CA Bobisch, B Weyers, A Bannani, E Zubkov, AM Bernhart, et al. Electronic transport on the nanoscale: Ballistic transmission and Ohm′s law. *Nano letters*, 9(4):1588–1592, 2009.

[22] Yuri A Berlin and Mark A Ratner. Intra-molecular electron transfer and electric conductance via sequential hopping: Unified theoretical description. *Radiation Physics and Chemistry*, 74(3):124–131, 2005.

[23] Rolf Landauer. Can a length of perfect conductor have a resistance? *Physics Letters A*, 85(2):91–93, 1981.

[24] AI Yanson, G Rubio Bollinger, HE Van den Brom, N Agrait, and JM Van Ruitenbeek. Formation and manipulation of a metallic wire of single gold atoms. *Nature*, 395(6704):783–785, 1998.

[25] XD Cui, A Primak, X Zarate, J Tomfohr, OF Sankey, AL Moore, TA Moore, D Gust, Gari Harris, and SM Lindsay. Reproducible measurement of single-molecule conductivity. *Science*, 294(5542):571–574, 2001.

[26] Rolf Landauer. Spatial variation of currents and fields due to localized scatterers in metallic conduction. *IBM Journal of Research and Development*, 1(3):223–231, 1957.

[27] Gabino Rubio-Bollinger, Sune Rastad Bahn, N Agrait, Karsten Wedel Jacobsen, and S Vieira. Mechanical properties and formation mechanisms of a wire of single gold atoms. *Physical Review Letters*, 87(2), 2001.

[28] Varlei Rodrigues, Tobias Fuhrer, and Daniel Ugarte. Signature of atomic structure in the quantum conductance of gold nanowires. *Physical review letters*, 85(19): 4124–4127, 2000.

[29] Mark A Reed, C Zhou, CJ Muller, TP Burgin, and JM Tour. Conductance of a molecular junction. *Science*, 278(5336):252–254, 1997.

[30] C Joachim and MA Ratner. Molecular wires: guiding the super-exchange interactions between two electrodes. *Nanotechnology*, 15(8):1065, 2004.

[31] M Di Ventra, ST Pantelides, and ND Lang. First-principles calculation of transport properties of a molecular device. *Physical review letters*, 84(5):979–982, 2000.

[32] Gary B Schuster. Long-range charge transfer in DNA: transient structural distortions control the distance dependence. *Accounts of chemical research*, 33(4): 253–260, 2000.

[33] Dvira Segal, Abraham Nitzan, William B Davis, Michael R Wasielewski, and Mark A Ratner. Electron transfer rates in bridged molecular systems 2. a steady-state analysis of coherent tunneling and thermal transitions. *The Journal of Physical Chemistry B*, 104(16):3817–3829, 2000.

[34] Yuri A Berlin, Alexander L Burin, and Mark A Ratner. Charge hopping in DNA. *Journal of the American Chemical Society*, 123(2):260–268, 2001.

[35] Xiaojuan Wang and Werner M Nau. Kinetics of one-and two-directional charge hopping in one-dimensional systems: Application to DNA. *ChemPhysChem*, 2 (12):761–766, 2001.

[36] EG Petrov, Ye V Shevchenko, and V May. On the length dependence of bridge-mediated electron transfer reactions. *Chemical Physics*, 288(2):269–279, 2003.

[37] Christian Joachim and Mark A Ratner. Molecular electronics: some views on transport junctions and beyond. *Proceedings of the National Academy of Sciences of the United States of America*, 102(25):8801–8808, 2005.

[38] Mark Elbing, Rolf Ochs, Max Koentopp, Matthias Fischer, Carsten von Hänisch, Florian Weigend, Ferdinand Evers, Heiko B Weber, and Marcel Mayor. A single-molecule diode. *Proceedings of the National Academy of Sciences of the United States of America*, 102(25):8815–8820, 2005.

[39] NB Zhitenev, Hong Meng, and Zhenan Bao. Conductance of small molecular junctions. *Physical review letters*, 88(22):226801, 2002.

[40] J Reichert, R Ochs, D Beckmann, HB Weber, M Mayor, and H v Löhneysen. Driving current through single organic molecules. *Physical Review Letters*, 88(17): 176804, 2002.

[41] Stuart M Lindsay and Mark A Ratner. Molecular transport junctions: Clearing mists. *Advanced Materials*, 19(1):23–31, 2007.

[42] Bingqian Xu and Nongjian J Tao. Measurement of single-molecule resistance by repeated formation of molecular junctions. *Science*, 301(5637):1221–1223, 2003.

[43] Xiaoyin Xiao, Bingqian Xu, and Nongjian J Tao. Measurement of single molecule conductance: Benzenedithiol and benzenedimethanethiol. *Nano Letters*, 4(2):267–271, 2004.

[44] Xiaoyin Xiao, Bingqian Xu, and Nongjian Tao. Conductance titration of single-peptide molecules. *Journal of the American Chemical Society*, 126(17):5370–5371, 2004.

[45] RHM Smit, Y Noat, C Untiedt, ND Lang, MC Van Hemert, and JM Van Ruiten-beek. Measurement of the conductance of a hydrogen molecule. *Nature*, 419(6910): 906–909, 2002.

[46] ND Lang and Ph Avouris. Electrical conductance of individual molecules. *Physical Review B*, 64(12):125323, 2001.

[47] Alexandre R Champagne, Abhay N Pasupathy, and Daniel C Ralph. Mechanically adjustable and electrically gated single-molecule transistors. *Nano letters*, 5(2): 305–308, 2005.

[48] Abhay N Pasupathy, Radoslaw C Bialczak, Jan Martinek, Jacob E Grose, Luke AK Donev, Paul L McEuen, and Daniel C Ralph. The Kondo effect in the presence of ferromagnetism. *Science*, 306(52):86–89, 2004.

[49] Wenjie Liang, Matthew P Shores, Marc Bockrath, Jeffrey R Long, and Hongkun Park. Kondo resonance in a single-molecule transistor. *Nature*, 417(6890):725–729, 2002.

[50] H Yu Lam and Douglas Natelson. Transport in single-molecule transistors: Kondo physics and negative differential resistance. *Nanotechnology*, 15(10):S517, 2004.

[51] LH Yu, Zachary K Keane, Jacob W Ciszek, Long Cheng, MP Stewart, JM Tour, and D Natelson. Inelastic electron tunneling via molecular vibrations in single-molecule transistors. *Physical review letters*, 93(26):266802, 2004.

[52] NJ Tao. Electron transport in molecular junctions. *Nature Nanotechnology*, 1(3): 173–181, 2006.

[53] Krzysztof Slowinski, Richard V Chamberlain, Cary J Miller, and Marcin Majda. Through-bond and chain-to-chain coupling. two pathways in electron tunneling through liquid alkanethiol monolayers on mercury electrodes. *Journal of the American Chemical Society*, 119(49):11910–11919, 1997.

[54] David J Wold and C Daniel Frisbie. Formation of metal-molecule-metal tunnel junctions: Microcontacts to alkanethiol monolayers with a conducting AFM tip. *Journal of the American Chemical Society*, 122(12):2970–2971, 2000.

[55] Wenyong Wang, Takhee Lee, and Mark A Reed. Mechanism of electron conduction in self-assembled alkanethiol monolayer devices. *Physical Review B*, 68(3):035416, 2003.

[56] Fabian Pauly, Janne K Viljas, Juan Carlos Cuevas, and Gerd Schön. Density-functional study of tilt-angle and temperature-dependent conductance in biphenyl dithiol single-molecule junctions. *Physical Review B*, 77(15):155312, 2008.

[57] Gerd Binnig and Heinrich Rohrer. In touch with atoms. *Reviews of Modern Physics*, 71(2):S324, 1999.

[58] Latha Venkataraman, Jennifer E Klare, Colin Nuckolls, Mark S Hybertsen, and Michael L Steigerwald. Dependence of single-molecule junction conductance on molecular conformation. *Nature*, 442(7105):904–907, 2006.

[59] Alexander L Burin and Mark A Ratner. Charge injection into disordered molecular films. *Journal of Polymer Science Part B: Polymer Physics*, 41(21):2601–2621, 2003.

[60] Amy Szuchmacher Blum, James G Kushmerick, David P Long, Charles H Patterson, John C Yang, Jay C Henderson, Yuxing Yao, James M Tour, Ranganathan Shashidhar, and Banahalli R Ratna. Molecularly inherent voltage-controlled conductance switching. *Nature Materials*, 4(2):167–172, 2005.

[61] ZK Keane, JW Ciszek, JM Tour, and D Natelson. Three-terminal devices to examine single-molecule conductance switching. *Nano letters*, 6(7):1518–1521, 2006.

[62] Emanuel Lörtscher, Jacob W Ciszek, James Tour, and Heike Riel. Reversible and controllable switching of a single-molecule junction. *Small*, 2(8-9):973–977, 2006.

[63] Velimir Meded, Alexei Bagrets, Andreas Arnold, and Ferdinand Evers. Molecular switch controlled by pulsed bias voltages. *Small*, 5(19):2218–2223, 2009.

[64] Jin He, Qiang Fu, Stuart Lindsay, Jacob W Ciszek, and James M Tour. Electrochemical origin of voltage-controlled molecular conductance switching. *Journal of the American Chemical Society*, 128(46):14828–14835, 2006.

[65] Michael Galperin, Mark A Ratner, Abraham Nitzan, and Alessandro Troisi. Nuclear coupling and polarization in molecular transport junctions: beyond tunneling to function. *Science*, 319(5866):1056–1060, 2008.

[66] Gaël Reecht, Fabrice Scheurer, Virginie Speisser, Yannick J Dappe, Fabrice Mathevet, and Guillaume Schull. Electroluminescence of a polythiophene molecular wire suspended between a metallic surface and the tip of a scanning tunneling microscope. *Physical review letters*, 112(4):047403, 2014.

[67] Joshua Hihath, Carlos R Arroyo, Gabino Rubio-Bollinger, Nongjian Tao, and Nicolás Agraït. Study of electron-phonon interactions in a single molecule covalently connected to two electrodes. *Nano letters*, 8(6):1673–1678, 2008.

[68] Jens Koch, Matthias Semmelhack, Felix von Oppen, and Abraham Nitzan. Current-induced nonequilibrium vibrations in single-molecule devices. *Physical Review B*, 73(15):155306, 2006.

[69] Renaud Leturcq, Christoph Stampfer, Kevin Inderbitzin, Lukas Durrer, Christofer Hierold, Eros Mariani, Maximilian G Schultz, Felix von Oppen, and Klaus Ensslin. Franck-Condon blockade in suspended carbon nanotube quantum dots. *Nature Physics*, 5(5):327–331, 2009.

[70] Aditi Mitra, Igor Aleiner, and AJ Millis. Phonon effects in molecular transistors: Quantal and classical treatment. *Physical Review B*, 69(24):245302, 2004.

[71] Joost van der Lit, Mark P Boneschanscher, Daniël Vanmaekelbergh, Mari Ijäs, Andreas Uppstu, Mikko Ervasti, Ari Harju, Peter Liljeroth, and Ingmar Swart. Suppression of electron-vibron coupling in graphene nanoribbons contacted via a single atom. *Nature communications*, 4, 2013.

[72] EA Osorio, Thomas Bjornholm, JM Lehn, M Ruben, and HSJ Van der Zant. Single-molecule transport in three-terminal devices. *Journal of Physics: Condensed Matter*, 20(37):374121, 2008.

[73] Jens Koch and Felix von Oppen. Franck-Condon blockade and giant Fano factors in transport through single molecules. *Physical review letters*, 94(20):206804, 2005.

[74] Ned S Wingreen, Karsten W Jacobsen, and John W Wilkins. Resonant tunneling with electron-phonon interaction: an exactly solvable model. *Physical review letters*, 61(22):2633, 1988.

[75] Stephan Braig and Karsten Flensberg. Vibrational sidebands and dissipative tunneling in molecular transistors. *Physical Review B*, 68(20):205324, 2003.

[76] Maarten R Wegewijs and Katja C Nowack. Nuclear wavefunction interference in single-molecule electron transport. *New Journal of Physics*, 7(1):239, 2005.

[77] Daniel Boese and Herbert Schoeller. Influence of nanomechanical properties on single-electron tunneling: A vibrating single-electron transistor. *EPL (Europhysics Letters)*, 54(5):668, 2001.

[78] George C Schatz and Mark A Ratner. *Quantum mechanics in chemistry*. Courier Dover Publications, 2012.

[79] Jens Koch, Felix von Oppen, and AV Andreev. Theory of the Franck-Condon blockade regime. *Physical Review B*, 74(20):205438, 2006.

[80] Nathalie P de Leon, Wenjie Liang, Qian Gu, and Hongkun Park. Vibrational excitation in single-molecule transistors: Deviation from the simple Franck-Condon prediction. *Nano letters*, 8(9):2963–2967, 2008.

[81] Rudolph A Marcus. Electron transfer reactions in chemistry. theory and experiment. *Reviews of Modern Physics*, 65(3):599–610, 1993.

[82] Ewen Smith and Geoffrey Dent. *Modern Raman spectroscopy: a practical approach*. John Wiley & Sons, 2005.

[83] Chandrasekhara Venkata Raman and Kariamanikkam Srinivasa Krishnan. A new type of secondary radiation. *Nature*, 121(3048):501–502, 1928.

[84] RW Wood. XLII. on a remarkable case of uneven distribution of light in a diffraction grating spectrum. *The London, Edinburgh, and Dublin Philosophical Magazine and Journal of Science*, 4(21):396–402, 1902.

[85] SL Cunningham, AA Maradudin, and RF Wallis. Effect of a charge layer on the surface-plasmon-polariton dispersion curve. *Physical Review B*, 10(8):3342, 1974.

[86] Gustav Mie. Beiträge zur optik trüber medien, speziell kolloidaler metallösungen. *Annalen der physik*, 330(3):377–445, 1908.

[87] JC Maxwell Garnett. Colours in metal glasses and in metallic films. *Philosophical Transactions of the Royal Society of London. Series A, Containing Papers of a Mathematical or Physical Character*, pages 385–420, 1904.

[88] RH Ritchie. Plasma losses by fast electrons in thin films. *Physical Review*, 106(5): 874, 1957.

[89] RH Ritchie, ET Arakawa, JJ Cowan, and RN Hamm. Surface-plasmon resonance effect in grating diffraction. *Physical Review Letters*, 21(22):1530, 1968.

[90] Andreas Otto. Excitation of nonradiative surface plasma waves in silver by the method of frustrated total reflection. *Zeitschrift für Physik*, 216(4):398–410, 1968.

[91] Erwin Kretschmann and Heinz Raether. Radiative decay of non radiative surface plasmons excited by light(Surface plasma waves excitation by light and decay into photons applied to nonradiative modes). *Zeitschrift Fuer Naturforschung, Teil A*, 23:2135, 1968.

[92] Uwe Kreibig and Peter Zacharias. Surface plasma resonances in small spherical silver and gold particles. *Zeitschrift für Physik*, 231(2):128–143, 1970.

[93] Eric Betzig, Jay K Trautman, et al. Near-field optics: microscopy,spectroscopy,and surface modification beyond the diffraction limit. *Science (New York,NY)*, 257 (5067):189, 1992.

[94] Daniel Courjon and C Bainier. Near field microscopy and near field optics. *Reports on progress in Physics*, 57(10):989, 1999.

[95] Christian Girard and Alain Dereux. Near-field optics theories. *Reports on Progress in Physics*, 59(5):657, 1999.

[96] Lukas Novotny and Bert Hecht. *Principles of nano-optics*. Cambridge university press, 2006.

[97] Alexandre Bouhelier, M Beversluis, Achim Hartschuh, and Lukas Novotny. Near-field second-harmonic generation induced by local field enhancement. *Physical review letters*, 90(1):013903, 2003.

[98] Neil Anderson, Alexandre Bouhelier, and Lukas Novotny. Near-field photonics: tip-enhanced microscopy and spectroscopy on the nanoscale. *Journal of Optics A: Pure and Applied Optics*, 8(4):S227, 2006.

[99] Oliver Benson. Assembly of hybrid photonic architectures from nanophotonic constituents. *Nature*, 480(7376):193–199, 2011.

[100] Katherine A Willets and Richard P Van Duyne. Localized surface plasmon resonance spectroscopy and sensing. *Annu. Rev. Phys. Chem.*, 58:267–297, 2007.

[101] Junxi Zhang, Lide Zhang, and Wei Xu. Surface plasmon polaritons: physics and applications. *Journal of Physics D: Applied Physics*, 45(11):113001, 2012.

[102] Ibrahim Abdulhalim, Mohammad Zourob, and Akhlesh Lakhtakia. Surface plasmon resonance for biosensing: a mini-review. *Electromagnetics*, 28(3):214–242, 2008.

[103] Raman Kashyap and Galina Nemova. Surface plasmon resonance-based fiber and planar waveguide sensors. *Journal of Sensors*, 2009, 2009.

[104] DW Pohl, W Denk, M Lanz, A Bouhelier, et al. SNOM. *Appl. Phys. Lett*, 44:651, 1984.

[105] Bin Ren, Gennaro Picardi, and Bruno Pettinger. Preparation of gold tips suitable for tip-enhanced raman spectroscopy and light emission by electrochemical etching. *Review of Scientific Instruments*, 75(4):837–841, 2004.

[106] Aurélien Crut, Paolo Maioli, Natalia Del Fatti, and Fabrice Vallée. Optical absorption and scattering spectroscopies of single nano-objects. *Chemical Society Reviews*, 43(11):3921–3956, 2014.

[107] Samuel Berweger, Joanna M Atkin, Robert L Olmon, and Markus B Raschke. Adiabatic tip-plasmon focusing for nano-Raman spectroscopy. *The Journal of Physical Chemistry Letters*, 1(24):3427–3432, 2010.

[108] Johannes Stadler, Thomas Schmid, and Renato Zenobi. Developments in and practical guidelines for tip-enhanced Raman spectroscopy. *Nanoscale*, 4(6):1856–1870, 2012.

[109] J Stadler, T Schmid, and R Zenobi. Nanoscale chemical imaging using top-illumination tip-enhanced Raman spectroscopy. *Nano letters*, 10(11):4514–4520, 2010.

[110] Raoul M Stöckle, Yung Doug Suh, Volker Deckert, and Renato Zenobi. Nanoscale chemical analysis by tip-enhanced Raman spectroscopy. *Chemical Physics Letters*, 318(1):131–136, 2000.

[111] Mark S Anderson. Locally enhanced Raman spectroscopy with an atomic force microscope. *Applied Physics Letters*, 76(21):3130–3132, 2000.

[112] Norihiko Hayazawa, Yasushi Inouye, Zouheir Sekkat, and Satoshi Kawata. Metallized tip amplification of near-field raman scattering. *Optics Communications*, 183(1):333–336, 2000.

[113] Tanja Deckert-Gaudig and Volker Deckert. Ultraflat transparent gold nanoplates: ideal substrates for tip-enhanced raman scattering experiments. *Small*, 5(4):432–436, 2009.

[114] Bruno Pettinger, Gennaro Picardi, Rolf Schuster, and Gerhard Ertl. Surface-enhanced and STM-tip-enhanced Raman spectroscopy at metal surfaces. *Single Molecules*, 3(5-6):285–294, 2002.

[115] Thomas Schmid, Boon-Siang Yeo, Grace Leong, Johannes Stadler, and Renato Zenobi. Performing tip-enhanced Raman spectroscopy in liquids. *Journal of Raman Spectroscopy*, 40(10):1392–1399, 2009.

[116] Linda T Nieman, Gerhard M Krampert, and Robert E Martinez. An apertureless near-field scanning optical microscope and its application to surface-enhanced raman spectroscopy and multiphoton fluorescence imaging. *Review of Scientific Instruments*, 72(3):1691–1699, 2001.

[117] Catalin C Neacsu, Jens Dreyer, Nicolas Behr, and Markus B Raschke. Scanning-probe Raman spectroscopy with single-molecule sensitivity. *Physical Review B*, 73 (19):193406, 2006.

[118] Bruno Pettinger, Bin Ren, Gennaro Picardi, Rolf Schuster, and Gerhard Ertl. Nanoscale probing of adsorbed species by tip-enhanced raman spectroscopy. *Physical review letters*, 92(9):096101, 2004.

[119] D Mehtani, N Lee, RD Hartschuh, A Kisliuk, MD Foster, AP Sokolov, and JF Maguire. Nano-raman spectroscopy with side-illumination optics. *Journal of Raman Spectroscopy*, 36(11):1068–1075, 2005.

[120] Y Saito, M Motohashi, N Hayazawa, M Iyoki, and S Kawata. Nanoscale characterization of strained silicon by tip-enhanced Raman spectroscope in reflection mode. *Applied physics letters*, 88(14):143109, 2006.

[121] U Ch Fischer. The tetrahedral tip as a probe for scanning near-field optical microscopy. *NATO ASI SERIES E APPLIED SCIENCES*, 242:255–255, 1993.

[122] C Debus, MA Lieb, A Drechsler, and AJ Meixner. Probing highly confined optical fields in the focal region of a high NA parabolic mirror with subwavelength spatial resolution. *Journal of microscopy*, 210(3):203–208, 2003.

[123] Jens Steidtner and Bruno Pettinger. High-resolution microscope for tip-enhanced optical processes in ultrahigh vacuum. *Review of Scientific Instruments*, 78(10): 103104, 2007.

[124] Marcus Sackrow, Catrinel Stanciu, M Andreas Lieb, and Alfred J Meixner. Imaging nanometre-sized hot spots on smooth au films with high-resolution tip-enhanced luminescence and Raman near-field optical microscopy. *ChemPhysChem*, 9(2):316–320, 2008.

[125] C Stanciu, M Sackrow, and AJ Meixner. High NA particle-and tip-enhanced nanoscale raman spectroscopy with a parabolic-mirror microscope. *Journal of microscopy*, 229(2):247–253, 2008.

[126] F Rasetti. Selection rules in the raman effect. *Nature*, 123:757–759, 1929.

[127] Derek Albert Long and DA Long. *Raman spectroscopy*, volume 206. McGraw-Hill New York, 1977.

[128] Katrin F Domke and Bruno Dai Zhang, and Pettinger. Enhanced Raman spectroscopy: single molecules or carbon? *The Journal of Physical Chemistry C*, 111 (24):8611–8616, 2007.

[129] Katrin F Domke, Dai Zhang, and Bruno Pettinger. Toward Raman fingerprints of single dye molecules at atomically smooth Au (111). *Journal of the American Chemical Society*, 128(45):14721–14727, 2006.

[130] Weihua Zhang, Boon Siang Yeo, Thomas Schmid, and Renato Zenobi. Single molecule tip-enhanced Raman spectroscopy with silver tips. *The Journal of Physical Chemistry C*, 111(4):1733–1738, 2007.

[131] R Zhang, Y Zhang, ZC Dong, S Jiang, C Zhang, LG Chen, L Zhang, Y Liao, J Aizpurua, Yi Luo, et al. Chemical mapping of a single molecule by plasmon-enhanced Raman scattering. *Nature*, 498(7452):82–86, 2013.

[132] Zheng Liu, Song-Yuan Ding, Zhao-Bin Chen, Xiang Wang, Jing-Hua Tian, Jason R Anema, Xiao-Shun Zhou, De-Yin Wu, Bing-Wei Mao, Xin Xu, et al. Revealing the molecular structure of single-molecule junctions in different conductance states

by fishing-mode tip-enhanced raman spectroscopy. *Nature communications*, 2:305, 2011.

[133] Jing-Hua Tian, Bo Liu, Xiulan Li, Zhi-Lin Yang, Bin Ren, Sun-Tao Wu, Nongjian Tao, and Zhong-Qun Tian. Study of molecular junctions with a combined surface-enhanced Raman and mechanically controllable break junction method. *Journal of the American Chemical Society*, 128(46):14748–14749, 2006.

[134] Katrin Kneipp, Yang Wang, Harald Kneipp, Irving Itzkan, Ramachandra R Dasari, and Michael S Feld. Population pumping of excited vibrational states by spontaneous surface-enhanced Raman scattering. *Physical review letters*, 76(14):2444, 1996.

[135] Daniel R Ward, Naomi J Halas, Jacob W Ciszek, James M Tour, Yanpeng Wu, Peter Nordlander, and Douglas Natelson. Simultaneous measurements of electronic conduction and Raman response in molecular junctions. *Nano letters*, 8(3):919–924, 2008.

[136] Daniel R Ward, Nathaniel K Grady, Carly S Levin, Naomi J Halas, Yanpeng Wu, Peter Nordlander, and Douglas Natelson. Electromigrated nanoscale gaps for surface-enhanced Raman spectroscopy. *Nano letters*, 7(5):1396–1400, 2007.

[137] Eugene G Bortchagovsky, Stefan Klein, and Ulrich C Fischer. Surface plasmon mediated tip enhanced raman scattering. *Applied Physics Letters*, 94(6):063118, 2009.

[138] A Bouhelier, Jb Renger, MR Beversluis, and L Novotny. Plasmon-coupled tip-enhanced near-field optical microscopy. *Journal of microscopy*, 210(3):220–224, 2003.

[139] J Koglin, U Ch Fischer, and H Fuchs. Material contrast in scanning near-field optical microscopy at 10 nm resolution. *Physical Review B*, 55(12):7977, 1997.

[140] K Tanaka, GW Burr, T Grosjean, T Maletzky, and UC Fischer. Superfocussing in a metal-coated tetrahedral tip by dimensional reduction of surface-to edge-plasmon modes. *Applied Physics B*, 93(1):257–266, 2008.

[141] Stefan Klein, Joachim Reichert, Harald Fuchs, and Ulrich Fischer. Near-field Raman spectroscopy using a tetrahedral snom tip. In *Photonics Europe*, pages 61951F–61951F. International Society for Optics and Photonics, 2006.

[142] Eugene G Bortchagovsky and Ulrich C Fischer. A tetrahedral tip as a probe for tip-enhanced raman scattering and as a near-field raman probe. *Journal of Raman Spectroscopy*, 40(10):1386–1391, 2009.

[143] J Heimel, UC Fischer, and H Fuchs. SNOM/STM using a tetrahedral tip and a sensitive current-to-voltage converter. *Journal of microscopy*, 202(1):53–59, 2001.

[144] Giulio Biagi, Tobias Holmgaard, and Esben Skovsen. Near-field electrospinning of dielectric-loaded surface plasmon polariton waveguides. *Optics express*, 21(4): 4355–4360, 2013.

[145] Tomasz J Antosiewicz, Piotr Wróbel, and Tomasz Szoplik. Performance of scanning near-field optical microscope probes with single groove and various metal coatings. *Plasmonics*, 6(1):11–18, 2011.

[146] Davide Tranchida, Jordi Diaz, Peter Schön, Holger Schönherr, and G Julius Vancso. Scanning near-field ellipsometry microscopy: imaging nanomaterials with resolution below the diffraction limit. *Nanoscale*, 3(1):233–239, 2011.

[147] Valeria Lotito, Urs Sennhauser, and Christian Hafner. Effects of asymmetric surface corrugations on fully metal-coated scanning near field optical microscopy tips. *Optics express*, 18(8):8722–8734, 2010.

[148] Daniel Gerster, Joachim Reichert, Hai Bi, Johannes V Barth, Simone M Kaniber, Alexander W Holleitner, Iris Visoly-Fisher, Shlomi Sergani, and Itai Carmeli. Photocurrent of a single photosynthetic protein. *Nature nanotechnology*, 7(10):673–676, 2012.

[149] Jens Steidtner and Bruno Pettinger. Tip-enhanced Raman spectroscopy and microscopy on single dye molecules with 15 nm resolution. *Physical review letters*, 100(23):236101, 2008.

[150] Bruno Pettinger, Bin Ren, Gennaro Picardi, Rolf Schuster, and Gerhard Ertl. Tip-enhanced Raman spectroscopy (TERS) of malachite green isothiocyanate at au (111): bleaching behavior under the influence of high electromagnetic fields. *Journal of Raman Spectroscopy*, 36(6-7):541–550, 2005.

[151] Marcel Mayor, Heiko B Weber, Joachim Reichert, Mark Elbing, Carsten von Hänisch, Detlef Beckmann, and Matthias Fischer. Electric current through a molecular rod relevance of the position of the anchor groups. *Angewandte Chemie International Edition*, 42(47):5834–5838, 2003.

[152] J Heurich, JC Cuevas, W Wenzel, and G Schön. Electrical transport through single-molecule junctions: from molecular orbitals to conduction channels. *Physical review letters*, 88(25):256803, 2002.

[153] A Prasanna De Silva and Seiichi Uchiyama. Molecular logic and computing. *Nature Nanotechnology*, 2(7):399–410, 2007.

[154] Willi Auwärter, Knud Seufert, Felix Bischoff, David Ecija, Saranyan Vijayaragha-van, Sushobhan Joshi, Florian Klappenberger, Niveditha Samudrala, and Jo-hannes V Barth. A surface-anchored molecular four-level conductance switch based on single proton transfer. *Nature nanotechnology*, 7(1):41–46, 2012.

[155] Hongkun Park, Jiwoong Park, Andrew KL Lim, Erik H Anderson, A Paul Alivisatos, and Paul L McEuen. Nanomechanical oscillations in a single-C60 tran-sistor. *Nature*, 407(6800):57–60, 2000.

[156] LA Ponomarenko, F Schedin, MI Katsnelson, R Yang, EW Hill, KS Novoselov, and AK Geim. Chaotic dirac billiard in graphene quantum dots. *Science*, 320 (5874):356–358, 2008.

[157] Francis Garnier, Gilles Horowitz, Xuezhou Peng, and Denis Fichou. An all-organic" soft" thin film transistor with very high carrier mobility. *Advanced Ma-terials*, 2(12):592–594, 1990.

[158] A Prasanna de Silva and Nathan D McClenaghan. Proof-of-principle of molecular-scale arithmetic. *Journal of the American Chemical Society*, 122(16):3965–3966, 2000.

[159] Alberto Credi, Vincenzo Balzani, Steven J Langford, and J Fraser Stoddart. Logic operations at the molecular level: An XOR gate based on a molecular machine. *Journal of the American Chemical Society*, 119(11):2679–2681, 1997.

[160] Tarkeshwar Gupta and Milko E van der Boom. Redox-active monolayers as a versatile platform for integrating boolean logic gates. *Angewandte Chemie*, 120 (29):5402–5406, 2008.

[161] David Margulies, Galina Melman, and Abraham Shanzer. A molecular full-adder and full-subtractor, an additional step toward a moleculator. *Journal of the Amer-ican Chemical Society*, 128(14):4865–4871, 2006.

[162] Kouichi Hosaka, Hiroyuki Shimada, Hisashi Chiba, Hiroyuki Katsuki, Yoshiaki Teranishi, Yukiyoshi Ohtsuki, and Kenji Ohmori. Ultrafast Fourier transform with a femtosecond-laser-driven molecule. *Physical review letters*, 104(18):180501, 2010.

[163] Jeffrey M Mativetsky, Giuseppina Pace, Mark Elbing, Maria A Rampi, Marcel Mayor, and Paolo Samorì. Azobenzenes as light-controlled molecular electronic switches in nanoscale metal- molecule- metal junctions. *Journal of the American Chemical Society*, 130(29):9192–9193, 2008.

[164] Masahiro Irie. Diarylethenes for memories and switches. *Chemical Reviews*, 100 (5):1685–1716, 2000.

[165] Ben L Feringa. The art of building small: from molecular switches to molecular motors. *The Journal of organic chemistry*, 72(18):6635–6652, 2007.

[166] Joakim Andréasson, Uwe Pischel, Stephen D Straight, Thomas A Moore, Ana L Moore, and Devens Gust. All-photonic multifunctional molecular logic device. *Journal of the American Chemical Society*, 133(30):11641–11648, 2011.

[167] Emanuele Orgiu, Núria Crivillers, Martin Herder, Lutz Grubert, Michael Pätzel, Johannes Frisch, Egon Pavlica, Duc T Duong, Gvido Bratina, Alberto Salleo, et al. Optically switchable transistor via energy-level phototuning in a bicomponent organic semiconductor. *Nature chemistry*, 4(8):675–679, 2012.

[168] Agustin Schiffrin, Tim Paasch-Colberg, Nicholas Karpowicz, Vadym Apalkov, Daniel Gerster, Sascha Mühlbrandt, Michael Korbman, Joachim Reichert, Martin Schultze, Simon Holzner, et al. Optical-field-induced current in dielectrics. *Nature*, 493(7430):70–74, 2013.

[169] KL Kompa and RD Levine. A molecular logic gate. *Proceedings of the National Academy of Sciences*, 98(2):410–414, 2001.

[170] Edward H Witlicki, Carsten Johnsen, Stinne W Hansen, Daniel W Silverstein, Vincent J Bottomley, Jan O Jeppesen, Eric W Wong, Lasse Jensen, and Amar H Flood. Molecular logic gates using surface-enhanced Raman-scattered light. *Journal of the American Chemical Society*, 133(19):7288–7291, 2011.

[171] Hennie Valkenier, Constant M Guédon, Troels Markussen, Kristian S Thygesen, Sense J van der Molen, and Jan C Hummelen. Cross-conjugation and quantum interference: a general correlation? *Phys. Chem. Chem. Phys.*, 16(2):653–662, 2013.

[172] Fanben Meng, Yves-Marie Hervault, Qi Shao, Benhui Hu, Lucie Norel, Stéphane Rigaut, and Xiaodong Chen. Orthogonally modulated molecular transport junctions for resettable electronic logic gates. *Nature communications*, 5, 2014.

List of Figures

List of Acronyms

AFM	Atomic Force Microscopy
BPDN-DT	Bipyridyl-dinitro oligophenylene-ethynylene dithiol
DFT	Density Functional Theory
HE	Hybrid Mode
HOMO	Highest Occupied Molecular Orbital
IPT	Inter-Phenyl Torsion
ITO	Indium Tin Oxide
I-V	Current-Voltage
LUMO	Lowest Unoccupied Molecular Orbital
MCBJ	Mechanically Controlled Break Junction
MGTIC	Malachite Green Isothiocyanate
MJS	Molecular Junction Spectroscopy
MPSMU	Medium Power Source Measuring Unit
NA	Numerical Aperture
PLC	Power Line Cycles
SAP	Sum of the Absoltute values of the Polarizability tensor elements
SERS	Surface Enhanced Raman Spectroscopy
SPPs	Surface Plasmon Polaritons
SNOM	Scanning Near Field Optical Microscopy
SPM	Scanning Probe Microscopy
TERS	Tip-Enhanced Raman Spectroscopy
TM	Transverse Magnetic Mode
T-tip	Tetrahedral Tip
UHV	Ultra-High Vacuum

Acknowledgements